Design of Robust PTFE Faced Bearings for Performance and Reliability in Large Rotating Machinery

Benjamin Charles Rothwell

Submitted in accordance with the requirements for the degree of

Doctor of Philosophy

The University of Leeds

School of Mechanical Engineering

June 2016

The candidate confirms that the work submitted is his own and that appropriate credit has been given where reference has been made to the work of others.

Acknowledgements

I would first like to thank my supervisors Dr R Hewson, Prof D Barton, Prof A Neville and Dr A Morina who have provided guidance, motivation and patience throughout this whole project. I would also like to thank my industrial supervisor Dr D Horner for the advice and guidance over the year and Michell Bearings, Rolls Royce Ltd and EPSRC founding body for their financial support.

To my colleagues at the University of Leeds, a big thank you for the coffee breaks, talks and advice whenever I was lost and or stuck. Your ears and brains were very much appreciated. A special mention to Greg for bearing chats, Adam T for the distractions and Joe for keeping me in line when needed. Thanks to Pollard for the car boot sales, fun was had.

My colleagues at BAE, thank you for feeding me, making me be social and putting up with the PhD chat whilst I was writing up. It's over now, you can relax.

Hazel and Daniel, thank you guys for the films, food, jokes and time. It was a pleasure to meet you guys during this whole thing.

Nick for being the house mate I needed all those years and not the house mate I wanted, for the all the hours spent working in lecture theatre E and all the trips/ breaks/ weekends and evenings. That being said, you still owe me a coffee machine.

Stuart and Laura, thanks for putting up with all the phone calls at all hours of the day, even if you were on night shifts, but mainly for everything else over the years.

Finally I would like to dedicate this thesis to my parents and sister. Thank you guys for everything!

Abstract

In this thesis a Finite Element Modelling (FEM) approach is proposed for modelling the visco-plastic creep effects that a PTFE-faced thrust bearing would undergo during normal operating conditions. A thermal elastic hydrodynamic lubrication (TEHL) model is developed, which uses the Reynolds equations for a fluid film, coupled with Hertzian contact theory and the energy equation to predict the pressure and film thickness on the PTFE face as well as the temperature and thickness of the fluid. These variables are then used with a Norton creep function to predict the secondary creep effects on the PTFE surface. This change in PTFE thickness due to visco-plastic effects are taken into account within the film thickness equations and the effects over a bearing's operational life span studied.

The Norton creep function is obtained from experimental creep results conducted on filled PTFE samples at the University of Leeds. This experimental method allowed for the displacement of the samples to be recorded over a 7 day test period at a representative range of pressure and temperature conditions and a Norton creep function to be obtained from the results. The Norton creep function was then included within the simulations to allow for the visco-plastic creep effects to be studied.

Results obtained showed that whilst the secondary creep had a small effect on the pressure profile of the pad, the peak pressure was significantly affected during the duration of the pads operational life. It was concluded that this was due to the pad deformation changing, meaning a smaller peak pressure was observed, but the tilt angle did not change greatly, meaning the profile did not change.

The pad and film thickness also changed as time passed, with the pad getting thinner in areas of high pressure and temperature, due to the secondary creep effects. It was also observed that the peak temperature of the pad also decreased as time passed, due to the film thickness increase in areas of high temperature.

Contents

Table of Figures

List of Tables

Nomenclature

ε_p	=	Strain due to primary creep
ε_s	=	Strain due to secondary creep
$\frac{\partial \varepsilon}{\partial t}$	=	Secondary creep rate
∂_n	=	Initial displacement (m)
∂_T	=	Current displacement (m)
μ	=	Viscosity (Pa s)
A, n	=	Norton creep function constants
A_s	=	Area of sample (m^2)
C_p	=	Specific heat capacity at constant pressure (J/kg K)
E	=	Young's Modulus (MPa)
E_I	=	Internal energy (J)
g	=	Gravity (m/s^2)
H	=	Film thickness (m)
h_{01}	=	Undeformed film thickness (m)
h_G	=	Gap thickness (m)
H_s	=	Original height of sample (m)
K	=	Thermal conductivity (W/mK)
k	=	Hot oil carry over coefficient
m	=	Mass (kg)
p	=	Pressure (Pa)
Q	=	Activation energy (J/mol)
R	=	Universal gas constant (J/mol K)
R_o, R_i	=	Radius of outer/ inner edge of pad (m)
T	=	Temperature (K)

T_{oil}	=	Temperature of oil exiting pad (K)
T_{sup}	=	Temperature of fresh supplied oil (K)
u, v, w	=	Velocity in a x, y, z direction (m/s)
U_1, V_1	=	x, y velocity at pad surface (m/s)
U_2, V_2	=	x, y velocity at collar (m/s)
V_m	=	Average velocity of oil (m/s)
W	=	Deformation of pad due to pressure (m)
x, y, z	=	Cordiant position (m)
α	=	Coefficient of thermal expansion ($^{O}C^{-1}$)
α_t	=	Tilt Angle (^{O})
γ	=	Poisson's Ratio
ε_s	=	Strain due to secondary creep
ε_T	=	True strain
ε_{TE}	=	Strain due to thermal expansion
ρ	=	Density (kg/m^3)
φ	=	Viscous dissipation
∂	=	Displacement from datum (m)

Chapter 1- Introduction

Tilting pad thrust bearings have been used for over a hundred years, in a large range of propulsion systems to support axial loads of a rotating shaft, by having a ring of induvial tilting sectional pads separated from the rotating axial counter face by a pressurised oil film. This pressure oil film stops the pad and counter face from coming into contact with the pad, and each pad tilts separately until the optimum position is found. The bearings can be used in a range of applications, varying in size and load carrying capacity, and these applications can include submarine engines, car engines, generators and hydro-electric generators to name a few applications. These bearings are used in industry on a daily basis and a scientific understanding of the tribological and mechanical properties are required to allow for optimum design and operating parameters to be set for individual thrust pads before manufacture. A further understanding of the pads' mechanical and tribological behaviour allows for accurate predictions of safety margins [1] meaning that a pad will not be overloaded and damaged, increasing the pads' operational life span. These bearings can vary in size, facing materials and can have a variety of support systems depending on the required application. The typical facing material used in these bearings are polytetrafluoroethylene (PTFE), a carbon based polymer more commonly known as Teflon, in both filled and unfilled forms, and more traditionally Babbitt metal, which is a tin alloy. Due to the facing material of PTFE being a polymer or soft metal, deformation on the pad surface con occur, causing changes to the fluid flow profile [2] and therefore effecting the load carrying capacity of the pad. Whilst this change has been investigated both experimentally and computationally over the years, computational analysis is now favoured due to the low costs involved, when compared to experimental work and the time saved [3].

1.1 Aims of Project

The overall aim of this project is the development of a Thermal Elastic-Hydrodynamic Lubrication (TEHL) model with visco-plastic effects for thrust bearing pad design. The project will also conduct creep experiments on PTFE to understand how the material changes over time due to creep and temperature, so that the visco-plastic effects can be measured, and incorporated into the model. With these visco-plastic effects included within the model, more accurate life span predictions can be made for pad pressure and temperature, as well as estimations of power loss over the life span of the pad.

The objectives of this project are therefore to:

a. Conduct a comprehensive literature review of past and current research into tilting pad thrust bearing performance.

b. Develop a thermal elasto- hydrodynamic lubrication model (TEHL) for a PTFE face thrust pad.

c. Conduct compressive creep experiments on PTFE samples.

d. Include creep effects into the TEHL model to create a visco-plastic TEHL model.

e. Study the effect of creep on long term bearing performance.

1.2 Thesis Layout

Chapter 2 within this thesis provides a literature review on current published work in the field of thrust pad bearings, and TEHL modelling of their domain, as well as a review of creep effects and PTFE as a facing material. Chapter 3 provides an overview of the experimental method used to collect creep data. In Chapter 4 the creep results are presented and a numerical creep function for filled PTFE is derived. Chapter 5 lays out the TEHL computational model used to simulate the thrust pad, along with the method to

include the visco-plastic creep function found in Chapter 4. Chapter 6 examines the effect of creep on thrust pad bearing performance and discusses the effect of visco-plastic effects on a pad's surface and operational life span, before conclusions are drawn about the project in Chapter 7.

Chapter 2- Literature Review

2.1 Theory of Modelling

2.1.1 Thrust Bearing

During the late 19th century when a rotating shaft's axial load needed to be supported, a metal to metal contact was the only known solution to maintain the load. This design resulted in wear and heat generation occurring at the metal interfaces which resulted in large power loses within the system as well as a very short operating life of the system components [4, 5]. An English engineer, named Anthony George Maldon Michell, investigated a means of supporting the large thrust loads of a hydroelectric generator. Applying Reynolds' lubrication equation (2.1), discussed below, Michell developed a design which allowed a pad to tilt to any position, such that the hydrodynamic load was positioned at the pads' optimum placement.

The design consisted of a series of pads, which replaced the lower metal surface, positioned around the main shaft, each pad being allowed to pivot independently and separated from the counter face, also known as the collar, by a pressurised thin film lubricate, as shown in Figure 2.1 and Figure 2.2.

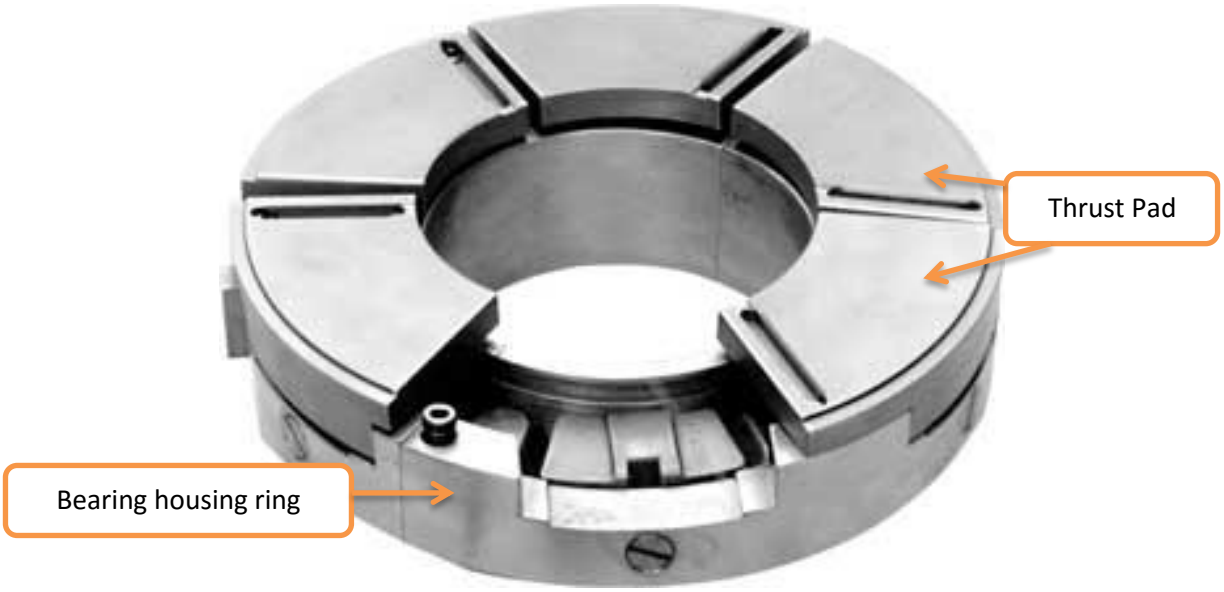

Figure 2.1 A thrust pad bearing ring showing five pads, with space for a sixth [6]

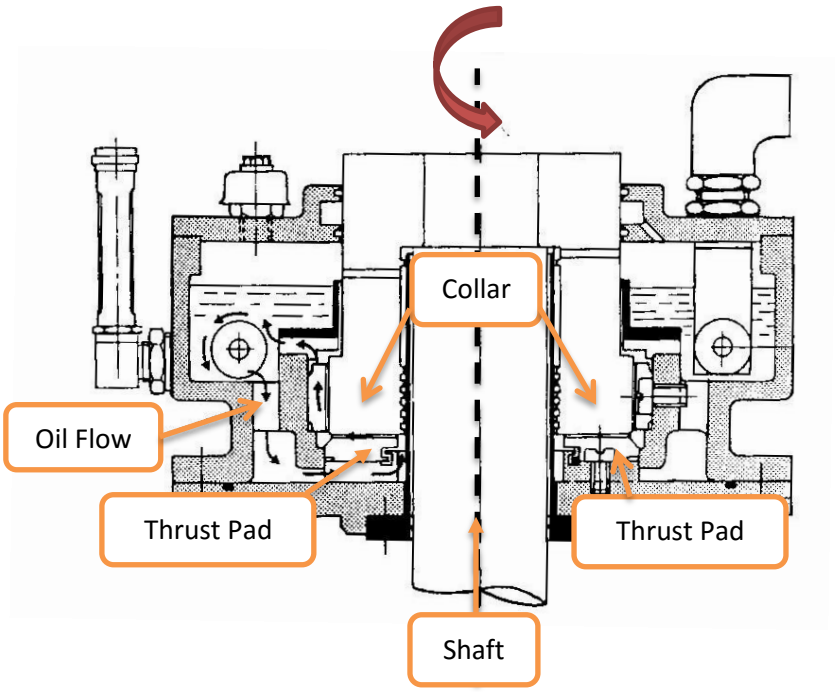

Figure 2.2 Thrust bearing configuration [3]

Michell [4] developed a design for a bearing pad which, as the bearing rotated, the pressure within the fluid film caused the pad to tilt, causing a converging gap to occur between the pad and collar. Pressurised fluid developed within the gap, maintaining a fluid film separating the bearing from the collar, thereby reducing the wear that the pad

experienced. As the speed and pressure increase, the bearings' tilt angle changes to the optimum angle such that the centre of pressure is positioned over the pivot position.

The bearing design put forward by Michell allowed for an increase in the mean load-carrying capacity when compared to the contact bearings used previously, in some cases increasing the load capacity by an order of magnitude [4]. Michell's thrust bearing design was implemented in World War 1 and, due to its success at increasing speeds for naval ships, it became common practice for thrust bearing to be incorporated into most ship propeller designs before coming common place in engines and rotating shaft systems.

2.1.2 Computational Modelling of Thrust Bearings

Bearing design was a matter of trial and error for many decades, with companies knowing from experimental test what loads different sized pads could accommodate. This process was not cost affective and once computers had developed significantly, Ettles [2] developed a code which would predict the film thickness and temperature of a pad. These simulations were used in the design process of a bearing and verified by experimental work. Ettles model used the energy equation and Reynolds lubrication equation simultaneously to predict the temperature and load distribution across the pad face. The results from Ettles model, which was the first application of the lubrication and energy equations to thrust bearings, were compared to published experimental results and the model was proven to accurately predict the pressure and temperature within 90% of the experimental results. Since Ettles first work, many improvements have been made to the model, increasing the accuracy of the results, by several authors, Markin, Fillon, Jiang and Ettles [2, 7-9] , which are discussed below.

All of the simulations to date use Dowson's elasto- hydrodynamic lubrication (EHL) equations [10] to simulate the pressure generated within the thrust pad as discussed in the following sections.

2.1.3 Reynold's Equations

Dowson [10] showed that by considering the Navier-Stokes equations and following the work of Reynold [11] and Pia [12], velocity in the *x, y* and *z* direction respectively, can be shown to reduce to equation 2.1.

$$\rho\frac{\partial u}{\partial t} = \rho X - \frac{\partial p}{\partial x} + \frac{2}{3}\frac{\partial}{\partial x}\mu\left(\frac{\partial u}{\partial x} - \frac{\partial w}{\partial z}\right) + \frac{2}{3}\frac{\partial}{\partial x}\mu\left(\frac{\partial u}{\partial x} - \frac{\partial v}{\partial y}\right) + \frac{\partial}{\partial y}\mu\left(\frac{\partial u}{\partial y} + \frac{\partial v}{\partial x}\right) + \frac{\partial}{\partial z}\mu\left(\frac{\partial w}{\partial x} + \frac{\partial u}{\partial z}\right) \quad 2.1$$

$$\rho\frac{\partial v}{\partial t} = \rho Y - \frac{\partial p}{\partial y} + \frac{2}{3}\frac{\partial}{\partial y}\mu\left(\frac{\partial v}{\partial y} - \frac{\partial u}{\partial x}\right) + \frac{2}{3}\frac{\partial}{\partial y}\mu\left(\frac{\partial v}{\partial y} - \frac{\partial w}{\partial z}\right) + \frac{\partial}{\partial z}\mu\left(\frac{\partial v}{\partial z} + \frac{\partial w}{\partial y}\right) + \frac{\partial}{\partial x}\mu\left(\frac{\partial v}{\partial x} + \frac{\partial u}{\partial y}\right)$$

$$\rho\frac{\partial w}{\partial t} = \rho Z - \frac{\partial p}{\partial z} + \frac{2}{3}\frac{\partial}{\partial z}\mu\left(\frac{\partial w}{\partial z} - \frac{\partial u}{\partial x}\right) + \frac{2}{3}\frac{\partial}{\partial z}\mu\left(\frac{\partial w}{\partial z} - \frac{\partial v}{\partial y}\right) + \frac{\partial}{\partial x}\mu\left(\frac{\partial w}{\partial x} + \frac{\partial u}{\partial z}\right) + \frac{\partial}{\partial y}\mu\left(\frac{\partial w}{\partial y} + \frac{\partial v}{\partial z}\right)$$

In the equation,ρ is the density of the fluid in kg/m^3, μ is the viscosity in Pa s, *p* is pressure in Pa and *u, v, w* are the velocity in the x, y, z directions measured in m/s. The left hand side of the equations, present in equation 2.1, represents induced flow, whilst the right hand side of the equation allows for shear flow and flow due to pressure gradient to be observed.

From this point onwards in the derivation only the x-direction will be considered, as the following steps can be applied in a similar manner to all three directions. Equation 2.1 showed that the inertia force of the fluid, shown on the left hand side of the equation, is a function of the body force, pressure and viscous forces, as shown on the right hand side of the equation. Assuming the two surfaces to be near parallel, it can be seen that the inertial force term tends towards zero. Reynolds [11] showed that the body force could be

counted as negligible when compared to the pressure and viscous forces, which lead to the conclusion that the pressure force and viscous force were in equilibrium, reducing equation 2.1 to a simpler form, as shown in equation 2.2.

$$\frac{dp}{dx} = \frac{2}{3}\frac{\partial}{\partial x}\mu\left(\frac{\partial u}{\partial x} - \frac{\partial w}{\partial z}\right) + \frac{2}{3}\frac{\partial}{\partial x}\mu\left(\frac{\partial u}{\partial x} - \frac{\partial v}{\partial y}\right) + \frac{\partial}{\partial y}\mu\left(\frac{\partial u}{\partial y} + \frac{\partial v}{\partial x}\right) + \frac{\partial}{\partial z}\mu\left(\frac{\partial w}{\partial x} + \frac{\partial u}{\partial z}\right) \quad 2.2$$

Dowson [13] showed that equation 2.2 could be reduced further by considering the fluid as a thin film i.e. the length of the film was an order of magnitude greater than the height of the film. This assumption shows that the x and y velocity components, with respect to the z direction, are of a greater order of magnitude than the velocity in the z-direction, w. For this reason, it was concluded that pressure variations in the z-directions can be neglected allowing for the equation to be simplified further, and for the pressure gradient in the x and y direction to be obtained as shown in equation 2.3.

$$\frac{\partial p}{\partial x} = \frac{\partial}{\partial z}\left(\mu\frac{\partial u}{\partial z}\right)$$
$$\frac{\partial p}{\partial y} = \frac{\partial}{\partial z}\left(\mu\frac{\partial v}{\partial z}\right) \quad 2.3$$

Integrating equation 2.3 twice, with respect to z, results in expressions for the velocities in the x and y directions as shown in equation 2.4.

$$u = \frac{\partial p}{\partial x}\int\frac{z}{\mu}dy + A\int\frac{dz}{\mu} + C$$
$$v = \frac{\partial p}{\partial y}\int\frac{z}{\mu}dz + B\int\frac{dz}{\mu} + D \quad 2.4$$

A, B, C and *D* are constants of integration. Assuming that viscosity is constant in the z-direction, and applying boundary conditions as follows, equation 2.4 expands to equation 2.5. The boundary conditions applied are $U=U_1$ and $V=V_1$ at $Z=0$, and $U=U_2$ and $V=V_2$ at $Z=H$,

where U_2 and V_2 is the velocity of the fluid at the counter surface in the x, y direction, and U_1, V_1 is the velocity of the fluid at the thrust bearing pad surface in the x, y direction. In equation 2.5 H is the film thickness.

$$u = \left(1 - \frac{z}{H}\right)u_1 + \frac{z}{H}u_2 - \frac{\partial p}{\partial x}\frac{z(H-z)}{2\mu}$$
$$v = \left(1 - \frac{z}{H}\right)v_1 + \frac{z}{H}v_2 - \frac{\partial p}{\partial x}\frac{z(H-z)}{2\mu} \qquad 2.5$$

By applying equations 2.5 to the continuity equations and integrating the resultant equations, with respect to z, the Reynolds equations are derived. The limits used in the integration are y=0 and y=H. This allows for the general form of the Reynold's equations to be generated as shown is equation 2.6.

$$\frac{\partial p}{\partial x}\left(\frac{\rho H^3}{12\mu}\right) + \frac{\partial p}{\partial y}\left(\frac{\rho H^3}{12\mu}\right) = 6\left(\frac{\partial}{\partial x}[\rho H^3(u_1+u_2)] + \frac{\partial}{\partial y}[\rho H^3(v_1+v_2)] + 2\frac{\partial}{\partial t}(\rho H)\right) \qquad 2.6$$

Considering 2D flow in the x-y plane only allows for w_1 and w_2 to be set to zero. Defining $U = \frac{u_1+u_2}{2}$ and $\mathrm{V} = \frac{\mathrm{v}_1+\mathrm{v}_2}{2}$, and assuming H does not vary in the x and y direction, then equation 2.6 reduces to the following;

$$0 = -\frac{\partial p}{\partial x}\left(\frac{\rho H^3}{12\mu} + \frac{UH}{2}\right) - \frac{\partial p}{\partial y}\left(\frac{\rho H^3}{12\mu} + \frac{VH}{2}\right) \qquad 2.7$$

Equation 2.7 is the simplified form of Reynolds' lubrication equation, put forward originally by Reynolds[11] which has been implemented, in some form, into most computational models of thrust bearings, and represents the lubrication aspect of the EHL equation. The other aspect of EHL theory is the stress within the pad due to pressure from the fluid. This will be considered next.

2.1.4 Elasto- Hydrodynamic Lubrication Theory

It has long been established that there are three main friction regimes when a lubricant is present between two surfaces [14];

- Boundary Layer Lubrication
- Mixed Lubrication
- Hydrodynamic lubrication

These regimes are shown best shown via a Stribeck curve, as shown in Figure 2.3, which shows the effect on coefficient of friction within the different lubrication regimes.

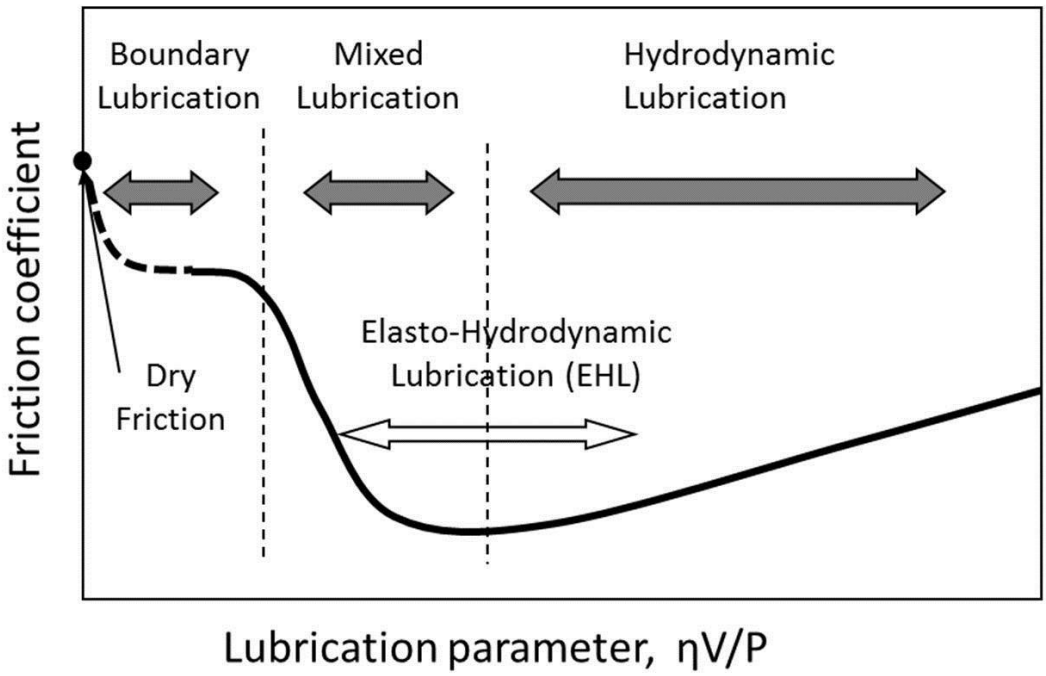

Figure 2.3 Stribeck curve showing different lubrication regions, where η is viscosity, V is the velocity of the fluid and P is the load applied [15]

Boundary lubrication occurs when two surfaces are in contact with each other, and even though a lubricant is present, most of the two surfaces are touching, as shown in Figure 2.4. This contact creates areas of high friction for a low pressure. The lubricant is

present within the micro grooves between the two surfaces, created by the surface roughness. Within this regime, significant heat energy is created, causing high wear rate of the surfaces.

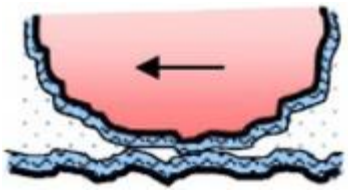

Figure 2.4 Diagram to show boundary lubrication regime [16]

As rotational speed increases, a mixed regime is reached, as shown in Figure 2.5. This is when a fluid film is present, but some contact between the surfaces occurs. As speed increase the coefficient of friction decreases, as more fluid film lubrication is occurring.

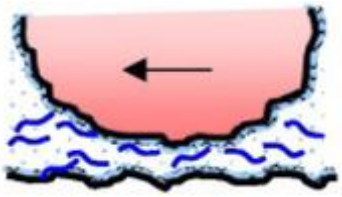

Figure 2.5 Diagram to show mixed lubrication regime [16]

Once a full fluid film has been reached, a hydrodynamic lubrication regime is present, shown in Figure 2.6. This is when a fluid film is formed between the two surfaces, and no contact is occurring. Within this domain, the coefficient of friction increases as speed increases but at a relativity slow rate.

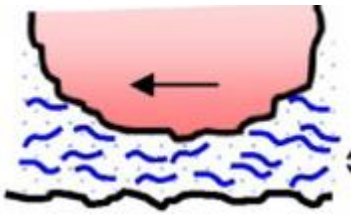

Figure 2.6 Diagram to show hydrodynamic regime [16]

Between the mixed and hydrodynamic lubrication regime, elastic- hydrodynamic lubrication occurs. This is an area of high pressure, minimum coefficient of friction and

small film thickness. Within this regime, elastic deformation of the boundary surfaces occurs due to the high pressure generated by the fluid. This deformation has a significant effect on the fluid film thickness [17]. It was observed by Dowson and Cameron that a thrust bearing typically operates within the EHL region [10, 18].

Using these fundamental concepts, Ettles [2] developed a computer model for a thrust pad bearing which would predict the pressure and film thickness of a bearing [2]. This allowed for optimal design of a bearing to be considered before the bearing was manufactured, reducing the number of failure pads and increasing efficiency of the bearings.

2.1.5 Thermal Properties in a Fluid Film

Along with the pressure profile of the pads, bearing design required that the model also simulated temperature profiles of the pad material, so that a deeper understanding of the conditions seen by the bearings could be made. To do this Ettles [2] applied Pia's energy equation (1956) [12], also known as the general energy equation, to successfully predict the temperature rise generated within the fluid film. The general energy equation is as follows;

$$\rho \frac{dE_I}{dt} = \left[\frac{\partial}{\partial x}\left(K\frac{\partial T}{\partial x}\right) + \frac{\partial}{\partial y}\left(K\frac{\partial T}{\partial y}\right) + \frac{\partial}{\partial z}\left(K\frac{\partial T}{\partial z}\right)\right] - p\left(\frac{\partial u}{\partial x} + \frac{\partial v}{\partial y} + \frac{\partial w}{\partial z}\right) + \varphi \qquad 2.8$$

In equation 2.8, K is the thermal conductivity; T is the temperature; E_I is the internal energy of the system, φ is the viscous dissipation, also known as the viscous heat generation term and t is time. Equation 2.8 allows for the temperature within a system to be found by considering the four governing terms. These terms are the total energy with the system, shown in the yellow box, heat transfer by conduction shown in the blue box, adiabatic compression shown in the green box and viscous dissipation shown in the red box. Dowson [13] showed that the viscous dissipation term can be set to equal the following for thin film fluids:

$$\varphi = \mu\left[\left(\frac{\partial u}{\partial z}\right)^2 + \left(\frac{\partial v}{\partial z}\right)^2\right] \quad 2.9$$

It can be assumed that the rates at which heat can be conducted within the film, across the pads surface, i.e. in the x and y direction is of an order of magnitude smaller than the z-direction conduction rate meaning they can be counted as negligible. The final energy equation is obtained by applying these assumptions to equation 2.8, allowing for the change of temperature through the fluid to be found as a function of velocity of the fluid as shown in equation 2.10, where C_p is the specific heat capacity at constant pressure.

$$K\frac{\partial^2 T}{\partial z^2} + \mu\left(\left(\frac{\partial U}{\partial z}\right)^2 + \left(\frac{\partial V}{\partial z}\right)^2\right) = \rho C_p\left(U\frac{\partial T}{\partial x} + V\frac{\partial T}{\partial y} + W\frac{\partial T}{\partial z}\right) \quad 2.10$$

Equation 2.10 has been used by a number of authors, Ettles [3], Glavatskih – Fillon [7] and Jiang [3, 7, 9], to predict the heat generated within the fluid film and therefore through the pad, allowing for operational conditions to be predicted.

It can be assumed that the temperature of the fluid and the pad at the fluid-pad interface is equal. Using this assumption, several models have been produced which predict the heat through the pad [7, 9, 19-21] due to the heat generated by the fluid, all of which use equation 2.11, known as the thermal conduction law.

$$\frac{\partial^2 T}{\partial x^2} + \frac{\partial^2 T}{\partial y^2} + \frac{\partial^2 T}{\partial z^2} = 0 \quad 2.11$$

Using the equations described above, several authors [9, 22] have produced models, which accurately predicted the temperature of the pad and fluid film as well as the pressure at the fluid-pad interface, both in Babbitt and PTFE pads for a range of different pad sizes, facing material and operating conditions.

However it was observed by Ettles and Cameron [23] that the viscosity of the oil entering the system (the fresh oil supply) was greatly different from the oil entering the leading edge of the film. It was suggested that this was caused by temperature being carried over between pads, and it was concluded that up to 95% of the hot oil leaving the trailing edge of one pad entered the next pad. Ettles went on to put forward a boundary condition for the leading edge of a pad [38] which used the temperature leaving the pad and the oil supply temperature, to determine the oil temperature entering the next pad. This effect, known as the 'Hot oil carryover' is described in equation 2.12, which predicts the temperature at the leading edge of the pad, or inlet, shown by T, by considering the fresh oil supply (T_{sup}), the temperature leaving the previous pad (T_{out}) and the hot oil carryover coefficient (k), which was determined from experimental data, and was itself a function of rotational speed.

$$T = T_{sup}\frac{1-\mathrm{k}}{1-1/2\mathrm{k}} + T_{out}\frac{1/2\mathrm{k}}{1-1/2\mathrm{k}} \qquad 2.12$$

The relationship between k and speed was inversely proportional, meaning that as speed increased, the hot oil coefficient decreased. Thus the temperature of the oil entering the pad, if the oil supply and exit oil temperature remained constant, would decrease as the temperature of the oil entering the pad was directly proportional to the hot oil carry over coefficient.

This method of predicting the temperature at the inlet of the pad allowed for a more accurate prediction to be made, and is now used in most TEHL models.

2.1.6 Thrust Bearing Design

As discussed above, a number of authors have developed thermal EHL models (TEHL) to predict the pressure profile of the pad as well as the temperature profile and conduction through the pad and fluid. These authors have used such models to investigate

the design of bearings. It was observed by Fillon and Glavatskih [22] that a leading and trailing edge gradual change in height, where the pad increase in height from the edge of the pad up to a predetermined location, known as a chamfer, would decrease the oil maximum temperature and the pad maximum pressure allowing for a larger load to be carried. The chamfers were set to cover approximately 10% of the pads' surface, with a larger chamfer at the leading edge. The study concluded that the chamfer was also required to help define the oil film profile during start up and shut down, which in turn helped reduce the chance that the counter face and pad would come into contact leading to severe wear. Within this study, Fillon and Glavatskih[22] also undertook a detailed study of the optimum dimensions of a pad's chamfers, considering the leading and trailing edges separately. It was found that increasing the height and length of the chamfers increases the maximum pressure experienced by the pad and reduces the minimum film thickness whereby increasing the load carrying capacity of the pad by a small amount [22]. The study also looked at how the thickness of the facing material of the pad, in this case virgin Polyterafluoroethylen (PTFE), affects the performance of a pad and it was observed that increasing the thickness of the facing material increased the maximum temperature and stress present within the pad whist reducing the oil film thickness.

Fillon and Glavatskih [22] undertook an experimental study, within the same published work, and found that bearing power loss increased at a faster rate than the rate the bearing size increased. A compromise between pad size and pad efficiency has had to be adopted within industry as a smaller pad, though more efficient in terms of power loss, has a lower load carrying ability then a larger pad. Whilst guidelines have been set out for the size of bearing to load carrying capacity required, industrial companies have their own 'in-house' guidelines based upon many years of experience of manufacturing thrust bearings [1].

As larger hydroelectric generators were developed, larger pads were required to withstand larger loads as well as operate under higher pressures and temperatures. It was found that the simple line pivot system was no longer viable for large bearings, as larger pads need to pivot in the y direction as well as the x direction to allow for the centre of pressure to line up with the pivot position. This was due to the movement of the centre of pressure being in a much larger range than for a smaller pad, due to the size, and as the pad size increase. This led the way for circular pivot systems, as shown Figure 2.7 to be designed along with spring supported systems as shown in Figure 2.8. These systems are used for large bearings but are not required in smaller bearing designs as the centre of pressure location is never far from the pivot position [24].

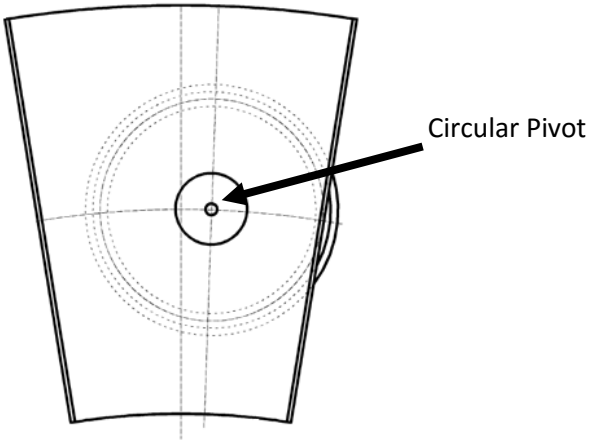

Figure 2.7 Example of a circular pivot system [24]

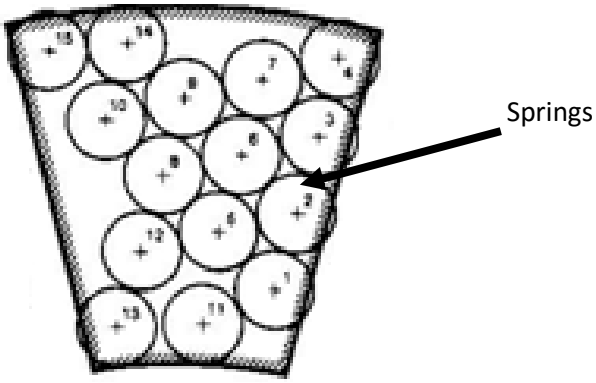

Figure 2.8 Example of spring support system [24]

The surface pattern of the pad and how it affects the performance of the bearings has also been investigated. Glavatskih and McCarthy [25] conducted an experimental investigation into micro-patterns on the surface of the pads and their effect on performance, whilst Sahlin et al. [26] conducted a computational investigation into the effect of surface profile. The study's main focus was the effect of micro-patterns within the pads on power-loss, operating temperatures and oil film thickness. A micro-pattern is a small decrease in the localised pad thickness, at specific points across the pad surface usually positioned as a pattern around the pad, in such a way to direct fluid flow from one area to another area of the pad. Both studies concluded that if a pad has a micro-pattern on its surface then the pad temperature decreased by a maximum of $5^{O}C$, whilst the film thickness increased at the leading and trailing edge. This led the authors to suggest that using micro-patterned pads could lead to a slight increase in the load carrying capacity of the bearings whilst decreasing the maximum temperature experienced by the pad. It was concluded that this was in part due to the formation of vortices within the micro-pores.

2.2 Bearing Material

When Michell was designing his original bearing design, several materials were considered for the facing pad. The chosen material had to withstand high operating pressures and temperatures and not deform or wear significantly. To ensure the material did not deform too much under hydrodynamic loads when at operating pressure and temperature conditions, a high Poisson's ratio was required as well as a high Young's modulus. Both of these properties are a function of temperature, and a material had to be selected where the mechanical properties did not change dramatically with temperature. This was so that once the material had been machined to the required tolerances; the bearing pad could operate within safety margins without significantly changing shape [1].

The material chosen for this application was called white-metal, also known as Babbitt metal. This composite of this material was a tin or lead based mixture of antimony, copper, iron, aluminium and zinc. Babbitt composites exhibit low coefficients of friction and wear rates, as well as predictable behaviour even in the absence of an adequate lubricate [27]. Table 2.1 shows some of the mechanical properties of Babbitt metal.

Table 2.1 Mechanical properties of Babbitt metal [2, 28]

Density at 25^{o}C (gm/cc)	7.4
Elastic Modulus (GPa)	50
Thermal Conductivity (W/m.C)	26.2
Poisson's Ratio	0.33

As thrust bearings became more popular in industry, and larger pads were needed to carry larger loads at higher speeds, Babbitt metal started to reach the limit of its performance. The limiting factor for traditional Babbitt facing material was the high temperatures at the centre of the pad, as well as the centre of the trailing edge, due to the pad thermal expansion (also known as thermal crowning). This meant that, at high temperature, the pad would thermally expand so much that the counter surface and pad would come into contact, and damage to the pad would occur in the form of a 'whipping effect' [29], shown in the left hand side of Figure 2.9. This damage can also cause small parts of the pad to 'flake' off the surface, and rotate around the bearing system, causing damage to other pads and leading to a complete failure of the bearing [30]. This damage can be seen in the right hand side of Figure 2.9.

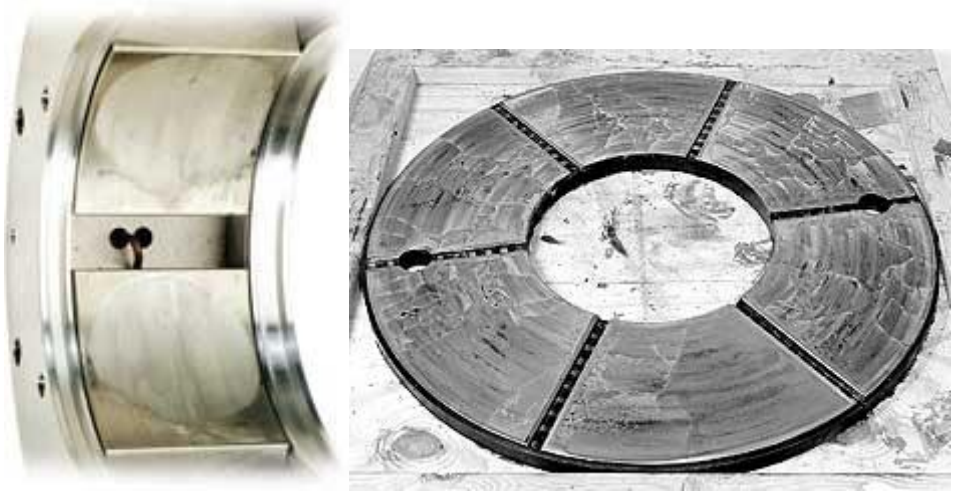

Figure 2.9 Example of damage to pad due to ‘whipping’ and 'flaking' [29]

Russia and the People’s Republic of China started to use polytetrafluoroethylene (PTFE) faced pads in the mid 1970’s [3], due its low coefficient of friction and wear rate [3], and PTFE has since become the industry standard for high performance thrust pad bearings. The use of PTFE meant that a lower peak temperature was seen across the bearing pad face, due to the low thermal conductivity, allowing for a reduction in the amount of thermal crowning that the pad experienced [3]. This reduction in thermal crowning/ expansion, meant that the pad would not come into contact with the counter surface, at the same temperature, leading to a more reliable bearing and a longer lifespan of pads [30]. It has been claimed that the advantages of PTFE over Babbitt metal are as follows [31, 32];

- Reduction in power loss
- Reduction in thermal crowning
- Reduction in pad surface temperature
- No requirement for oil jacking within the system on start-up

- More relaxed manufacturing tolerances on the pad thickness and flatness
- More tolerant to abuse and mishandling

Babbitt metal is still commonly used in a wide range of bearings, but industry is slowly phasing Babbitt pads out and replacing them with PTFE faced pads [3]. Direct comparisons have been made between Babbitt metal and PTFE [3] which demonstrate that PTFE leads to a reduction in thermal crowning and power loss as well as an increased maximum operating pressure and temperature. Thermal crowning is an increase in thickness of the pad material due to thermal expansion which occurs near the centre of pressure, as this is where the highest pressure is located. For these reasons PTFE is also becoming more commonly used in smaller bearing designs.

2.2.1 PTFE Properties

PTFE, also known by the DuPont brand name Teflon, is an addition polymer formed by reacting chloroform ($CHCl_3$) and hydrofluoric acid (HF) in the present of an iron catalysis. Once formed, PTFE is a visco-plastic material, which means that while it can store energy elastically it releases it over a period of time, not instantly like a true elastic material[33]. It is considered a semi-crystalline structure meaning there are areas of crystalline molecular structure present as well as amorphous regions throughout the material.

Two crystalline structures are present within PTFE depending on the temperature of the sample. PTFE can display both triclinic chains which complete a full rotation every 13 atoms, and hexagonal crystallization chains that complete a full rotation every 15 atoms. **Figure** 2.10 demonstrates how the two chains vary at different crystallization states. PTFE displays triclinic crystallization under $19^{O}C$ and above this temperature displays hexagonal crystallization [33].

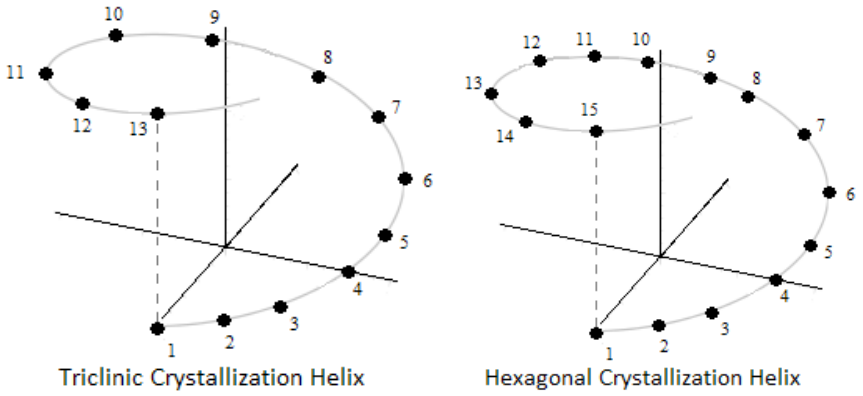

Figure 2.10 Different crystallization helix states

The addition polymerization process produces the PTFE in powdered form. Depending on the rate of polymerization, different size chains are formed creating different sized granules. Once the powder is obtained, the PTFE is formed into sheets by melting the powder in a cycler contained and once set, cut into to form sheets. The melting and setting process takes around 24hours to complete. These sheets are then ready for manufacturing into the required sized pad faces. This process involves loading the PTFE powder into a container, pressurising it with a weight and then slowly raising the temperature. Once at the melting temperature of the PTFE, approximately 327^{o}C, the temperature is held constant for several hours and then slowly brought back down to room temperature. This whole heating process takes 24 hours. When the PTFE is initial loaded into the container before melting of the powder occurs, different materials can be added to the mixture to act as fillers. These fillers change the mechanical properties of the PTFE and different fillers have different degree of effect. These fillers can affect properties such as the wear rate, Young's' modulus, Poisson's ratio, creep rate and coefficient of friction. Typical fillers can include bronze, carbon and polyether-ether-ketone (PEEK) [34-41]. A good comparison of how fillers can change the mechanical properties is between unfilled PTFE and PTFE filled with carbon black. Unfilled PTFE, or virgin PTFE, has a coefficient of friction of 0.11 and wear rate of 9.00x10^{-4} mm^{3}/Nm[34], at standard room temperature under a pin on disk test load of 1MPa and relative velocity of 1m/s on a CMT-1 friction machine. The samples used

had a specific geometric surface area of 14-18 m^2/g. Adding 10% carbon filler increases the coefficient of friction to 0.33[42], which is an undesirable effect but is considered an acceptable trade off when considering the reduced wear rate of $1.14x10^{-5}mm^3/Nm$. Additionally the Young's modulus increases from 279MPa to 496MPa when comparing virgin to carbon-black and graphite filled PTFE [3]. The increase in Young's modulus is good due to the reduction on change of film thickness due to pressure within the fluid film.

The mixture of filler to PTFE considered in this study was 15% carbon black with 2% graphite. Samples of this material were supplied by Fluorocarbon Company Limited to Michell Bearings, Rolls Royce, before being passed on to the author. The mechanical properties of the material were provided via a data sheet, supplied by Fluorocarbon, which is included within appendix I.

As PTFE is a visco-elastic polymer, it experiences creep when under a constant load. Creep is defined as the tendency of a solid to permanently deform under high stress over time. This stress can be below the yield point of the material and the material has to experience the load for a long period of time[36].

A material undergoes 3 stages of creep during its lifespan. These stages are called, primary, secondary and tertiary creep, Figure 2.11 shows an estimation of the creep strain as a function of time, on a material during constant loading [43], as well as an approximation of change in material thickness at each stage, from first loading till failure.

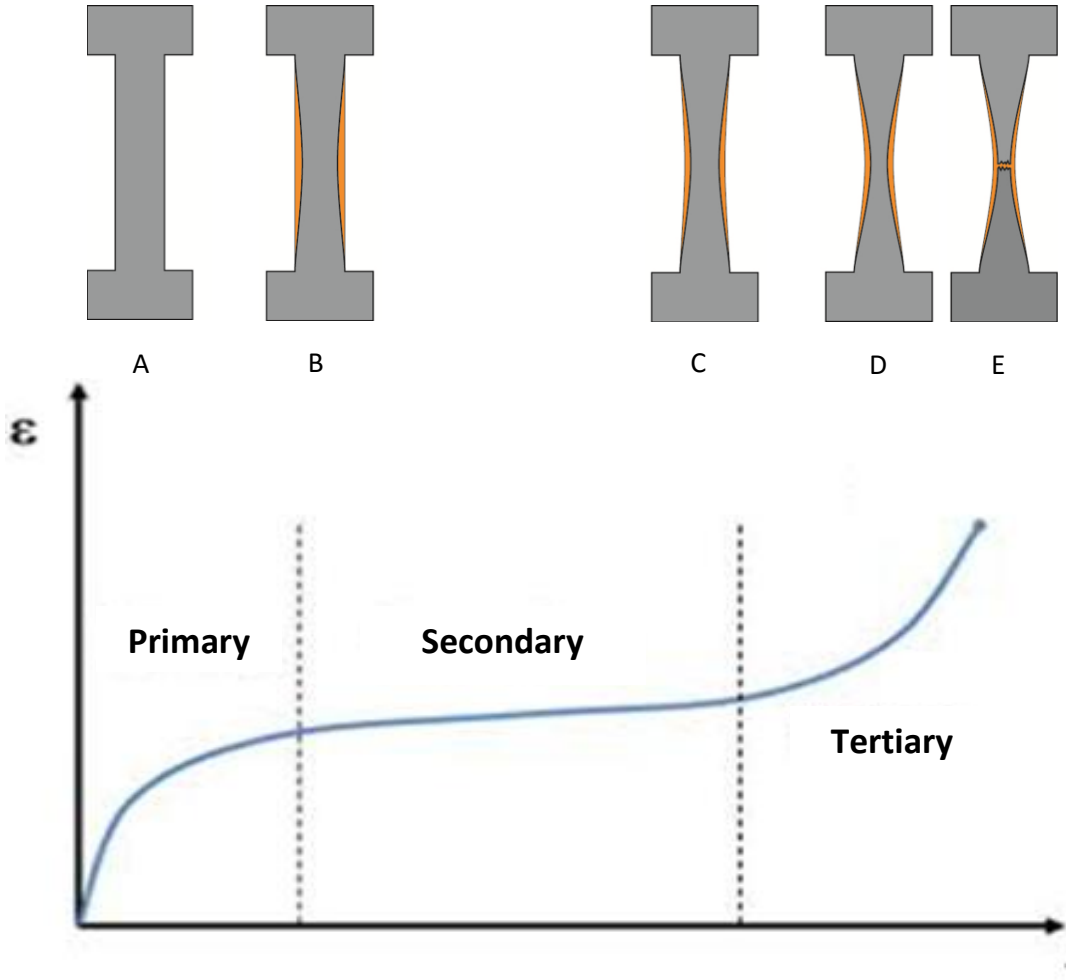

Figure 2.11 Stages of creep during a material's lifespan for a tensile test [6]

When a material is first loaded, it undergoes primary creep, which means a rapid increase in the creep strain occurs, and produces a large initial creep strain rate. This is shown in Figure 2.11 by the rapid decrease in material thickness from drawing A to B. Over time this high strain rate decreases, tending towards a constant value. The duration of this stage depends on the material, but usually accounts for a large amount of deformation. Experimentally, this primary stage of creep is very hard to accurately observe, due to the need to differentiate between primary creep and elastic deformation, which occur almost simultaneously.

Secondary creep is established when a constant creep rate has been achieved, and a material will spend most of its operational lifespan in this stage. During this stage, the creep strain will increase, at a slow linear rate, and will continue to do so for a long period of time. This is shown in Figure 2.11 by the drawings B and C, which shows a gradual decrease in material thickness over a long period of time.

Finally, the material will start to undergo tertiary creep. This only happens if the material is undergoing tensile loading, and leads to failure of the material. During this stage there is a rapid increase in strain rate due to necking of the material [43], shown by drawings C to D in Figure 2.11, before failure and 'necking' in drawing E.

The thrust bearings considered, experience contact load for long periods of time, sometimes for months on end [37] in which time creep effects will occur. From literature it can be concluded that an unfilled sample of PTFE can deform by 2.5% of its original thickness over a 6 month period, under a stress of 8MPa and temperature of 25^{O}C[44]. If this level of deformation was applied to a thrust bearing pad, which is typically 10mm in thickness, that would suggest a change in pad thickness of 250μm due to creep. As the film thickness is typically 10-1000μm thick, then this deformation due to creep could be large enough to significantly affect the load carrying capacity of the pad. These creep effects have not previously been investigated for PTFE faced thrust bearings to date, and the work presented here aims to provide a greater understanding of the effect of creep on bearing performance during its operational life span.

2.2.1 PTFE Experimental Creep Results

Creep results on virgin PTFE have been published by several authors [44, 45], whilst little data on filled PTFE has been published, due to the vast number of possible fillers and ratios of PTFE to filler that can be made. Carbon fibre, graphite and fibre glass have all been shown to increase the creep resistance of PTFE when used as a filler, by

demonstrating a reduced secondary creep rate when compared to virgin PTFE [46, 47]. These blends of filled PTFE are used mainly in rotary, wear and piston seal rings, and to date haven't been used in a thrust bearing application. To date, the only published data on filled PTFE used within a thrust bearing application is the 15% carbon black, 2 % graphite blend, used within this study [3].

From the literature it can be seen that virgin PTFE behaves in a typical manner when compared to the idealised case in Figure 2.11, as shown in Figure 2.12 [45] and Figure 2.13 [44]. It should be noted that both graphs are of compressive creep and the idealised graph is based on tensile loading and a linear axis whilst Figure 2.12 and Figure 2.13 is based on a logarithmic axis. It can be seen that the creep strain rate (slope of the strain vs time curves) is relatively independent of the applied stress over most of the time period considered.

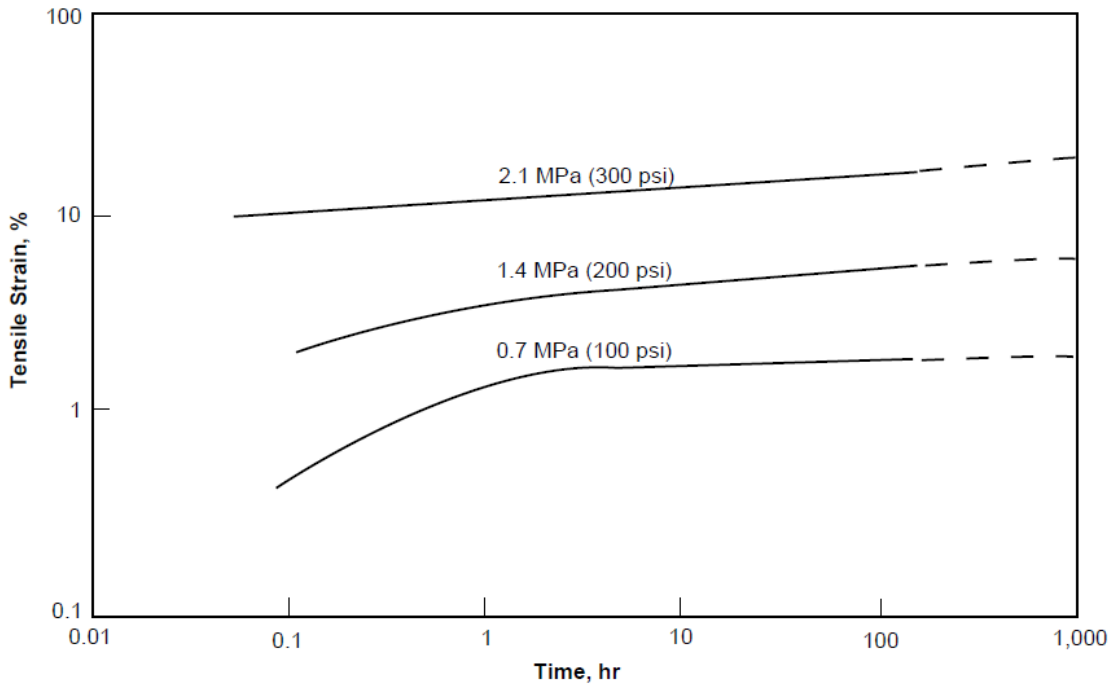

Figure 2.12 Compressive creep for virgin PTFE at varying loads at 200^{0}C [45]

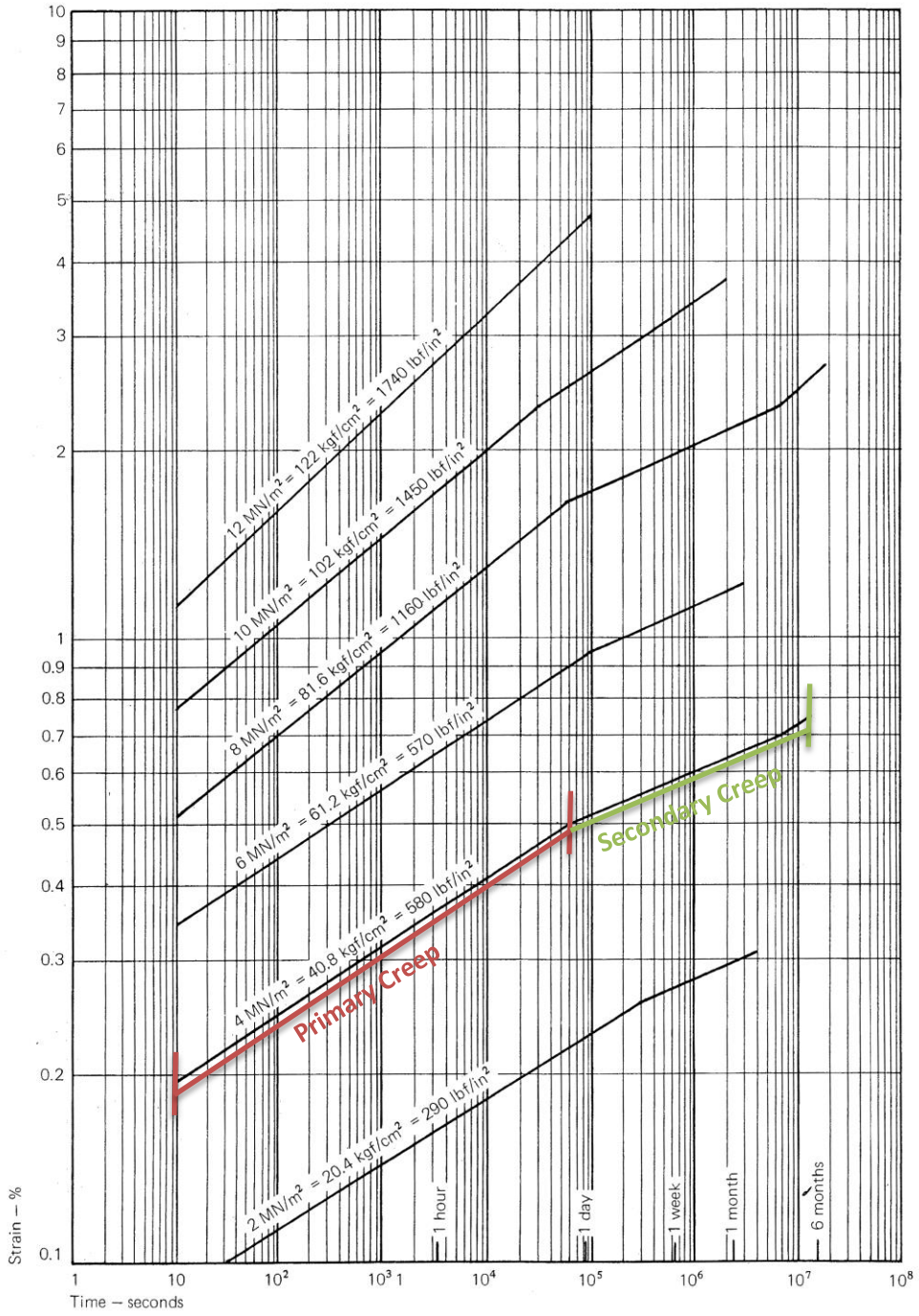

Figure 2.13 Compressive creep results for virgin PTFE at varying loads at 25^{O}C [38]

It can be seen from Figure 2.12 and Figure 2.13 that the strain rates are relatively independent of pressure, and produce very similar strain rates (shown by the gradients of

each curve). The only thing that changes drastically on the curves is the transition time from primary to secondary creep, in which no pattern can be seen. This is shown by Figure 2.13, in which the transliteration from primary to secondary creep appears to be independent of time.

2.2.2 Numerical creep models

The visco-plastic creeping of materials has been understood for some time, with reports of it being found in literature since 1922 [48], but no numerical models for primary secondary or tertiary creep of PTFE has published to date. Using experimental data, Norton [49] put forward a numerical creep function which predicted the secondary creep of a visco-plastic material, as a function of pressure and temperature. This has come to be known as the Norton creep function, and is shown in equation 2.13, in which $\frac{\partial \varepsilon}{\partial t}=\dot{\varepsilon}^{c}$ is the creep strain rate, A and n are material dependent constants,σ is the applied stress, σ_{th} is the threshold stress, Q is the activation energy, T is the absolute temperature and R is the universal gas constant [49].

$$\frac{\partial \varepsilon}{\partial t} = \dot{\varepsilon}^{c} = A(\sigma - \sigma_{th})^{n} e^{\frac{-Q}{RT}} \qquad 2.13$$

Using this equation Norton was able to accurately predict the secondary creep strain rate for several polymers and had limited success with predicting the primary creep rate [49].

Bailey [50] added a time function, called the time hardening function, which allows for more accurate predictions to be made of primary creep. This equation, as shown in 2.14, allows for the primary creep to be predicted in a more accurate manner, due to the time hardening function forcing the primary creep rate to a constant value, which is the definition of a secondary creep rate. Within this equation t is time and m is a material dependent constant, which is always less than 1.

$$\frac{\partial \varepsilon}{\partial t} = \dot{\varepsilon}^c = A(\sigma - \sigma_{th})^n e^{\frac{-Q}{RT}} m^t \qquad 2.14$$

Most computational models use a Norton or Norton-Bailey creep function to predict the primary or secondary creep, with a Norton function being used to predict the secondary creep only, and a Norton-Bailey function used to predict primary and secondary creep [50, 51].

Mukherjee et al. put forward an alternative creep function, partly based on Norton's initial model, which predicts creep as a function of pressure, temperature and grain size, as shown in equation 2.15. Within this equation d is the grain size, G, d and b are material based constants, k is the Botzman constant and D_0 a material based constant at 25^{O}C [51].

$$\dot{\varepsilon}^c = \frac{AGb}{KT} D \left(\frac{b}{d}\right)^p \left(\frac{\sigma}{G}\right)^n = A' e^{\frac{Q}{KT}} \qquad 2.15$$

Where $D = D_0 e^{\frac{-Q}{RT}}$

All of these models have been used for polymers and metals to predict creep strain rate, which in turn can be used to predict the amount of deformation within a material due to creep. As stated previously the Norton creep function can be used for secondary creep, but literature suggest that when predicating primary creep, a Norton-Bailey creep function is more suited to the task. The Mukherjee et al. model is more commonly used with metals than polymers [33, 51].

Whilst PTFE creep experiments have been conducted [44, 45], application of a numerical model to these results has yet to be published within literature. This being said, there is no reason why any of these functions cannot be applied to PTFE.

2.2.3 Manufacture and Construction of Pads

Each sector of the bearing pad ring is made separately, but all are identical. The pad is attached to a steel backing material, which in turn sits on a metal housing rig (see Figure 2.2). Babbitt pads have been constructed in the same manner for many years; the Babbitt facing material and steel backing pad are constructed separately, and machined/polished to the required finished. Once these two parts have been constructed, the Babbitt is heated and melted onto the steel backing material, before a final polish is carried out. PTFE, due to its well-known 'non-stick' properties, cannot be simply stuck or melted onto a steel backing material, so an alternative technique has had to be adopted to attach the PTFE to the steel backing material. The PTFE is heated up to just below melting point, and then forced into a copper mesh. This copper mesh is then soldered onto the steel backing material. .

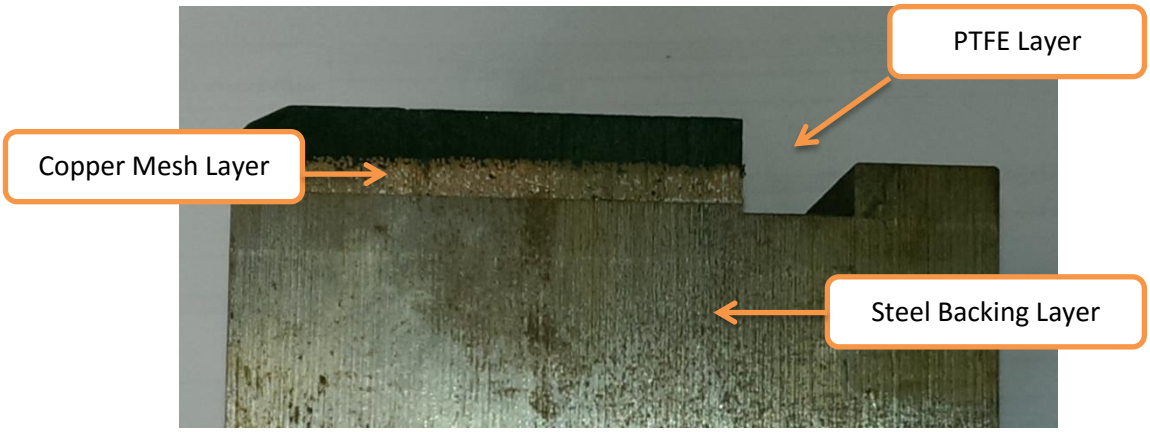

Figure 2.14 Cross section of a pad showing PTFE, Copper and Steel layers

Figure 2.15 Copper mesh used to bond PTFE to steel backing material

From private communications with Michell Bearings, the author was informed that the PTFE and copper mesh layer, shown in Figure 2.15, was of an uneven, near random thickness, with some parts of the pad including much more copper than other parts, shown in Figure 2.14. Due to this randomness and lack of published data on the ratio of PTFE to copper, it has become common practice not to include the copper layer within computational simulations.

2.3 Summary

Within this chapter, a history of modelling of thrust bearings has been presented, along with the equations used to model the bearings. An outline of literature relating to bearing materials, construction techniques and visco-plastic material properties is also presented along with numerical models for modelling visco-elastic creep effects. It is concluded that whilst bearing analysis techniques are quite sophisticated, they do not consider the time-dependent behaviour of the PTFE bearing surfaces that have become the industrial norm material. Although there is some data on the creep properties of unfilled PTFE, there is

very little information on the filled PTFE that are currently being used in tilting pad thrust bearings. This is because the only experimental and computational models for thrust pad bearings published to date are for virgin [2] or filled PTFE [3] (15% carbon black and 2% graphite). Of them only virgin PTFE creep results have been published [44] but not the filled PTFE.

Chapter 3- Experimental Apparatus and Methodology

The purpose of this chapter is to give a clear description of the procedure used to collect the creep data which was then used in the visco-plastic Thermal Elastro-Hydrodynamic Lubrication (TEHL) model as described in later chapters. As the model developed simulated PTFE subjective to a compressive load case, at varying temperatures, material testing apparatus was designed to measure creep under the same conditions. The rig was designed and commissioned at the University of Leeds.

3.1 Design of Experimental Rig

From initial simulations done on the TEHL model, shown in Chapter 5- , and after reviewing literature [2, 22], it was determined that the equipment needed to be suitable for temperatures of 30-200^{O}C and 20 MPa. The PTFE supplied from Flurocarbon Ld., which was used throughout the study, was a 15% carbon-black, 2% graphite blend and was supplied in 5mm thick rectangle sheets of 300x600 mm. From these sheets the PTFE was machined into cylinders for testing of Ø5x10 mm sizing. With the sample sizing determined, the maximum mass required for the stress of 20 MPa, needed to be found using equation 3.1, where m is the required mass, p is the desired pressure, g is gravity and A_s is area of the sample seen by the rig.

$$m = \frac{pA_S}{g} \qquad 3.1$$

With the radius set to 5 mm, and the maximum pressure of 20MPa set, the maximum mass to be applied to a sample was 40.04 kg. During the test cycle some samples, when a large load and temperature were applied, sheared in the horizontal direction to a point of failure. To avoid this, shorter samples of Ø5x5 mm size were tested at the high load and high temperature conditions. This would not affect rate of creep (ε_c) as ε_c is a ratio independent of original height.

The oven used for the experiments had a hole cut into the top and bottom of it from a previous experiment, which allowed for the apparatus to be fitted in and around the oven. As previously stated, the samples only needed to be tested in compression, so a vertically-loaded system was designed. A large plate was fixed on top of a rod, held in place by linear bearings, allowing for the rod to apply the force directly to the sample. A structure was designed around the oven, to hold the linear bearings in place, directly over the top hole within the oven. The sample would be mounted on a cylindrical flat plate during testing. The whole rig was secured to a large base plate. The rig is shown in Figure 3.1 along with an accompanying CAD drawing in Figure 3.2.

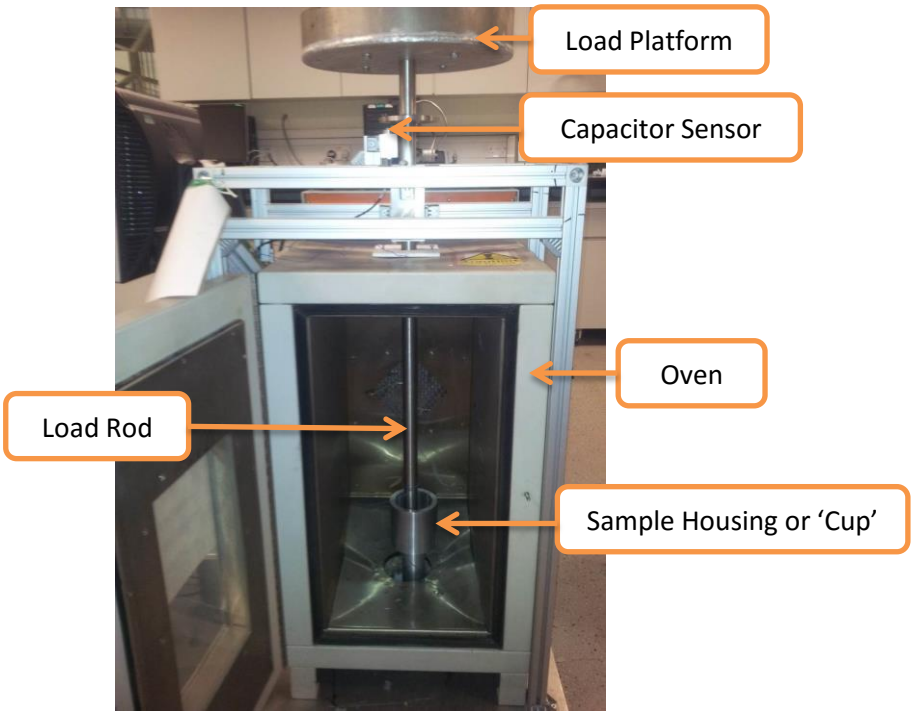

Figure 3.1 Experimental creep rig

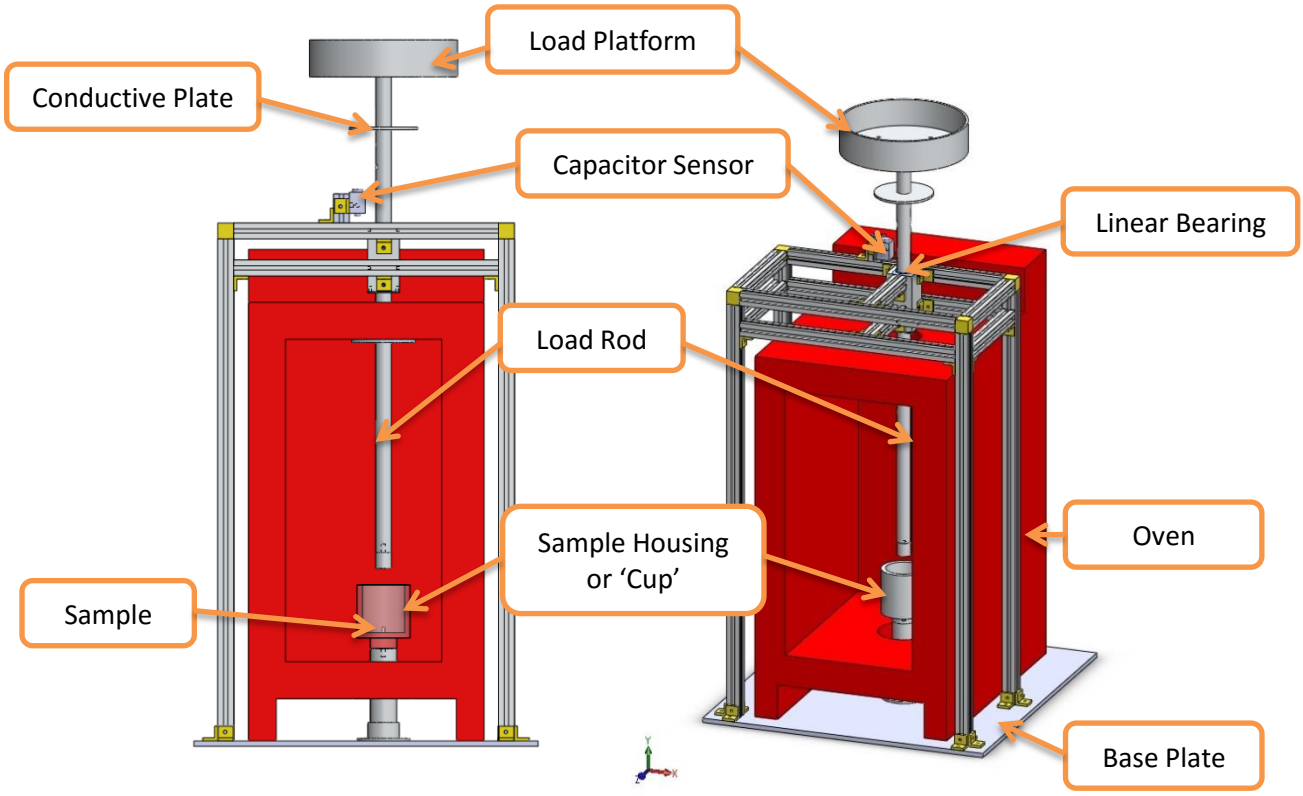

Figure 3.2 CAD drawing of creep testing apparatus

The material used for the load platform, loading rod and base plate was steel. The main structure, to which the loading was connected rod via linear bearings, was made out of Rexroth aluminium bar, engineering drawings for the whole rig can be found in Appendix II. A thermal insulator was attached to the top hole of the rig, with a hole large enough for the loading rod, to reduce the amount of heat loss within the oven. This thermal insulator was made from a machinable glass ceramic which had a maximum continuous operating temperature of 800^{O}C.

The loading rod, shown in Figure 3.3 was manufactured with two holes cut in to it, which allowed for a steel pin to be inserted through it. This allowed an estimate of 95% of the rod, which would be in the oven during testing, to be held within the oven by the pin during the start-up phase of testing, to reduce the amount of thermal expansion seen

during the test. The second hole, allowed for the rod to be kept stationary, by the pin, without resting on any other part of the rig.

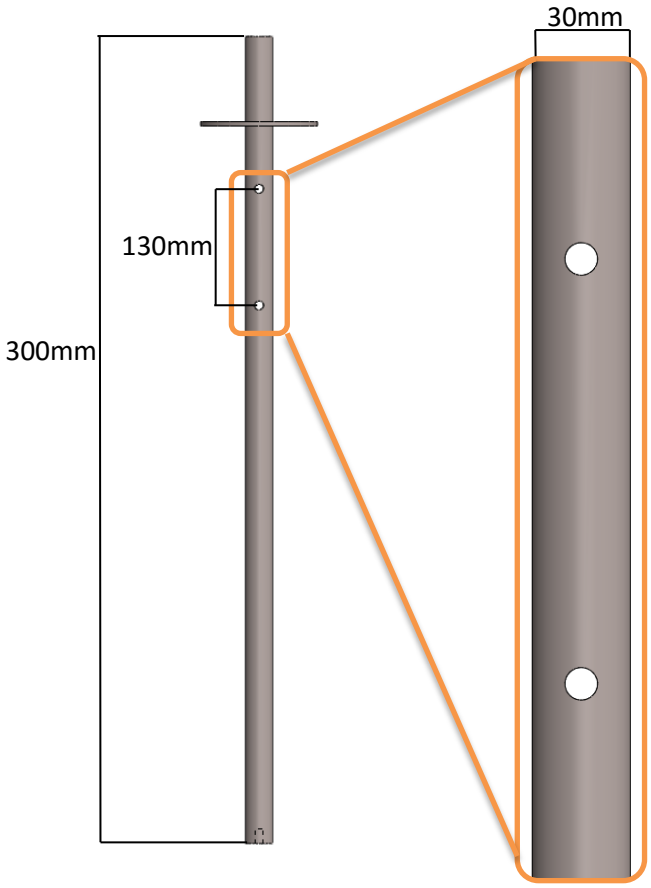

Figure 3.3 Load rod hole locations

The base cylinder for the rig, on which the sample would be mounted and the pressure force reacted, was designed as a 'cup' shape as shown in Figure 3.4. This was to allow other projects to use the rig at a later date, without a new machine part having to be manufactured.

To load the sample accurately for every test, a mark was made on the base rod, or 'cup', marking the centre where the load rod would come into contact with the sample. This allowed for the samples to always be placed at the same point during tests, reducing

the chance of shear or misalignment to take place. The load rod was lowered onto the sample, at a slow speed, to try and reduce the chance of moving the sample. After the tests were completed, the sample was examined for visible signs of shear. If shearing of the sample could be seen, this meant that misalignment had occurred, and the test was marked as failed and repeated. These failed tests were not included within the results presented in the thesis, or in defining the creep function found.

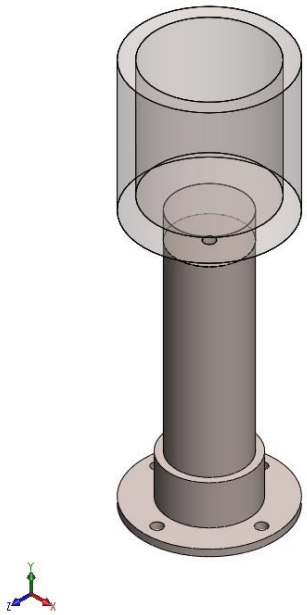

Figure 3.4 Base rod schematic

The procedure for loading the sample is listed on the next page and Figure 3.5 shows the sample resting on the 'cup' with the load rod above it. This is the position that the equipment was left in when the oven was reaching a steady state;

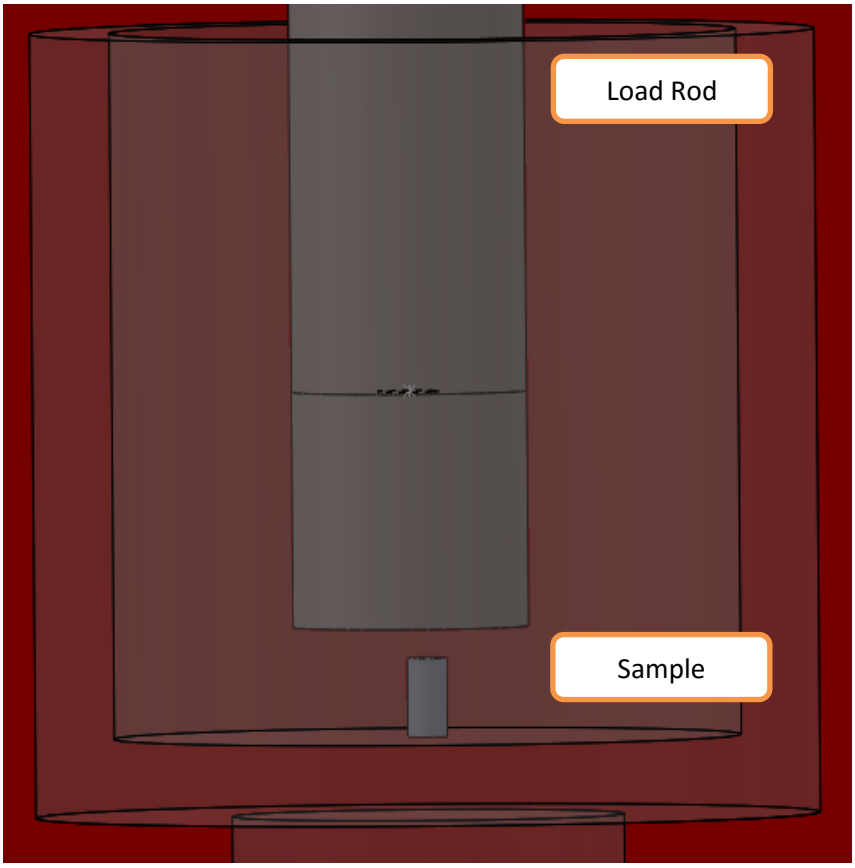

Figure 3.5 Schematic of load rod about to contact with sample after alinement

1. All equipment turned on and checked
2. Steel sample inserted into rig, placed on the sample ‘cup’ plate
3. Loading rod lowered and Labview program started
4. Capacitor sensor moved to allow for largest range. When found, Labview program turned off
5. Load platform raised and metal sample taken out
6. PTFE sample inserted on sample plate
7. Lower load platform lower position and insert pin
8. Labview program started, under name ‘start up’, oven turned on to required heat, and load applied to load platform

9. Once the oven had reached a steady temperature, shown by Labview program, reset Labview, name the Labview save file and start test
10. Lower load platform slowly until contact with PTFE is achieved
11. Leave for 7days, checking intermittently
12. If measured deflection approaches 2 mm, move the capacitor sensor to a to 2mm gap position, recording the capacitor sensor distance from conductive plate before and after movement
13. Once test is complete, stop Labview program and save file
14. Turn off oven
15. One everything has cooled raise load platform
16. Remove sample and label

A sensor was required to capture the deformation of the sample. A capacitor sensor, type a CS2 sensor, was selected, and was bought from Micro-Epsilon UK Ltd. The CS2 sensor, has an operating range of 0-2 mm and a linearity of <0.1% full scale output (FSO). This meant the error due to a lack of linearity was +/-2 µm at full operating range. The capacitor sensor recorded the distance from a fixed point, which had to be made out of an electrically conducting material, so an aluminium plate was attached to the loading rod, as shown in Figure 3.3 called the conductive plate. The sensor housing, shown in Figure 3.2and Figure 3.6, was designed to be moved in the vertical direction. This allowed for the sensor to be moved vertically in case a smaller sample height was required.

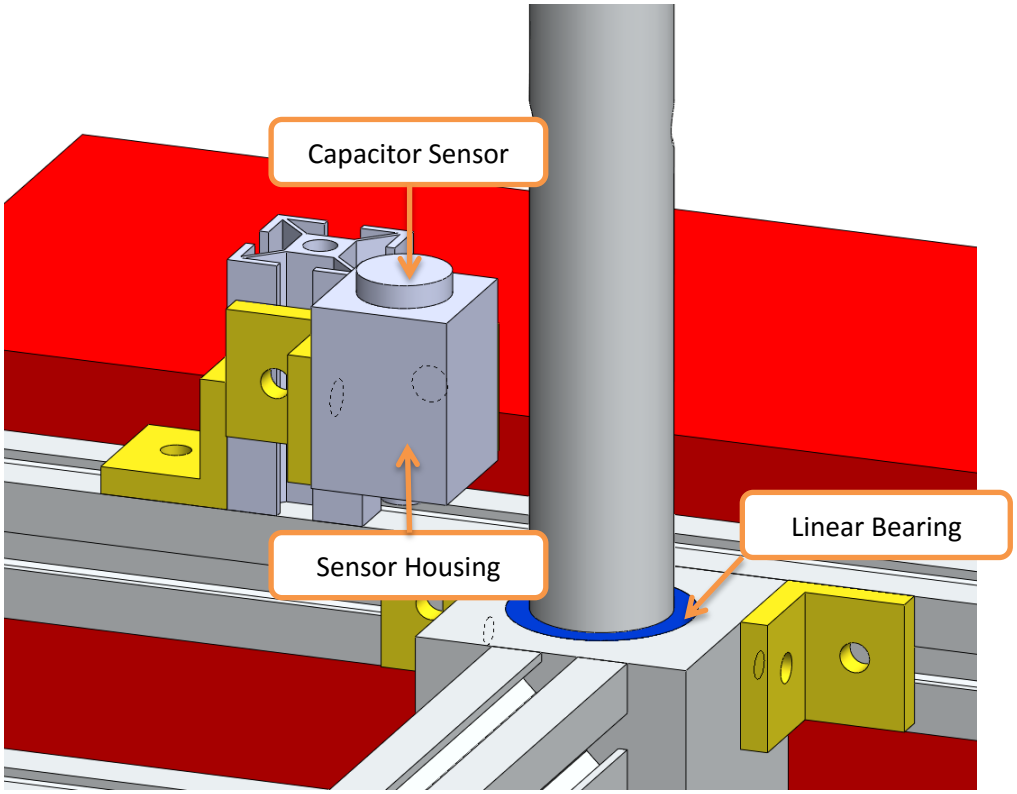

Figure 3.6 Sensor housing diagram

Five thermocouples were placed around the rig, two within the oven, and 3 around the outside of the rig, the placements are shown in Figure 3.7. All thermocouples used conformed to BS 1843 [52]. The thermocouples had a maximum error of +/-3^{O}C. The positions of these thermocouples are shown in Table 3.1 and Figure 3.7.

Table 3.1 Thermocouple location

Thermocouple Number	Location
Thermocouple 1	Inside Oven, Next to Sample
Thermocouple 2	Inside Oven, Back of Oven
Thermocouple 3	Outside Oven, On Top of Thermal Insulating Material
Thermocouple 4	Outside Oven, Next to Capacitor Sensor
Thermocouple 5	Underneath Oven, by Bottom Hole of Oven

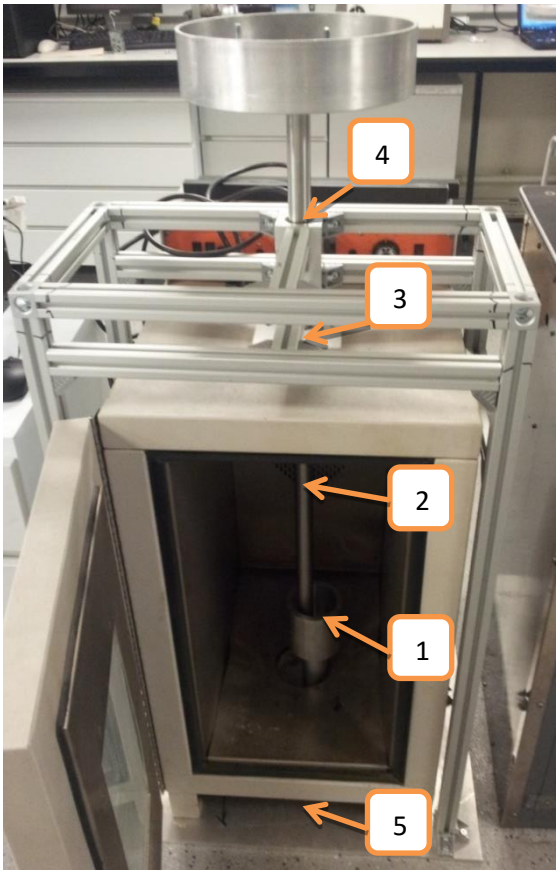

Figure 3.7 Position of thermocouple around experimental rig

The base rod, load platform, linear bearing housing, loading rod and base plate were built at the University of Leeds. The load platform and rod were weighed, to an accuracy of +/-.005kg, as this weight needed to be subtracted from any additional load applied to get the total load seen by a sample. Together the plate and rod weighed 9.30kg; this meant that the total weight needed to be added to achieve the maximum load case was 30.73kg. The weights used during the experiments were a combination of 5, 10, 20 kg weights, and were arranged so that an even weight distribution was achieved.

3.2 Experimental Equipment Validation

Validation of the rig had to be conducted on the equipment before the rig was used, to make sure that the deformation due to loading and thermal expansion was within allowed tolerances.

3.2.1 Displacement due to loading

The displacement due to loading (ΔL) can be found by considering the Young's modulus (E), force applied (F), area the force is applied to (A) and the unloaded thickness of the material (L). The displacement due to loading occurs in the load cell plate in the vertical direction, due to only being loaded in the vertical direction. Using equation 3.2, which is based on the simple definition of Young's modulus, the displacement due to loading could be found.

$$\Delta L = \frac{FL}{AE} \qquad 3.2$$

Using this equation, with E= 205 GPa, A= 0.0028m^2, L= 10mm and F= 196 N, the maximum axial load case that the load cell will experience, the vertical displacement in the top load cell, would equal 3.41nm. As the capacitor sensor chosen had an accuracy of +/- 2 µm, this value for displacement was acceptably low.

3.2.2 Thermal expansion displacement

Displacement due to thermal expansion was found by considering the linear thermal expansion equation, as shown in equation **3.3**.

$$\Delta L = L\alpha\left(T - T_{ref}\right) \qquad 3.3$$

This equation uses the original thickness of the load rod (*L*), coefficient of thermal expansion (α), temperature of rig (*T*) and the starting temperature (30^{O}C) (*T*), to find the amount of deformation experienced during heating (ΔL). Using this equation, it was

predicted that the maximum deformation due to thermal expansion would be 4.16μm, when the rig's maximum operating temperature of 150^{O}C was considered. This is well within the tolerance of 2mm for due to the linear bearing holding the beam in place. This meant that if the beam expanded due to heat during a test, the bearing would still allow the rod to move freely in the vertical direction.

3.3 Stability Test

With the rig built, a stability test was conducted on the equipment for a 30 min time period, where no sample was present and the oven was set to 85^{O}C and the load platform was loaded with 16 MPa. The laboratory was kept at a constant temperature of 25^{O}C at all times. The temperature and distance of the sensor to the datum plate, was recorded over the 30min period. The results from the thermocouples can be seen in Figure 3.8, whilst the displacement results from the capacitor sensor can be seen in Figure 3.9.

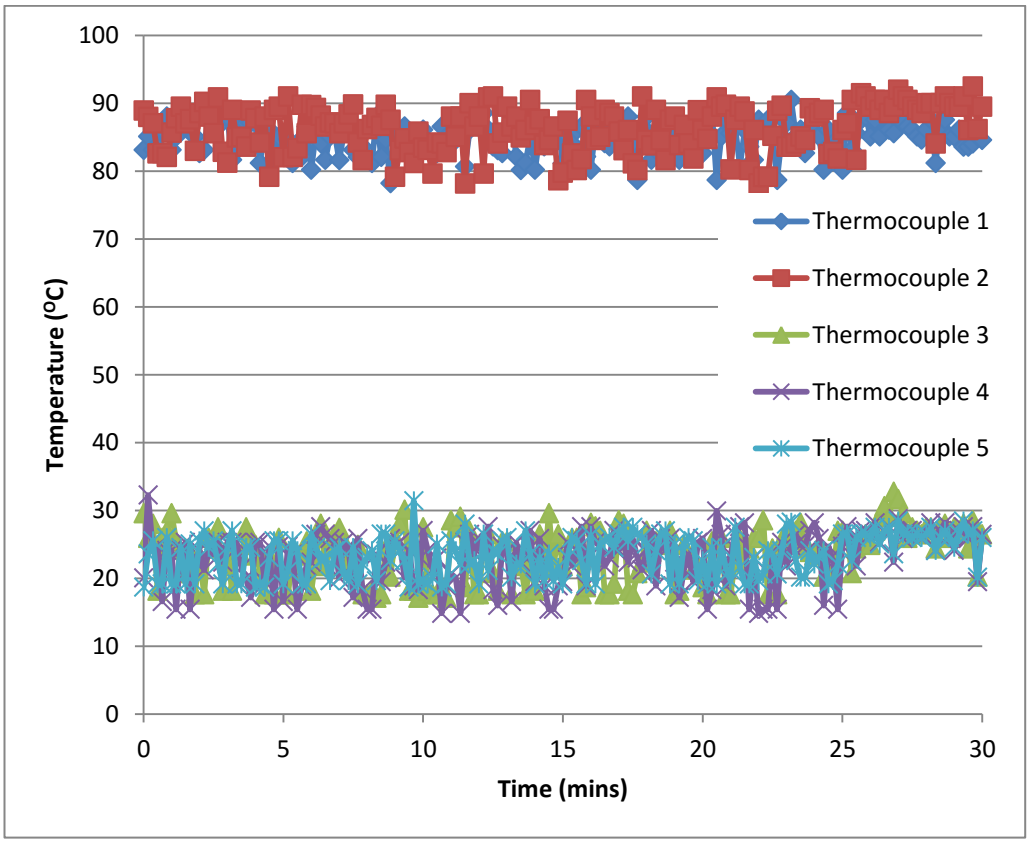

Figure 3.8 Stability test results of thermocouples over 30 minuets

From Figure 3.8 it can be observed that the oven can keep a near constant temperature, with some temperature fluctuations over time, approximately +/-5^{O}C from the desired 85^{O}C

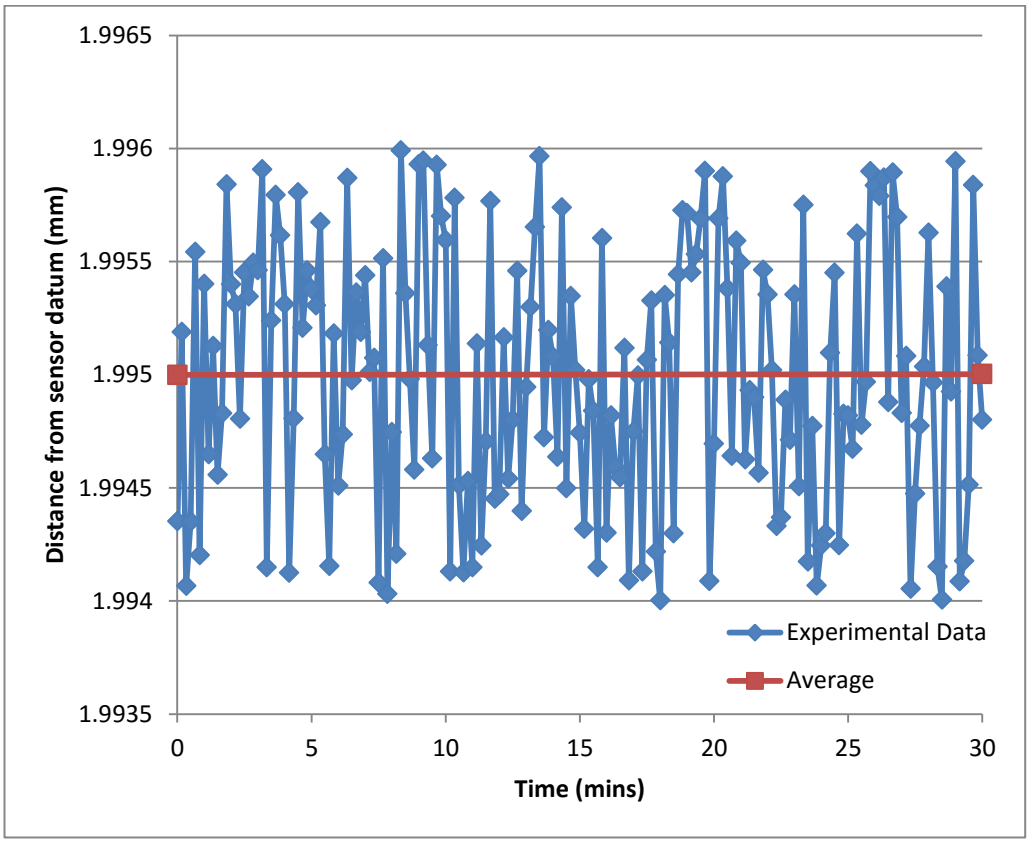

Figure 3.9 Stability test results of capacitor sensor over 30 minutes

From Figure 3.9 it can be observed whilst the desired position of the capacitor sensor was 2 mm away, this being the sensors maximum range, from the conductive plate, the actual position was 1.98 mm. To maximise the range of displacement that the sensor could measure, the start position for the sensor was desired to be 2mm at the start of each test. To achieve this, a steel cylinder sample of 10x10mm was made so that the sensor position could be adjusted before the test was started to allow for the maximum distance between the sensor and the conductive plate to be achieved. Figure 3.9 shows that the capacitor sensor only varies with a +/- 2μm, as advised by Micro-Epsilon UK Ltd, the sensor manufacturing company.

3.4 Summary

A rig has been designed to accurately measure the amount of displacement present within a sample over a large period of time. For a polymer, this displacement will be in the form of creep. This allows for creep tests to be conducted at a range of temperature and pressure cases. The results from these tests are presented in Chapter 4. Once these tests have been completed, a creep function for a filled PTFE was derived, as presented in Chapter 4.

Chapter 4- Experimental Results

Within the following chapter, the experimental results produced by the creep rig are presented, along with the equations used to process the data. A function is then fitted to the creep data, to allow for the prediction of creep strain rate at any given temperature and pressure.

4.1 Experimental Results

As stated in Chapter 3- , tests were conducted at three load cases, 4, 8 and 12MPa, and three temperature cases, 40^0C 90^0C and 140^0C, with all combinations of load and temperature tested. Each test case was repeated twice, with three repeats being conducted for the 12MPa load cases, at all temperature combinations. An additional single test was done at 16MPa and 40^OC. All tests were conducted on 10mm height samples, with a single test being done on a 5mm height sample for each of the following cases; 12MPa 40^0C, 12MPa 90^0C and 12MPa 140^0C. The height of the sample should have no effect on the results, as strain was the variable which was to be used to find the creep function, which is a function itself of the original sample height.

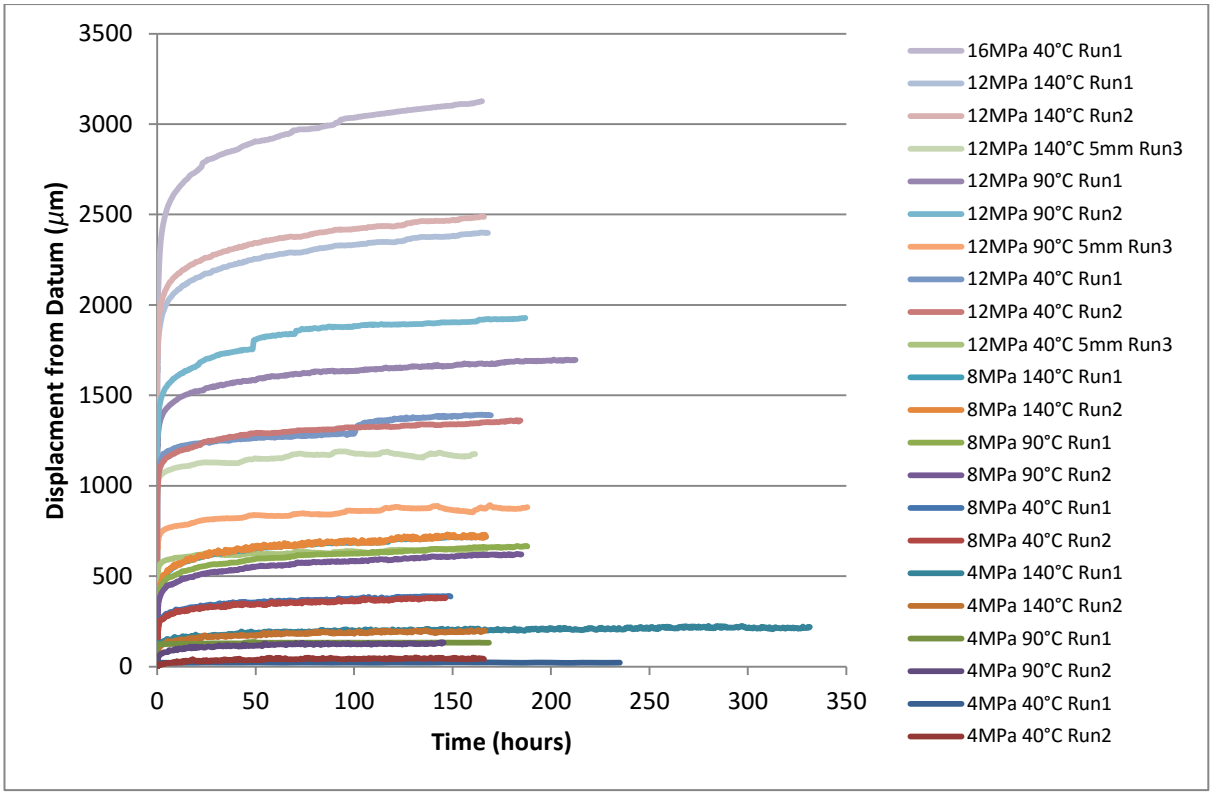

Figure 4.1 Displacement as a function of time from datum due to visco plastic creep effects

Figure 4.1 shows the results gained from the experimental work as a function of displacement. This displacement was found by using equation Figure 4.1, in which the total displacement of the sample (∂) is found by considering the current distance from the datum (∂_n) and the initial distance from the datum ($\partial_{T=0}$).

$$\partial = \partial_n - \partial_{T=0} \qquad 4.1$$

Figure 4.1 shows that, as predicted from the literature review, no tertiary creep was observed. The repeat results show that there was little change between tests. Figure 4.1 shows that some test experienced more than the maximum experimental range 2mm of displacement. When this was the case, before the sensor and datum came into contact, the sensor was moved to a lower position and the new starting distance of the sensor from the datum, was recorded and taken into account when finding the total displacement.

During the tests of 8MPa, 40^0C run1 and 12MPa, 90^0C run2 the sensor and datum came into contact before the sensor could be moved. This can be seen clearly in Figure 4.1 when a sharp, sudden increase appears, during the 8MPa 40^0C test around 95hours of testing, and around 45hours of testing for the 12MPa 90^0C case. This occurred during the night, when there was no access to the experimental laboratory. The effect of this contact did not seem to have a large effect on the results, as the all the repeats show the same trend and are within the same order of magnitude.

The true strain can be obtained from the displacement by using equation 4.2 on the displacement values for each individual case. Equation 4.2considers the original height of the sample (H_s) and the displacement (∂) seen by the sample at each time step to find the true strain of the sample (ε_T) at each time step. Using equation 4.2 allowed for the true strain to be obtained, as shown in Figure 4.2.

$$\varepsilon_T = In\left(1 + \frac{\partial}{H_S}\right) \qquad 4.2$$

In Figure 4.2, the true strain for different specific pressure load cases are shown at three different temperatures per pressure. All the tests have been repeated at least twice, apart from the 16MPa specific load case, in graph c, which was only considered once. Graph A shows the results for 4MPa, graph B shows the results for 8MPa and graph C shows the results for 12 and 16MPa.

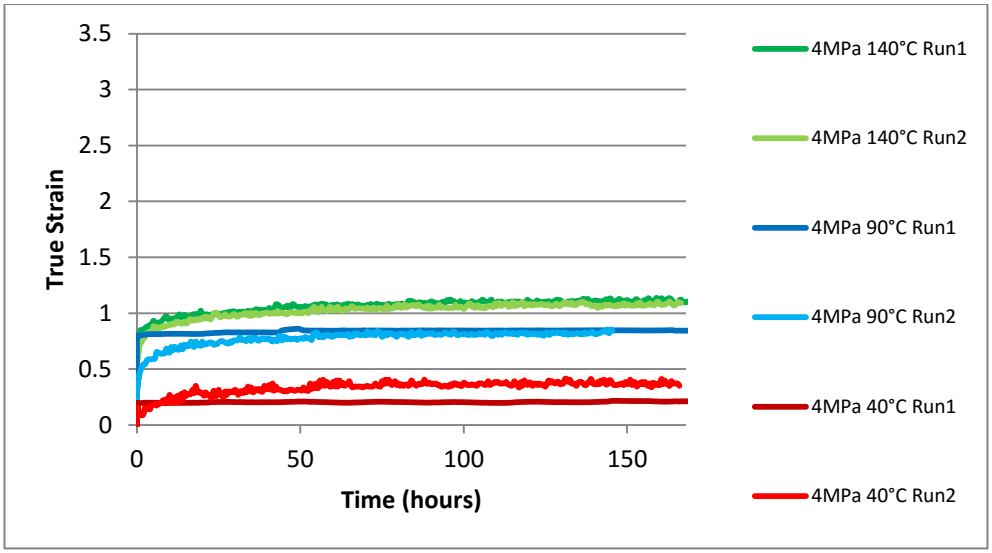

a)

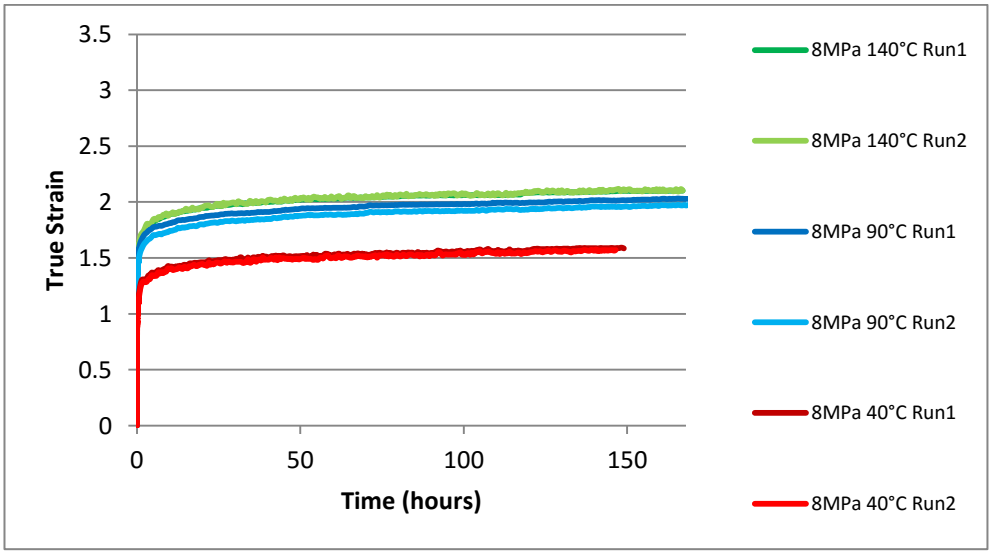

b)

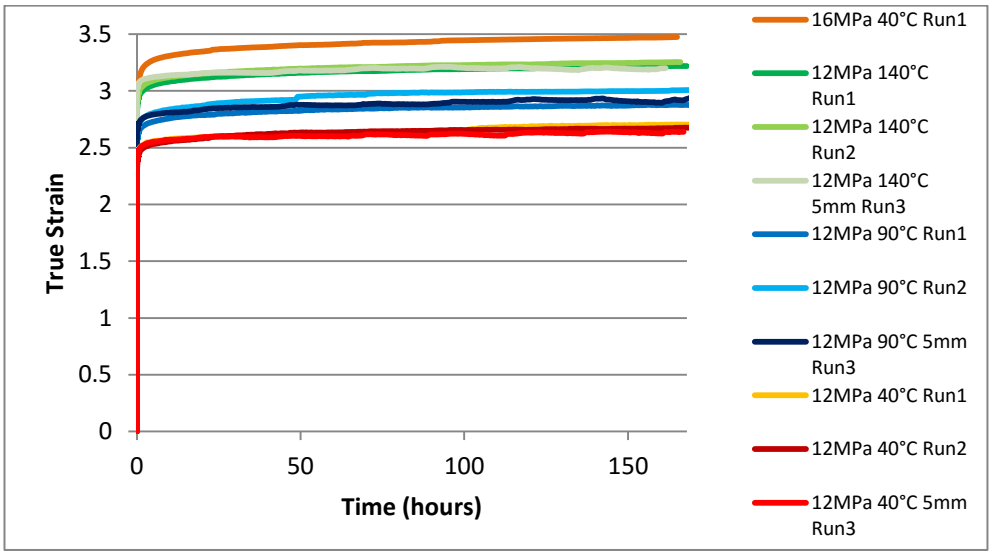

c)

Figure 4.2 True strain observed of the samples over 168 hours at different specific pressures

As presented in Chapter 2- , a Norton creep relationship was to be fitted to the creep data and do this it was determined that two creep strain function should be found, one for primary creep and another for secondary point. This decision was made after initial creep fitting functions were tested on the data, and due to the exponential relationship of the primary creep and linear relationship of the secondary creep, a function was unable to be found which fitted the data to a satisfactory percentage difference error. The definition of secondary creep is when a constant creep rate has been reached. By examining the gradient of the curves, it was determined that at a time of 30 hours, secondary creep had been achieved, as the gradient of each curve no longer changed between time steps. Some cases did achieve secondary creep before this value of 30hours, but this had no effect on the secondary creep rate as the gradient value for each case remains constant in the secondary creep regime. Figure 4.3 shows the amount of change in true strain over time and it can be observed that after the value of 30 hours, no change to the gradient of each test is observed.

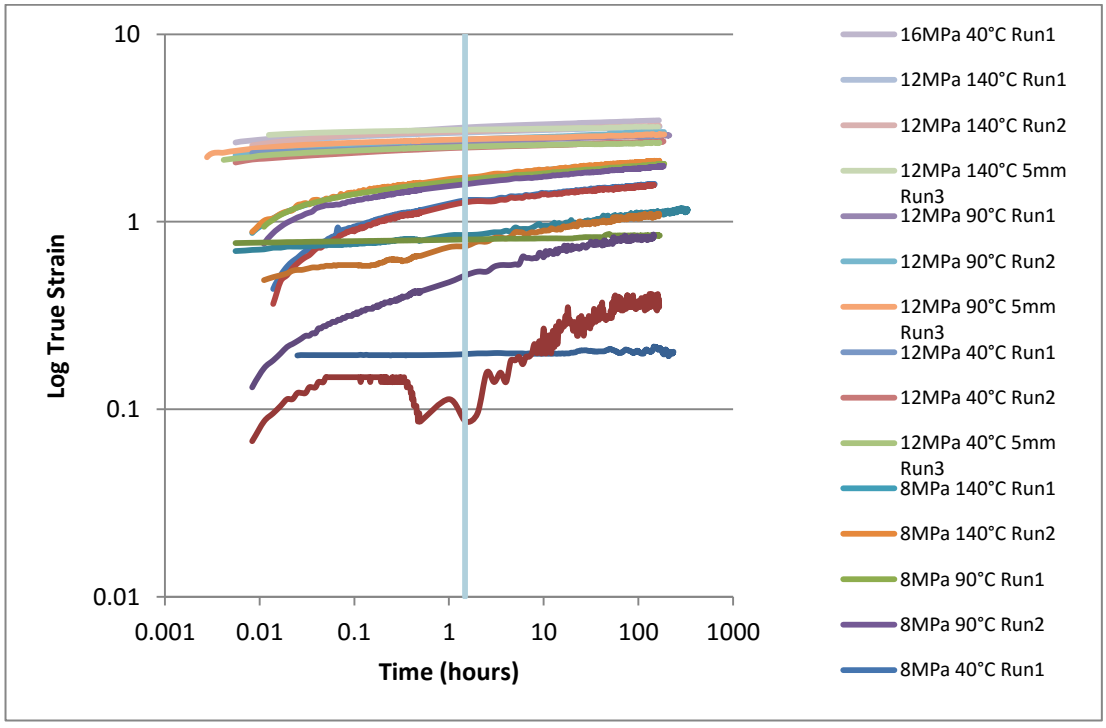

Figure 4.3 Log true strain seen by samples over 168 hours

4.2 Primary Creep Analysis

From Figure 4.2 and Figure 4.3 it can be seen that a large amount of strain occurs during the initial 5 hours of the experiment for all tests, and then starts to tend to a constant rate, i.e. approaching secondary creep. This is in agreement with the literature presented in section 2.2.1. This initial 5 hours of testing tends to follow an inverse function. The amount of strain presents within the results accounts for stain due to elastic deformation as well as plastic deformation due to creep. The rig was not designed to distinguish between different types of deformation, as it only recorded total displacement. The elastic deformation, due to Young's modulus, was assumed to occur within the first few seconds of the experiment, suggesting that the majority of the displacement, and therefore strain, seen within the results Figure 4.1 is due to primary creep and not due to elastic deformation. This is shown by the large amount of deformation present past the initial few readings. From 5 hours to 30 hours, the rate of change of strain decreases until a constant strain rate is achieved, and therefore the secondary creep regime has been reached.

As the aim of this project was to understand the long term effects of creep on PTFE faced thrust pad bearings, for this reason primary creep will not be included within the simulations. This means that between 70% and 90% of the total creep seen by the samples over a 7 day period will be unaccounted for and is therefore one of the limitations of the computational model.

4.3 Secondary Creep Analysis

As stated in earlier in section 4.1, the secondary creep regime was determined to occur from 30 hours, as shown in Figure 4.4. This was when the creep rate was at a constant value, defined as the secondary creep regime in the literature, as discussed in section 2.2.1. With this data range of 30+hours, each test case within Figure 4.4 was fitted

to a linear relationship. The equations of each line was then obtained in the form of equation 4.3, where ε_s equals the total amount of creep, t is time in seconds, $\frac{d\varepsilon}{dt}$ is the secondary creep rate and ε_p is the amount of primary creep present;

$$\varepsilon_s = \frac{d\varepsilon}{dt}t + \varepsilon_p \qquad 4.3$$

Equation 4.3 allows for the prediction of the total amount of creep seen by the sample, at any time point, considering only secondary creep effects. This means that at time=0, the total amount of creep seen within the sample would equal ε_p. This meant that secondary creep was considered to be a linear function, which was supported by published data [43, 44, 48]. This assumption allowed for simulations of secondary creep to be conducted.

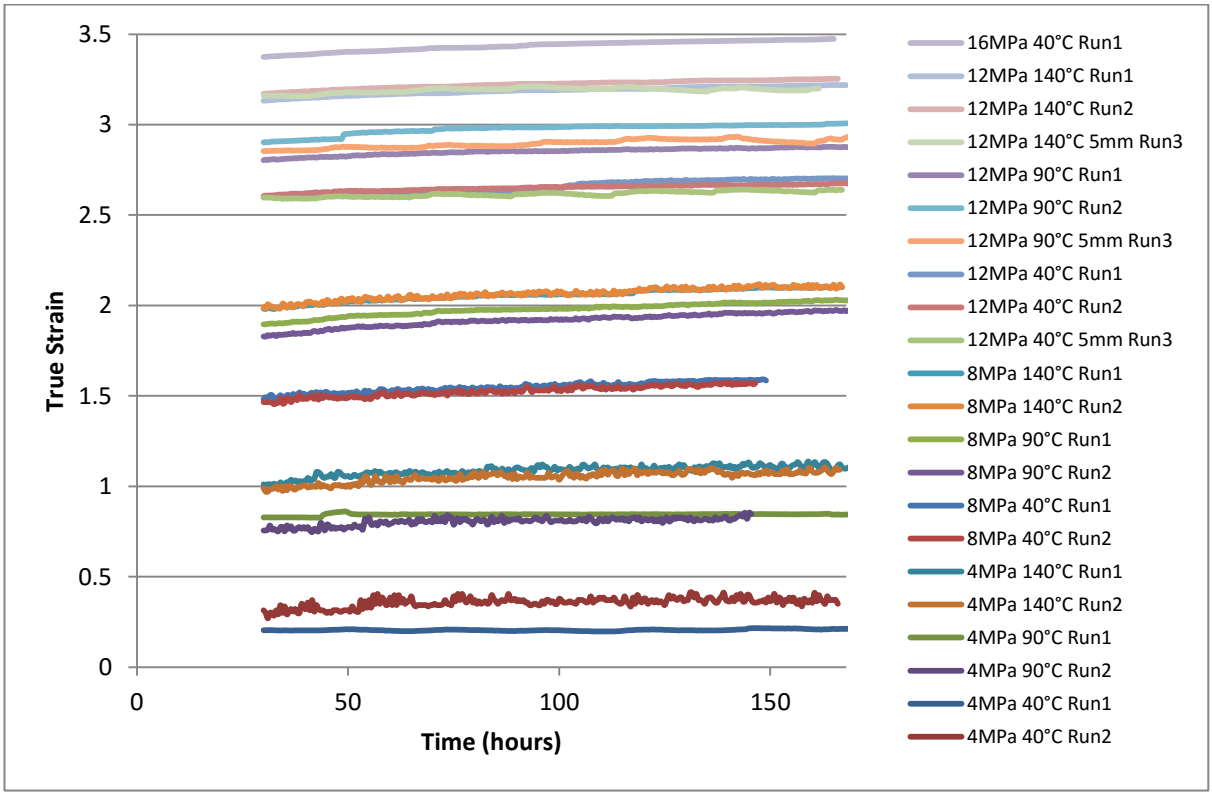

Figure 4.4 True strain seen by samples from 30 hours onwards

The secondary creep rate ($\frac{d\varepsilon}{dt}$) was to be fitted to a Norton Creep function which allowed for the creep rate to be expressed as a function of pressure and temperature.

The $\frac{d\varepsilon}{dt}$ and ε_p for each test case can be seen in Table 4.1 along with the average for each test case. These values were found by using the equation of each line, provided by Microsoft Excel. The average $\frac{d\varepsilon}{dt}$ and ε_p for each test case have been plotted as function of temperature and pressure within Figure 4.5-Figure 4.8. Within these graphs, standard deviation error bars have been added to each graph, though in some cases the standard deviation is so small that the error bars can hardly be seen. These errors bars demonstrate the scatter between the repeat tests at each condition. There was no error bar added to the 16MPa, 40^{O}C case as only 1 test was conducted at these test conditions.

It can be seen from Figure 4.5 that there is a consistent relationship between temperature and strain rate. As temperature increase the strain rate present also increase. This relationship is not present between the steps of 12 and 16MPa. The reason for this lack of relationship is unknown, but as only 1 test was conducted on the 16MPa case, the result will be ignored, for the purpose of finding a creep strain rate function.

Table 4.1 Secondary creep rates and primary creep rates from experimental data

Pressure (MPa)	Temperature (^{o}C)	Run	Secondary Strain Rate	Primary Creep Value	Average Secondary Creep Strain Rate	Average Primary Creep Value
4	40	1	1.56 x10^{-5}	0.21	#	
4	40	2	4.15 x10^{-4}	0.32	2.16 x10^{-4}	0.26
4	90	1	5.02 x10^{-4}	0.76	#	
4	90	2	6.32 x10^{-5}	0.84	2.83 x10^{-4}	0.80
4	140	1	2.80 x10^{-4}	1.05	#	
4	140	2	3.50 x10^{-4}	0.99	3.15 x10^{-4}	1.02
8	40	1	7.09 x10^{-4}	1.48	#	
8	40	2	8.35 x10^{-4}	1.45	7.72 x10^{-4}	1.46
8	90	1	7.95 x10^{-4}	1.90	#	
8	90	2	8.51 x10^{-4}	1.83	8.23 x10^{-4}	1.87
8	140	1	8.10 x10^{-4}	1.98	#	
8	140	2	7.10 x10^{-4}	1.99	8.02 x10^{-4}	1.98
12	40	1	4.92 x10^{-4}	2.57	#	
12	40	2	3.97 x10^{-4}	2.61	#	
12	40	3 (5mm)	3.47 x10^{-4}	2.58	4.12 x10^{-4}	2.59
12	90	1	4.01 x10^{-4}	2.81	#	
12	90	2	5.46 x10^{-4}	2.92	#	
12	90	3 (5mm)	4.30 x10^{-4}	2.85	4.59 x10^{-4}	2.86
12	140	1	5.60 x10^{-4}	3.13	#	
12	140	2	5.45 x10^{-4}	3.17	#	
12	140	3 (5mm)	2.35 x10^{-4}	3.17	4.47 x10^{-4}	3.16
16	40	1	6.97 x10^{-4}	3.37	6.97x10^{-4}	3.37

Considering Figure 4.6, no clear relationship can be drawn between pressure and creep rate. This is due to the sharp increase in creep rate when the 8MPa load case is tested. These tests at 8MPa were repeated twice, and from Table 4.1 it can be seen that no great variation was observed within test cases, the maximum difference being 1.26 x10^{-4}, or 15% of the maximum value.

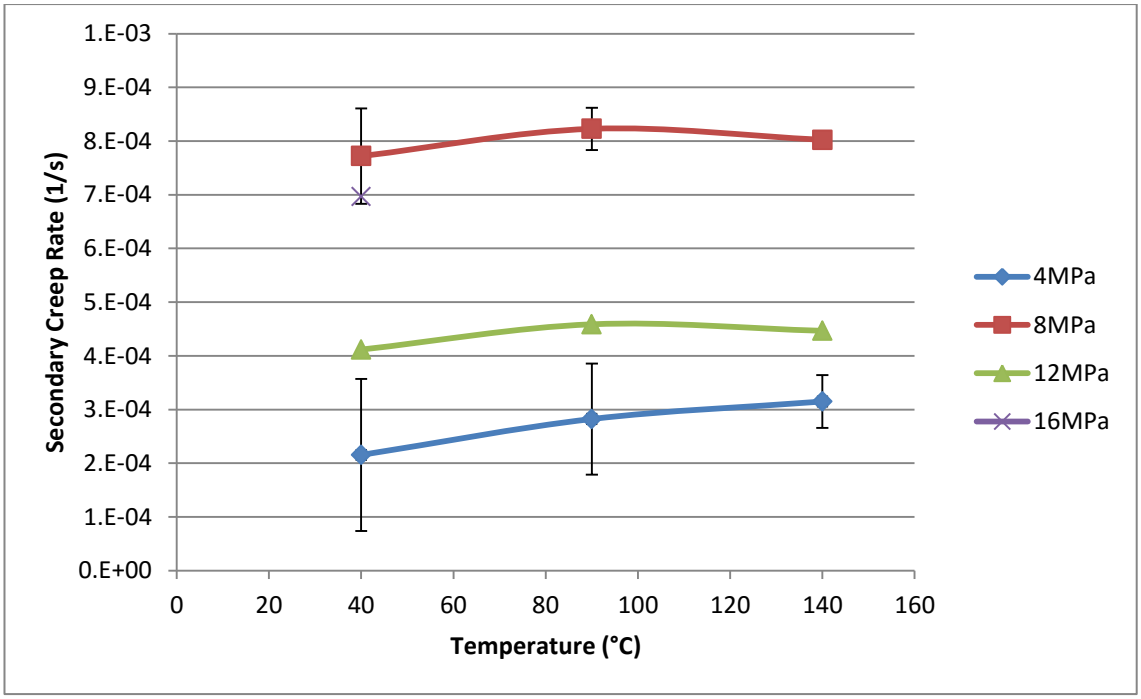

Figure 4.5 Relationship between temperature and secondary creep rate

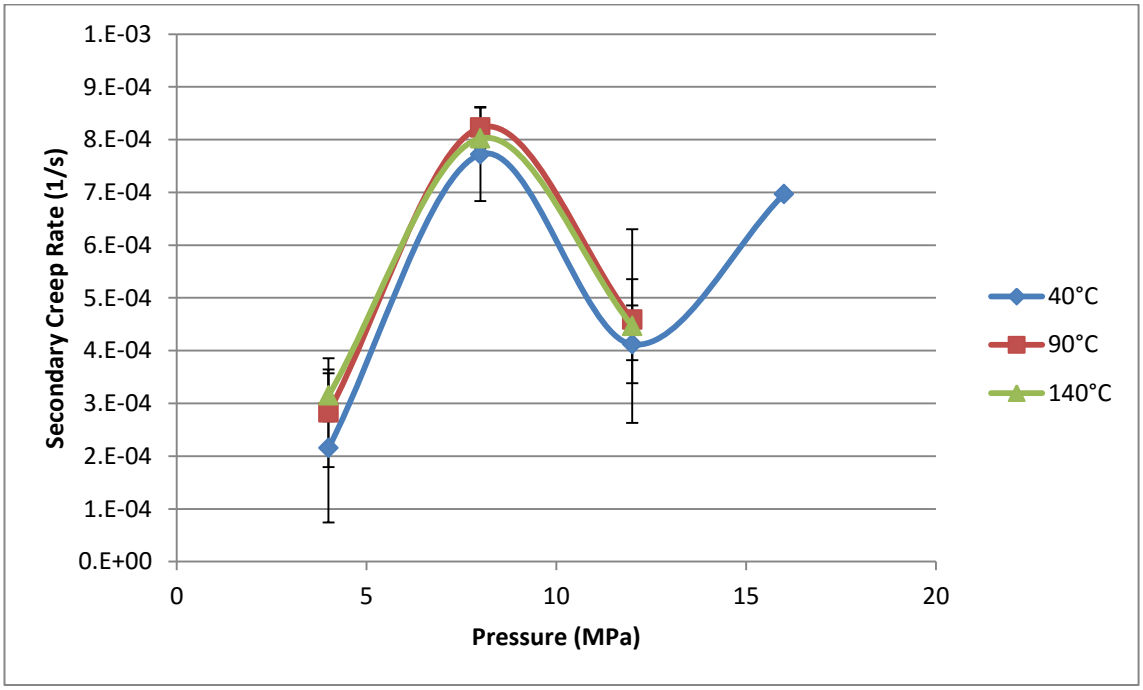

Figure 4.6 Relationship between pressure and secondary creep rate

From these observations it can be concluded that the secondary creep rate is a function of only temperature and not pressure. This means that in any creep function the data is fitted

to, the creep rate should not be a function of pressure. This means, in the case of the Norton, Norton-Bailey or Mukerjee-Bird-Dorn creep law, equations 2.13- 2.15, that the n constant should equal 0, as this would set the pressure term equal to a constant value of unity.

By considering Figure 4.7 and Figure 4.8, conclusions can be drawn about the effect of pressure on temperature on the primary creep. As both temperature and pressure increase the amount of primary creep present at the start of the secondary creep region, which $\boldsymbol{\varepsilon_p}$ demonstrates, increase in a near linear relationship. The gradients of each line would suggest that pressure has a more dramatic effect onε_p, as the increase in ε_p as pressure increases is more significant than the increase due to temperature.

Figure 4.7 and Figure 4.8 show that the primary creep is both a function of temperature and pressure.

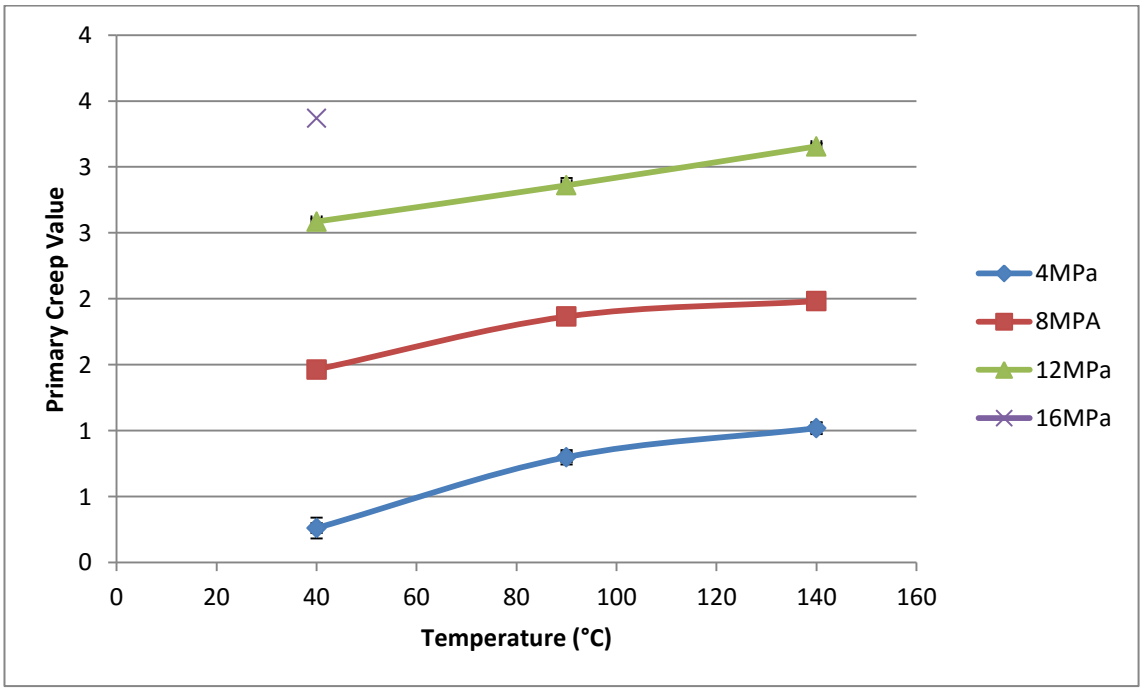

Figure 4.7 Relationship between temperature and primary creep values

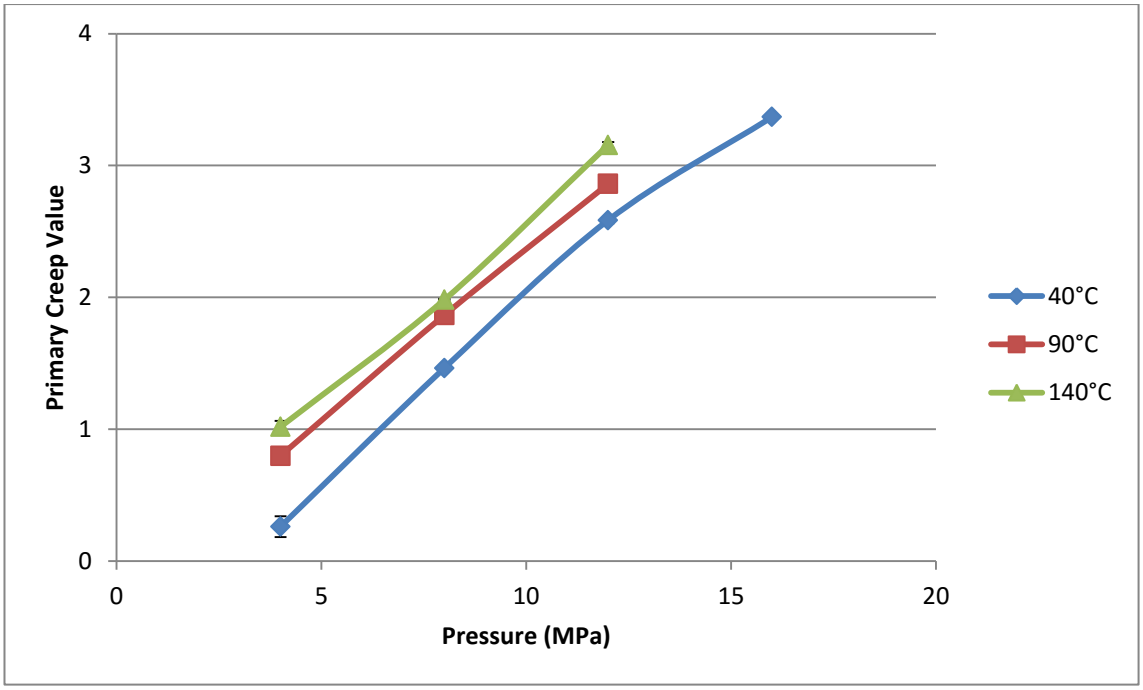

Figure 4.8 Relationship between pressure and primary creep values

From the results gained it can be determined that the full equation for the follows the relationship shown in equation 4.4, in which it can be seen that as temperature changes, the secondary creep and primary creep will change, but if pressure changes, only the primary creep with change;

$$\varepsilon_s = \frac{\partial \varepsilon_s}{\partial t} f(T).t + \varepsilon_p f(T,P) \qquad 4.4$$

This relationship holds true when the condition of time greater than 30hours is maintained.

Using the experimental data for secondary creep strain rates, a regression analysis was performed to allow a creep function to be fitted to the experimental results, as discussed below.

4.4 Creep Fitting Function

Considering the three creep laws put forward from the literature review, a Norton or Norton-Bailey creep law seemed more appropriate to fit the PTFE experimental data to as

the Mukherjee-Bird-Dorm law is better suited to metals. Of these two laws, a time function was not required, as primary and tertiary creep were not being simulated. For this reason a Norton creep function was selected for the creep fitting function.

Assuming the secondary creep follows a Norton creep function, a regression analysis was conducted on the data using Microsoft Excels GRG nonlinear solver. The GRG nonlinear solver works by changing the values of each variable, in this case the values for A and n, until the root mean square (RMS) value is at a global minimum. The RMS values is found by comparing the predicted value for creep rate, with the experimental value for creep rate, for each test case, and then all the errors from the test cases are summed. This solver allowed for the optimum value of *A* to be found, for the Norton creep equation 2.13, with respect to root mean squared (RMS) error. This meant that the value for *A* would vary till the lowest error across all the data was obtained. The effect of allowing *n* to be varied was observed as well, but the optimum value found by the solver tended to 0 every time the RMS was solved. This indicates that the creep rate is virtually independent of stress. The value for *A* found by the regression analysis was 1.601e-17. The final Norton creep function used, with the constants included is shown in equation 4.5. With these values the RMS error was 13.67% and varying these values of A and n only produced a larger error.

$$\frac{d\varepsilon_s}{dt} = 1.60198e^{-17}e^{\frac{-Q}{RT}} \qquad 4.5$$

4.4.1 Alternative Methods to Modelling the Experimental Creep Data

As the experimental creep results were found to be independent of pressure, before a Norton creep law was fitted to the data, other methods to allow for the experimental data to be included within the simulations were considered, which did not rely on a defined creep law. These included a look-up table and an exponential creep model. All of these methods were unsuccessful or inappropriate as discussed below.

A look up table function was included within the software used to simulate the computational model (Comsol Multi Physics). This would allow the experimental data to be included within the model, and the software would extrapolate a secondary creep strain value from experimental data. The software had a limit of two variables that the data could be a function of and the experimental data had three variables (pressure, temperature and time). Using another piece of software to produce a lookup table was investigated, but due to difficulties of then incorporating this new software into Comsol, this idea was abandoned. This meant that a look up table was found to be unfeasible for use with Comsol.

A power creep function was tried as well. This idea was to set the equation of the secondary creep to equation 4.6, and then uses Excel to find the value of the constants (A and n). These constants could be made to include more complexity, by adding more variables, in the form of pressure and time. This idea worked when a variable for temperature was added, but once pressure was added, a solution could not be found within the limits of the optimization solver. The limits of the solver were a RMS of below 20%, which at the time was the accuracy of the Norton creep method.

$$\varepsilon_s = \left(\frac{1}{At - Atn}\right)^{\frac{1}{1+n}} \qquad 4.6$$

4.5 Summary

Experimental creep data has been collected for filled PTFE samples, and a Norton creep function has been fitted to the data allowing for secondary creep to be predicted as a function of temperature. It was found that the filled PTFE did not follow an obvious pattern in terms of pressure, so the n parameter in Norton creep function was set to zero. Whilst this is unusual when compared to other published creep data [44, 45], the overall trend of the experimental creep data is comparable to published results. Other methods to fit the

experimental data were tried, but the Norton creep function was deemed to be most appropriate when PTFE secondary compressive creep was considered and when simulated within Comsol Multi-physics software.

Chapter 5- Computational Methodology

The following chapter describes the thermal elastro- hydrodynamic lubrication (TEHL) model used by the author to predict the effect of creep on the life span of a thrust pad bearing. The traditional Reynold's lubrication theory for EHL is introduced along with the governing equations of the fluid, mechanical material properties, thermal effects and visco-plastic creep effects. A review of numerical techniques is given along with a description of the finite element method (FEM) and the equations associated with FEM.

Figure 5.1 demonstrates the interaction between the different parts/ equations of the model, and how the equations are coupled.

The Reynolds equation [11] is used to predict the pressure seen by the pad in the lubrication film. This pressure is found by considering the fluid film thickness, among other constants, which in turn is effected by deformation caused by the pressure acting on the pad, as described by Hertzian contact theory [53]. Dowson and Higginson first used this idea to solve the coupled equations [10] and the method is referred to as elasto-hydrodynamic lubrication (EHL) theory. The energy equation is then solved in the fluid film, with heat generation occurring due to the pressurised fluid passing over the pad surface. This change in temperature is conducted through the pad, changing the material properties of the fluid and pad, along with causing the pad to thermally expand [54]. With the temperature and pressure the pad is subject to now known, visco-elastic secondary creep effects was simulated within the model so a further understanding of secondary creep effects, using a Norton creep function can be made.

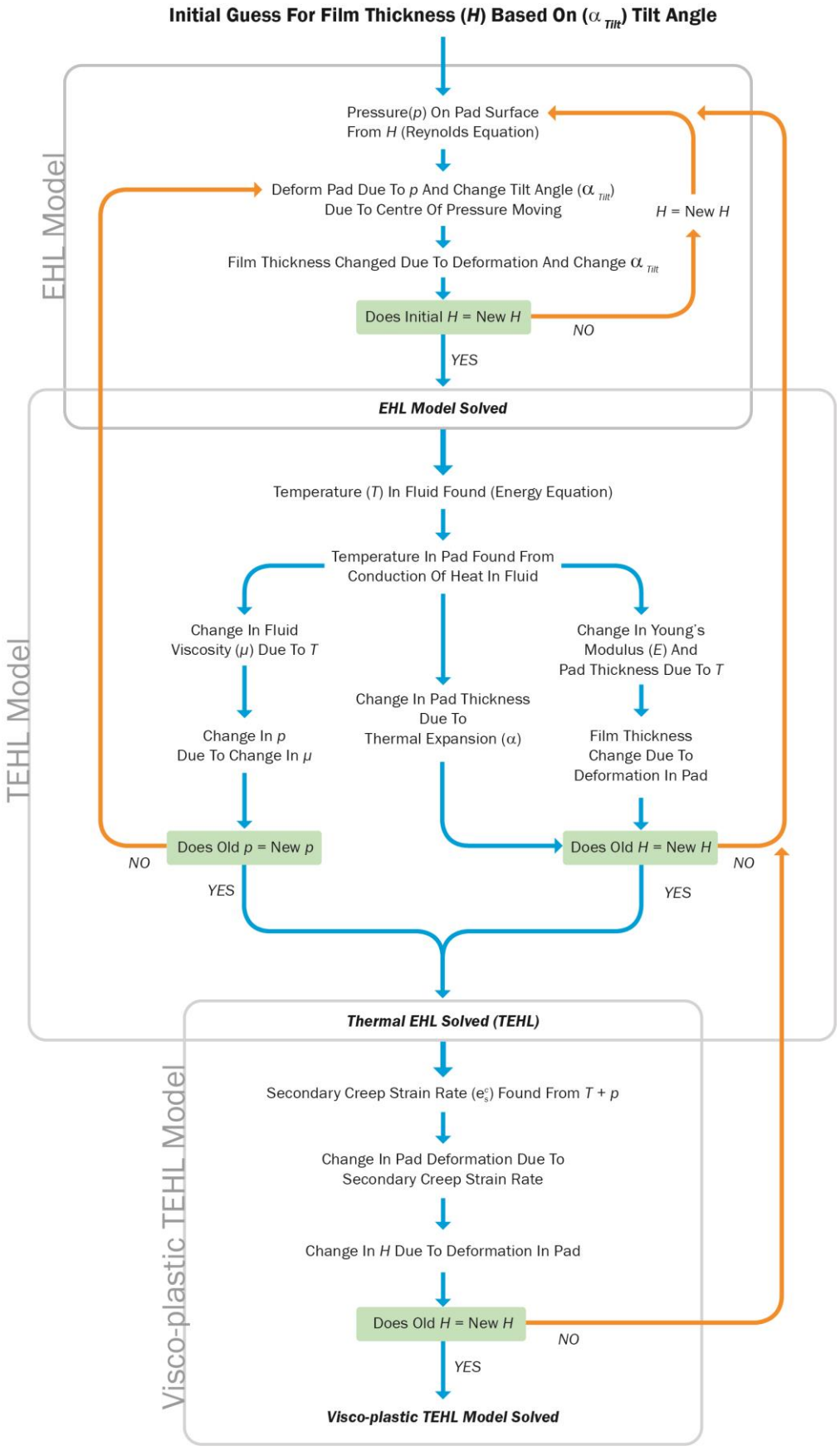

Figure 5.1 Final model flow chart

Once the model has been described and an understanding of numerical methods and FEM is provided, the chapter describes the validation checks on the model, and the final pad size and parameters used in the visco plastic creep study.

5.1 Thermal Elasto- Hydrodynamic Lubrication Model

The following section of the chapter describes the equations used within the computational model to predict the pressure and temperature within a thrust bearing pad system. This system considers a thrust bearing pad, at a tilt angle, separated from the collar thrust by a thin film of oil. The section describes the deviation of each equation in a general form, before applying them to a thrust bearing case.

5.1.1 Reynolds Equations

The Reynolds equation, derived by Reynolds in 1886 [11], describes the pressure in the lubricated film, and was derived from the Navier-Stokes equations by following the assumptions listed below[54] (a full deviation of the Reynolds equations is shown in Chapter 2-):

- Pressure is constant through the fluid film
- Body forces are negligible
- The fluid film is a Newtonian fluid
- The fluid viscosity is constant across the film
- The fluid film boundary surfaces are parallel or at a small angle in two dimensions
- No slip boundary at the fluid- surface interaction
- Fluid flow is in the laminar regime
- Inertia and surface tension forces are negligible compared with the viscous forces
- Shear stress and velocity gradients are only significant across the fluid film

$$0 = -\frac{\partial p}{\partial x}\left(\frac{\rho H^3}{12\mu} + \frac{UH}{2}\right) - \frac{\partial p}{\partial y}\left(\frac{\rho H^3}{12\mu} + \frac{VH}{2}\right) \quad 5.1$$

By considering steady flow, the equations can be reduced further to equation 5.1. Dowson introduced a generalised form of the Reynolds equation which allowed for the variation in fluid properties across the fluid film to be account for along with solving the energy equation within the fluid film[13]. Using equation 5.1, the pressure generated by the fluid passing over a thrust bearing pads surface can be predicted by considering the varying fluid film thickness. This allowed for deformations of the pad surface, due to the fluid pressure, to be solved for.

5.1.2 Fluid Film Thickness equations

As the pressure generated by the fluids can be in the order of 10MPa, the surface in contact with the fluid can be deformed. The film thickness (*h*), in the case of this project, is the local distance between the collar and the pad. The deflection of the pad is assumed to be elastic and the forces seen by the pad does not exceed the yield point of the material, shown in Figure 5.2.

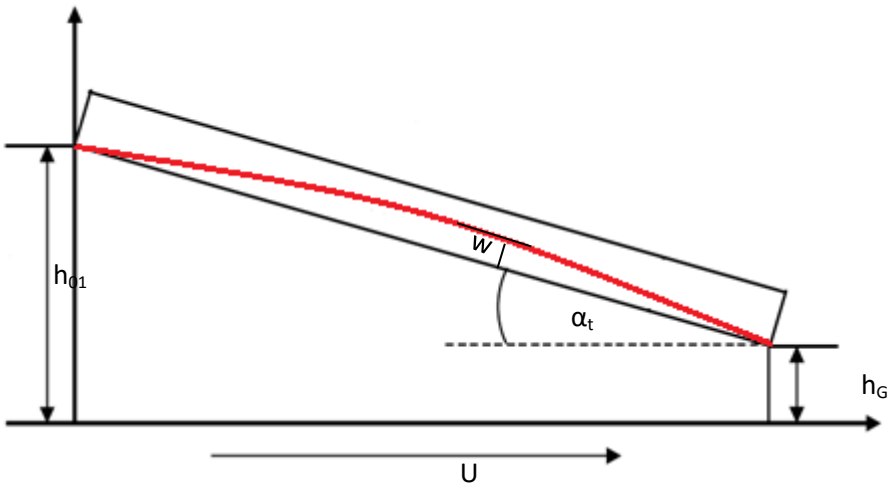

Figure 5.2 Fluid film shape

Within Figure 5.2, h_{01} is the undeformed film thickness, α_t is the angle of tilt of the pad, U is the direction of rotation, h_G is the film thickness between the lowest point of the

pad and the collar, also known as the gap thickness and W is the deformation within the pad due to pressure within the fluid. By considering Figure 5.2 the film thickness within the fluid can be predicted as shown in equation 5.2, which is a function of tilt angle of the pad, the gap between a pad and the counter surface (collar), original film thickness and elastic deformation on the pad surface due to pressurised fluid film.

$$H = h_{01} + h_G + \alpha \cdot x + W \tag{5.2}$$

5.1.3 Energy Equation

Due to the fluid being a pressure driven flow, it was concluded by Ettles [55] that thermal effects should be account for as within the fluid film for a thrust bearing. Dowson [10] first put for a method for solving the energy equation in the fluid film, when an EHL contact system was considered. The derivation of the energy equation made the following assumptions and resulted in equation 5.3 [54], where *T* is the temperature, *α* is the thermal expansion of the surface, *K* is the thermal conductivity and C_p is the specific heat at constant pressure of the fluid.

- Velocity across the film is negligible
- Thermal conductivity is constant within the fluid film
- Velocity and temperature gradients are only significant across the fluid film and are negligible in the direction of flow

$$\alpha UT\frac{\partial p}{\partial x} + K\frac{\partial^2 T}{\partial z^2} + \mu\left(\frac{\partial U}{\partial z}\right)^2 = \rho C_p U\frac{\partial T}{\partial x} \tag{5.3}$$

The thermal expansion component of the energy equation is considered at a later point with in this chapter, so is neglected for the moment. Considering the energy equation in 2-directions, the x, y direction, and the full equation becomes;

The energy equation was discussed in chapter 2.1.5 and shown in equation 2.11.

Using the velocity of the fluid in each direction, *U, V* and *W*, and their respective gradients in the x, y and z direction, the heat generation within the fluid could be found, which in turn courses a change in the temperature within the pad. It should be noted that the velocities and their gradients are a function of pressure.

5.1.4 Thermal Expansion

As materials experience a change in temperature, the material thickness can increase or decrease, depending on which direction the temperature changes. As the temperature of a material increase the thickness will increase. This is due to internal thermal strains, caused by the changed in temperature. This effect is called thermal expansion. The thermal expansion effect is defined by equation 5.4, where ε_{TE} is the strain due to thermal expansion, *T* is the current temperature, T_0 is the reference temperature set to 25^{O}C, and α is the coefficient thermal expansion.

$$\varepsilon_{TE} = \alpha(T - T_0) \qquad 5.4$$

By applying equation 5.4 to the pad surface allowed for the deformation due to thermal expansion to be included within the film thickness equation.

5.1.5 Thermal Mechanical Properties

After consulting literature, it was deduced that the Young's Modulus of the PTFE would vary with temperature [45, 56], a relationship between Young's modulus and temperature could be obtained, shown in equation 5.5, where *E* is the Young's modulus, in Pa, and *T* is the temperature in ^{O}C.

$$E = 7x10^{8}e^{-0.0012T} \qquad 5.5$$

By comparing values for Youngs modulus at 25^{O}C for the filled and unfilled PTFE, a relationship was found for effect of temperature on filled PTFE Young's modulus, shown in

equation 5.6. As stated within Chapter 2, the filled PTFE considered within the study was 15% Black carbon, 2% Graphite blend of PTFE.

$$E = 4x10^{8}e^{-0.0012T} \quad 5.6$$

The temperature would also affect the oil properties. From [57] viscosity data, it was observed that for a temperature of 0-400^{O}C, the viscosity of the oil decreased at a non-linearly rate. From experimental data, an algebraic relationship was obtained to allow for the predictions of viscosity to be made at any temperature. This relationship is shown in equation 5.7, and is the gradient of the line from the experimental literature data [57].

$$\mu = 0.0027T^{2} - 0.6524T + 42.523 \quad 5.7$$

5.2 Numerical Solving Methods

To solve complex equations numerically, like EHL problem, a method had to be developed. A numerical method called finite element analysis (FEM) was developed, initially to solve solid mechanics problems before being used to solve large problems such as EHL theory. The theory allows for mutually dependent variables (such as pressure being dependent on film thickness, and vice versa) to be solved for across a described physical domain, with the aim to reduce the error within the problem to a minimum.

The theory finds an approximant solution to the problem by splitting a domain up into much smaller sections, also called elements. The points were elements connect are called boundary's, and where boundary's intercept are called nodes. This process of splitting a domain up into smaller domains, or elements, is called discretization, or meshing. Each domain of the shape is viewed as a finite number of nonintersecting simple sub domains, or elements, leading to the name finite element. These finite number of elements are then combined, once a solution has been found so that, to remake the initial domain, allowing the solution across the original domain to be observed. This method of

splitting a domain into smaller elements reduces the approximant error of the solution when compared to using a single large element.

FEM allows for multi-physic problems, like a TEHL thrust bearing model, to be coupled and partly coupled together. This means that, using the TEHL thrust bearing as an example, the pressure and film thickness equations, which are depend on each other, can be solved for and iterated to an approximant solution is found, whilst these variables are also being used to solve the energy equation.

The FEM based model used for this work needed several conditions to be defined to be able to solve the TEHL model. The following sections describe these conditions such as domain types, boundary conditions and mesh selection. For the boundary condition section, each separate boundary condition is discussed independently. Boundary conditions are used to describe boundaries between domains, at a PTFE-oil interface for example, as well as effects at the edges of a boundary, where data or values are not known or solved for.

5.2.1 Domains within Model

The model was defined to have 3 domains, a steel domain which was connected to a PTFE domain, which in turn was connected to a fluid domain. This is shown in Figure 5.3, along with the shape of the pad. Fillets and chamfers were not included within the model, as previously stated.

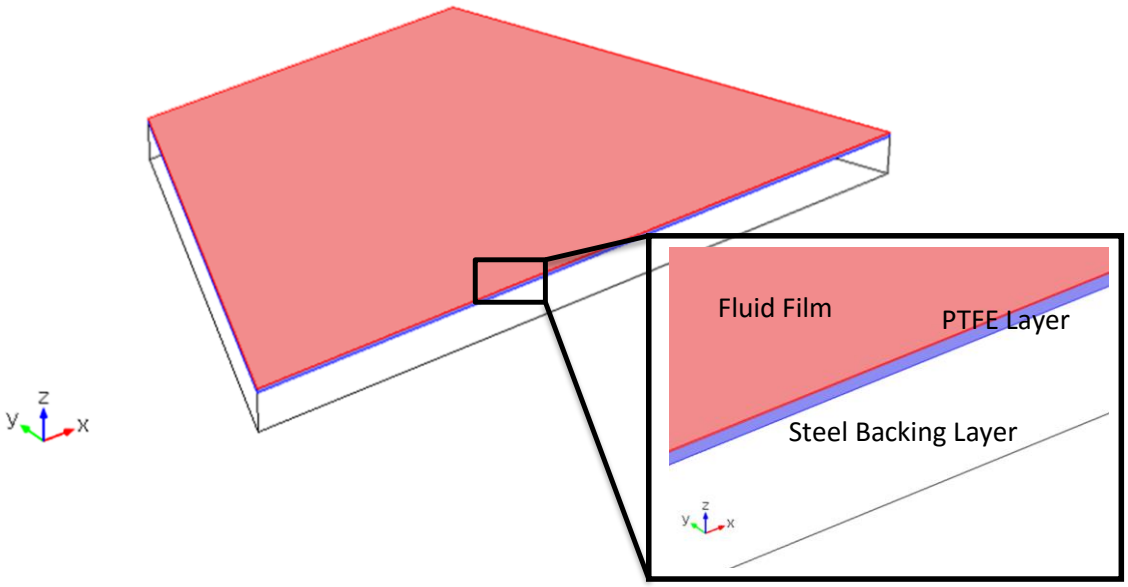

Figure 5.3 A diagram showing the location of the 3 different domains considered within the visco-plastic study

Within the steel domain, only the energy equation was solved for. This meant that heat could be transferred into the domain, but it would not deform due to pressure from the PTFE pad surface. This is a reasonable assumption for this relatively high modulus material[55, 58].

The energy equation was also solved within the PTFE domain, with heat being transferred from the fluid domain to the PTFE and then onto the steel domain. Along with thermal effects, visco-plastic secondary creep effects were accounted for within the PTFE domain (discussed later in section 5.4), as well as temperature dependent expansion deformation, deformation due to pressure of the fluid film and thermal changes to the Young's modulus of the material, as shown in equation 5.6.

Within the fluid domain, the energy equation was solved, with the viscous heat generation term being included, as well as the pressure within the fluid being found fromReynolds equation. The fluid film was adjusted to account for tilt angle, which changed as a function of centre of pressure and deformation of the pad surface due to the

pressure, due to visco-plastic effects and due to thermal expansion. The viscosity of the fluid also changed as a function of temperature as shown in equation 5.7.

Boundary conditions for each domain are discussed in sections 5.2.3-5.2.5.

The process followed by the solver to find a solution is described below, and also shown in Figure 5.1. The model started with an undeformed PTFE surface, and the fluid film was initially deformed by the tilt angle only. The FEM solver was configured into 3 parts. The first part was a stationary solver used to find initial conditions for the model. Within this step, only pressure on the pad surface and film thickness, as a function of tilt angle of deformation due to pressure, were calculated. This meant that only the PTFE and fluid domains were active, as the steel domain was considered to be rigid. The second step of the solver was also a stationary (time independent) solver, in which a solution for everything apart from visco-plastic creep effects was found. In this step all three domains were active. The final solver step was a time dependent solver in which visco-plastic effects were included, along with all of the above mentioned equations and physics. As with step two, all three domains were active within this step.

5.2.2 Mesh Selection

A mesh study was conducted to allow for the lowest solving time to be obtained, whilst being at such a mesh density that the solution would not change dramatically increasing or decreasing the number of elements within the mesh. It was decided that maximum temperature would be the variable to be compared between mesh cases, so that it could be seen how much change occurred between changes in number of mesh elements. During testing it was observed that a mesh of 7200 elements or above would not solve due to computing power. The results from the mesh study are contained in Table 5.1 and displayed in graph form in Figure 5.4.

Table 5.1 Mesh sensitivity study results

Mesh Size	Peak Temperature (°C)	Percentage Difference
1800	125.687	#
2400	105.942	15.710
3300	91.103	14.007
4400	76.489	16.041
4620	72.557	5.141
5324	72.099	0.631
5500	71.81	0.401
6878	71.494	0.440

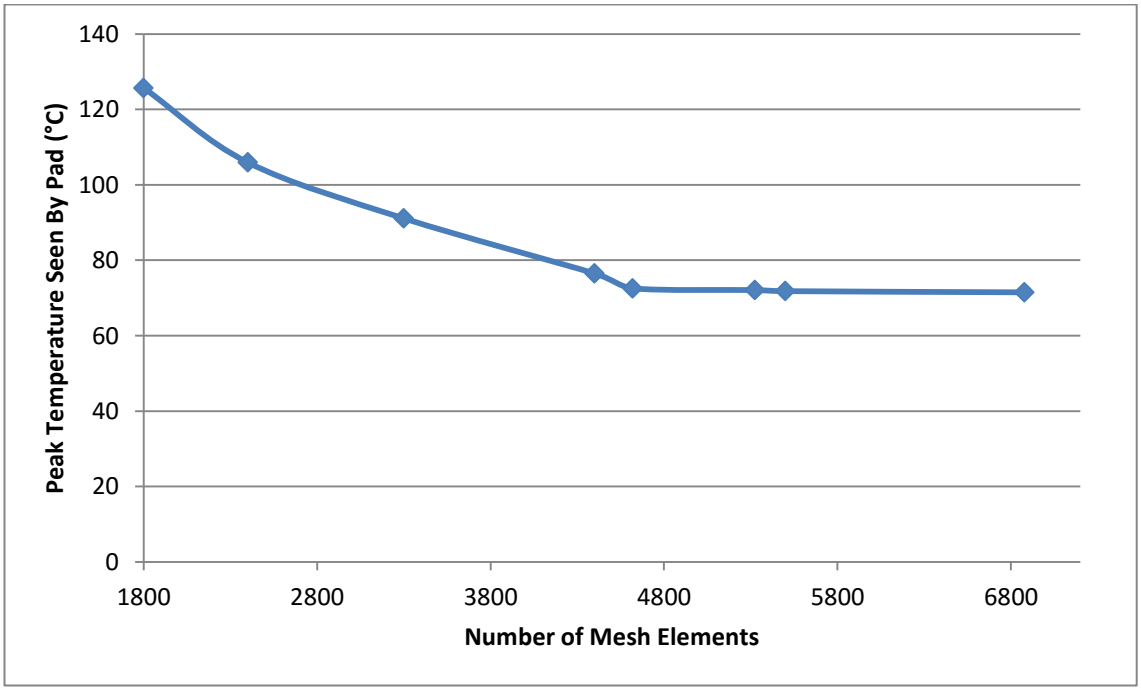

Figure 5.4Mesh sensitivity study

From these results, a mesh of 5324 elements was selected, which consisted of 22 elements in the X and Y direction, 2 elements thick in the steel domain, 4 elements thick in the PTFE domain and 5 elements thick in the fluid domain. As before, the mesh in the X and Y direction was weighted so that more elements would be at the trailing outer edge as anywhere else. This was to allow for more elements to be at the point of peak pressure, where the maximum amount of deflection would occur. The final selected mesh is shown in Figure 5.5.

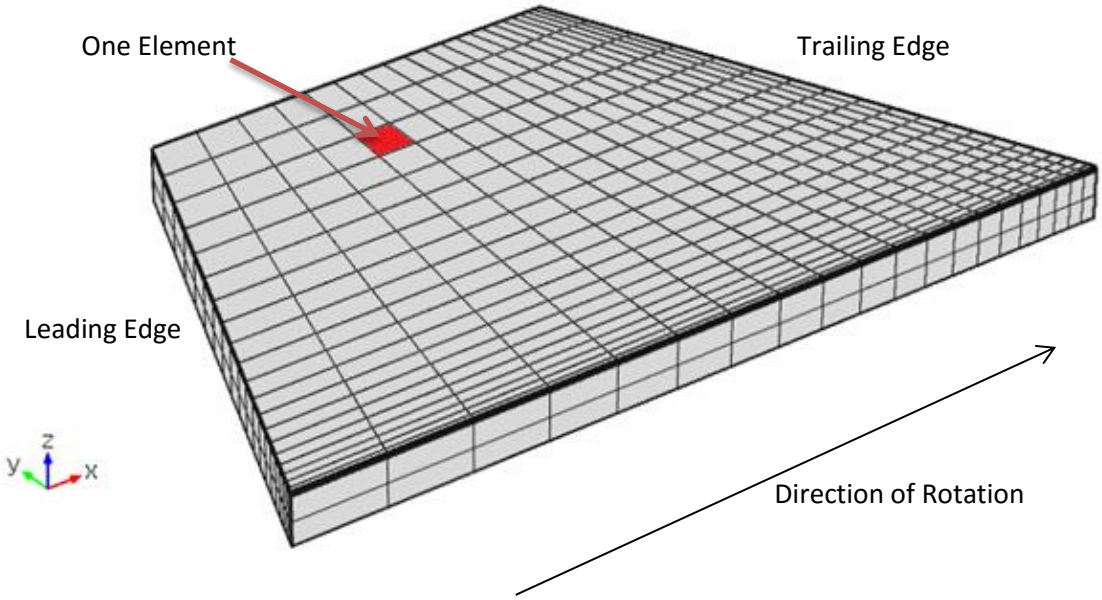

Figure 5.5 Final mesh of 5324 elements

5.2.3 Pressure Boundary Conditions

Figure 5.6 dictates the location of the boundaries used within the proposed model, on the PTFE domain, where boundary 1 is the PTFE fluid interface, 2 is the PTFE steel backing interface and 3 and 6 are the leading and trailing edges respectably and 4 and 5 are the outer and inner radius of the pad.

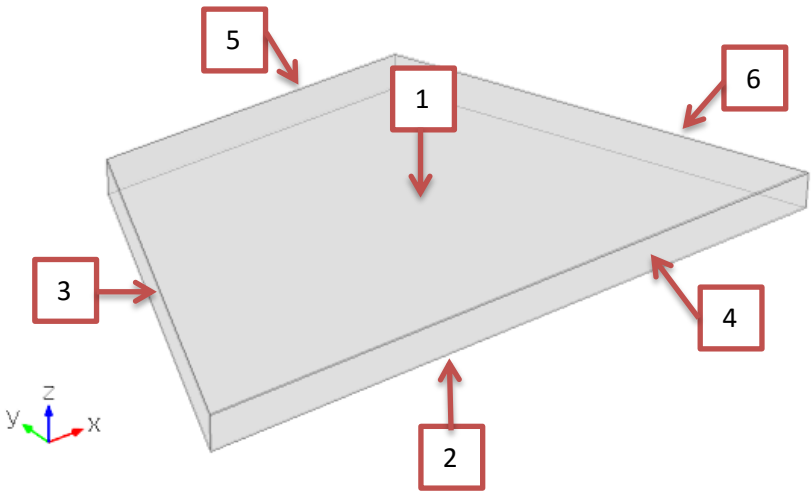

Figure 5.6 PTFE domain with boundary's labelled

The boundary conditions applied to the EHL model are as follows;

Table 5.2 Boundary conditions for EHL model

Boundary 1,	**Load= p(x,y)**
Boundary 3,4,5,6	$\delta_{x,y}$=0
Boundary 2	$\delta_{x,y,z}$=0

These boundary conations mean that the lower boundary of the PTFE, which in a real system would be connected to a steel backing plate, does not deform in any direction. The edge boundary only deforms in the z-direction, and are restricted in the x and y direction. The Top PTFE boundary, the oil-PTFE interface boundary, is free to deform in any direction, as a function of pressure within the fluid film.

5.2.4 Hot Oil Carry Over Effect

In a practical thrust bearing system, fresh oil would be supplied into the systems from injectors, placed between each pad. The oil currently in the bearing blocks systems would be at a higher temperature then this new oil supply temperature due to the viscous heat generation caused by passing over the pad surface. This new supplied oil mixes with the oil already in the systems and would change the overall oil temperature seen by the pad, i.e. the temperature would not be equal to the exit temperature of the previous pad or the oil supply temperature. Setting an overall temperature of the oil entering the system to be equal the supply oil temperature would be incorrect as it does not account for the carryover. Ettles [23] proposed an inlet condition for the oil entering a pad to account fot this hot oil carry over effect, shown in equation 5.8, that predicts the inlet temperature of a pad by considering the oil supply temperature (T_s), the outlet temperature (T_o) and a hot oil carry over coefficient (k) to find the new inlet temperature for the pad.

$$T = T_s\left(\frac{1-k}{1-\frac{1}{2}k}\right) + T_o\left(\frac{\frac{1}{2}k}{1-\frac{1}{2}k}\right) \qquad 5.8$$

Ettles concluded that the inlet temperature should be based on a ratio of outlet temperature and inlet temperature, as seen in equation 5.8 and the weighting of this ratio should be determined by velocity of the fluid. This was because the fresh oil entering the system always entered at a constant rate whilst the oil exiting the previous pad would vary with speed. Ettles observed that the faster the mean velocity of the fluid, the more dependent the ratio was on the outlet temperature, meaning a higher inlet temperature for the new oil. Using data from Ettles paper [23], an equation for k, shown in equation 5.9, was obtained which allowed for the prediction of *k* as a function of mean velocity within the fluid domain (V_m).

$$k = 1x10^5 \cdot \left(V_m{}^2\right) - 0.0057 \cdot V_m + 0.8863 \qquad 5.9$$

As the oil left a pad, and mixed with the fresh supply oil, the thermal energy of the fluid within the space between pads would spread out over the entire domain. For this reason an average was taken of the outlet temperature and used within the hot oil carry over equations, so that the inlet temperature of the pad had a single value i.e. it did not vary along the boundary.

5.2.5 Thermal Boundary Conditions

With an average value for hot oil carry over found, the boundary condition of the following could be used on the inlet oil edge boundary;

$$\frac{\partial T}{\partial z} = 0, \quad \mathrm{T} = \text{Average hot oil carry over value}$$

This boundary condition constricts the temperature variation in the Z direction. This is safe to assume, as an assumption of Reynolds equation is that no variation in the z direction of pressure occurs, and temperature is a pressure dependent value.

The top and bottom boundaries, i.e. the oil-collar boundary and the bottom steel boundary were set to thermal insulators, i.e. $\frac{\partial T}{\partial x,y,z} = 0$.

The remaining edge boundaries, of the PTFE domain and steel domains, were set to a constant temperature equal to the fresh supply oil temperature.

On the interior boundaries, i.e. between the oil and PTFE domains and the PTFE and steel domains, a conjugate heat conditions was set. This meant that the temperature at each domain boundary was equal either side of the boundary, allowing for heat to transfer freely between the domains (no thermal resistance at interfaces).

5.3 Validation of Model

Using the equations described above, a TEHL model was created by the author implemented in Comsol Multi-Physics software. The model consisted of a three domain model, an oil film domain, which was contacted to a PTFE domain, which in turn was connected to a steel domain. The steel domain did not consider the EHL equations, only thermal conduction was considered within this domain. All domains were considered to have the same surface area, with only the thickness of each domain varying.

This model used the Dowson-Higginson [10] EHL theory to predict the pressure caused by the fluid film passing over a tilted pad, as a function of film thickness. This pressurised fluid caused a deflection within the pad and altered the film thickness accordingly. The velocity of the pressurised fluid, in the x and y direction, was considered, along with the velocity gradients, and was used to predicted the heat generation within the fluid film. This temperature change of the system was then considered using conduction heat laws. With a change in temperature present, the model also considered changes in the Youngs modulus of the PTFE and the viscosity of the oil. The model also considered the

effect thermal expansion had on the film thickness and therefore the pressure within the fluid.

With a TEHL model, two validation studies were conducted on the model to check the models accuracy. The first study considered was on published results put forward by Ettles [2], in which a constant temperature model was considered. The second study was conducted on industrial test data. This data was provided by the project Industrial sponsors, Michell Bearings of Rolls Royce [59]. Within both models, creep effects were not included at this point in the project as it was thought unlikely that the effects would have a significant effect on the temperature.

5.3.1 Comparison with Published Results

Using published data [2], the pad bearing were defined to the dimensions given in Table 5.3, and the model made as accurate to the data as possible. The study considered a steel line pivot Babbitt metal thrust pad bearing. Therefore different material properties had to be set within the simulation to simulate Babbitt metal and not PTFE. Apart from these changes, no other changes were made to the model. Also within the published results, peak pressure values were not provided, only pressure profiles. This meant that comparing the pressures would be an inaccurate method of validation. Therefore only film thicknesses were comparable between the model predictions and the published results.

Table 5.3 Published result's pad sizing

Outer Length (m) (Ro)	0.41
Inner Length (m) (Ri)	0.79
Number of Pads	8
Pivot Type	Lined Pivot
Pivot Position (%)	60

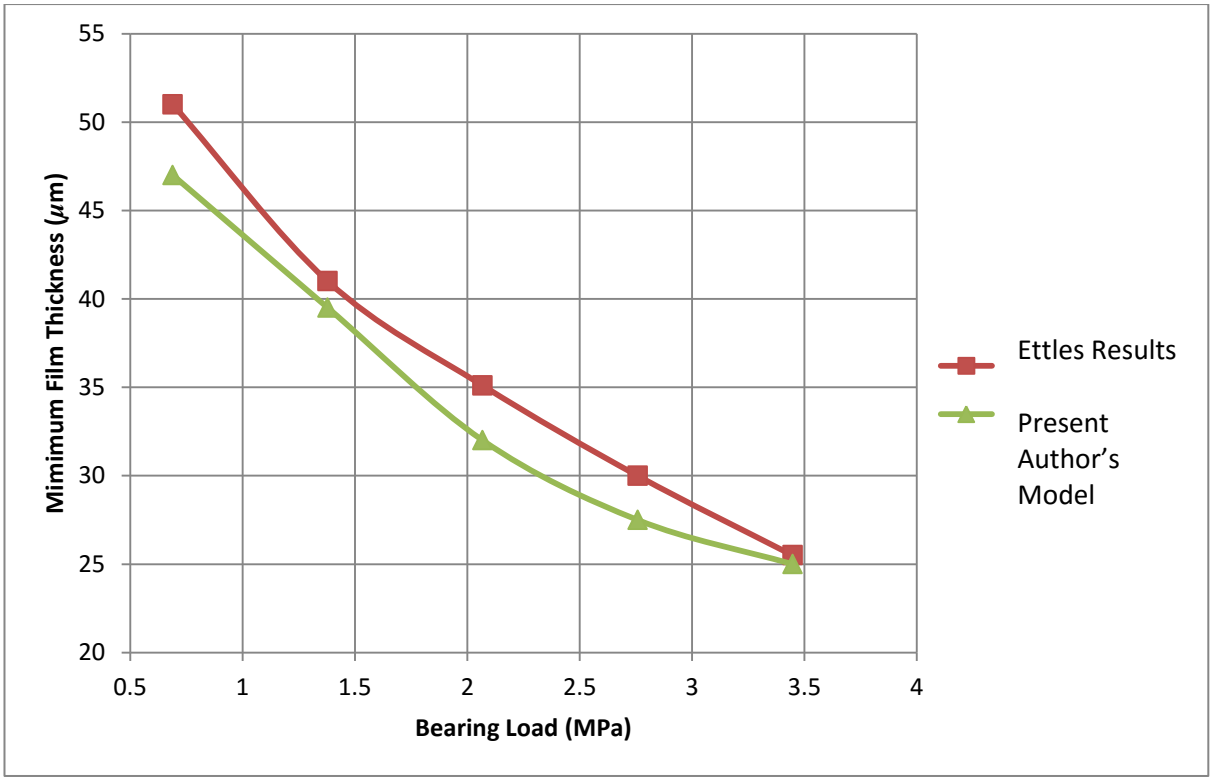

Figure 5.7 Comparison of film thickness predicted by model with published results

A comparison between the results of the present author's model and Ettles model can be seen Figure 5.7.It can be seen from Figure 5.7 that the model predicts minimum film thickness to be close to the published works, with percentage difference between 1.97% at 3.4MPa, and 10.11% at 2.1MPa. These values are the minimum and maximum for the percentage difference between the two sets of results. It was concluded by the author that this percentage difference between the results, and the trend agreement, was within significant agreement to count the model as accurate for a stable temperature condition.

5.3.2 Comparison with Industrial Test Data

The industrial test data provided by Michell Bearings, in private communications with the author, contained experimental test results for a range of specific pressure and rotational speed, at all combinations of these variables. These test conditions are shown in Table 5.4.

Table 5.4 Michell bearings report test conditions

Specific Pressure (MPa)	Rotational Speed (revs/min)
2.88	400
4.33	600
5.76	800
	1200

The bearing described within the report considered a small bearing, as seen from dimensions of the thrust pad shown in Table 5.5.

Table 5.5 Michell bearing pad dimensions

Outer Length (mm) (*Ro*)	179
Inner Length (mm) (*Ri*)	89
Number of Pads	8
Sector Pad Angle (^{o})	40
Thickness of Steel (mm)	10
Thickness of PTFE (mm)	1
Pivot Position (%)	60

The results presented within the report were of eight thermocouples placed around the pad, at different locations and heights within the pad. Thermocouples 1-7 were located at the PTFE-steel interface 1mm below the PTFE surface and thermocouple 8 was located at 0.1mm below the PTFE surface. The locations of theses thermocouples are shown in Figure 5.8.

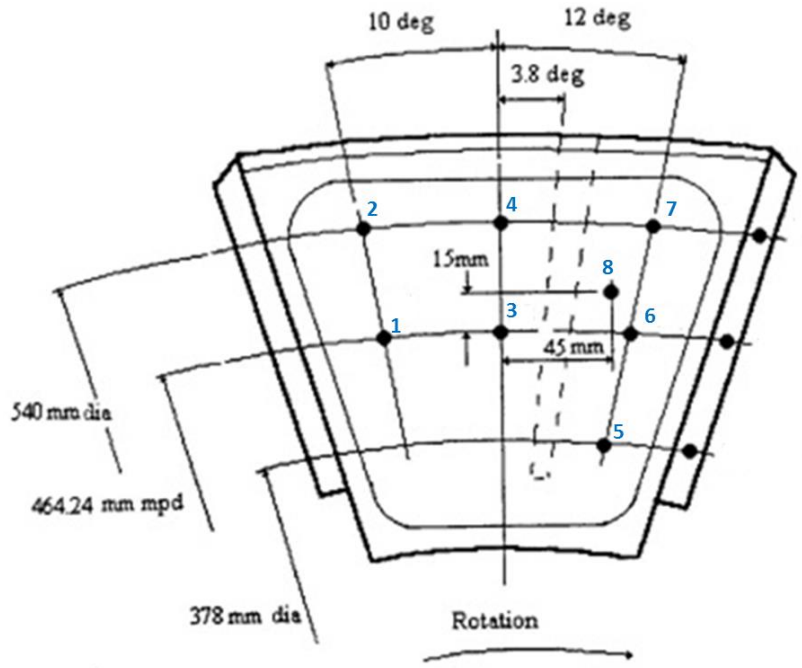

Figure 5.8 Location of thermal couples on pad for inlet temperature study

Figure 5.9 shows the layout of the pad configuration used by the computational study. Within the study, as each pad was assumed to be axisymmetric, only one pad was simulated.

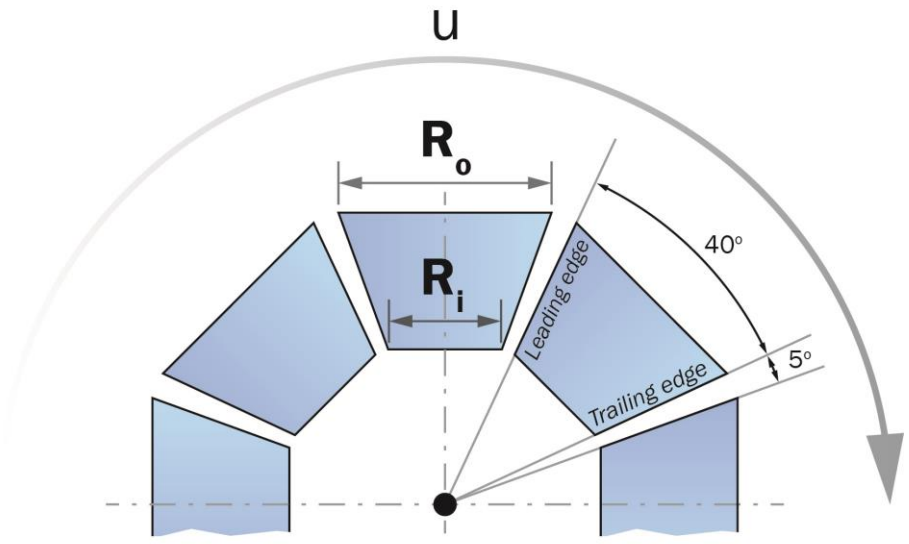

Figure 5.9 Layout of a pad used within the computational model

Using the results from the experimental study, temperatures from each thermocouple were plotted against predicted temperature at these locations, produced by

the model developed in this work. A range of specific pressure and rotational speeds were compared and these results can be seen in Figure 5.10Figure 5.12.

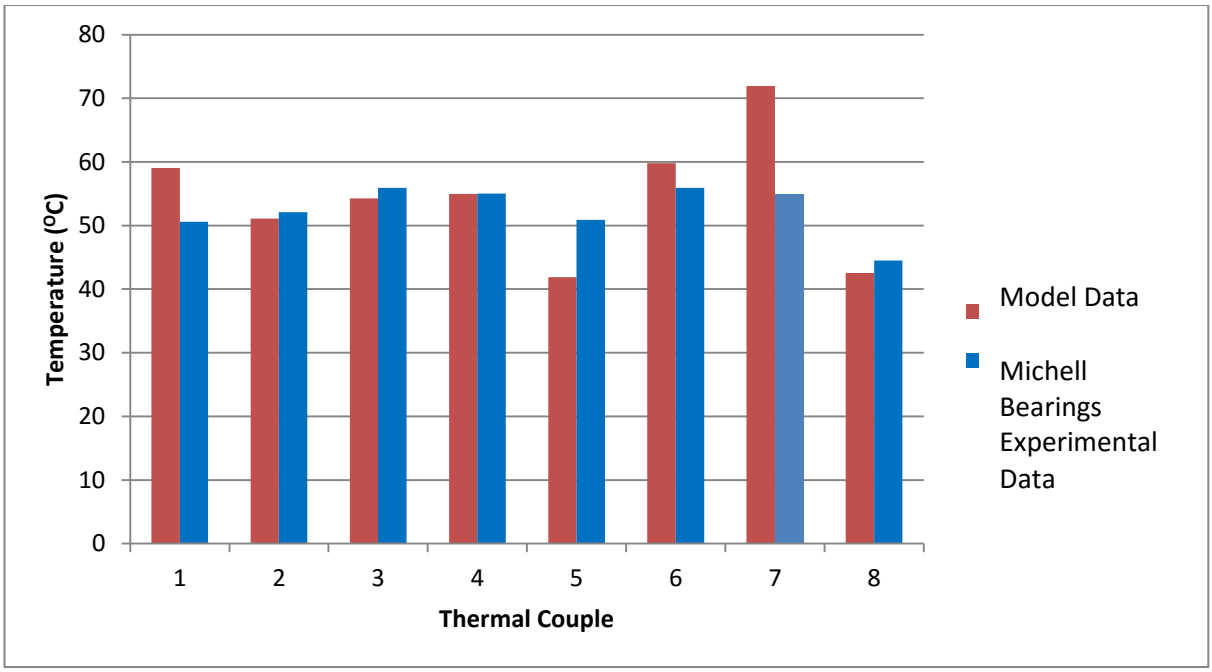

Figure 5.10 Comparison of results at 400RPM rotational speed and 2.88MPa specific Load

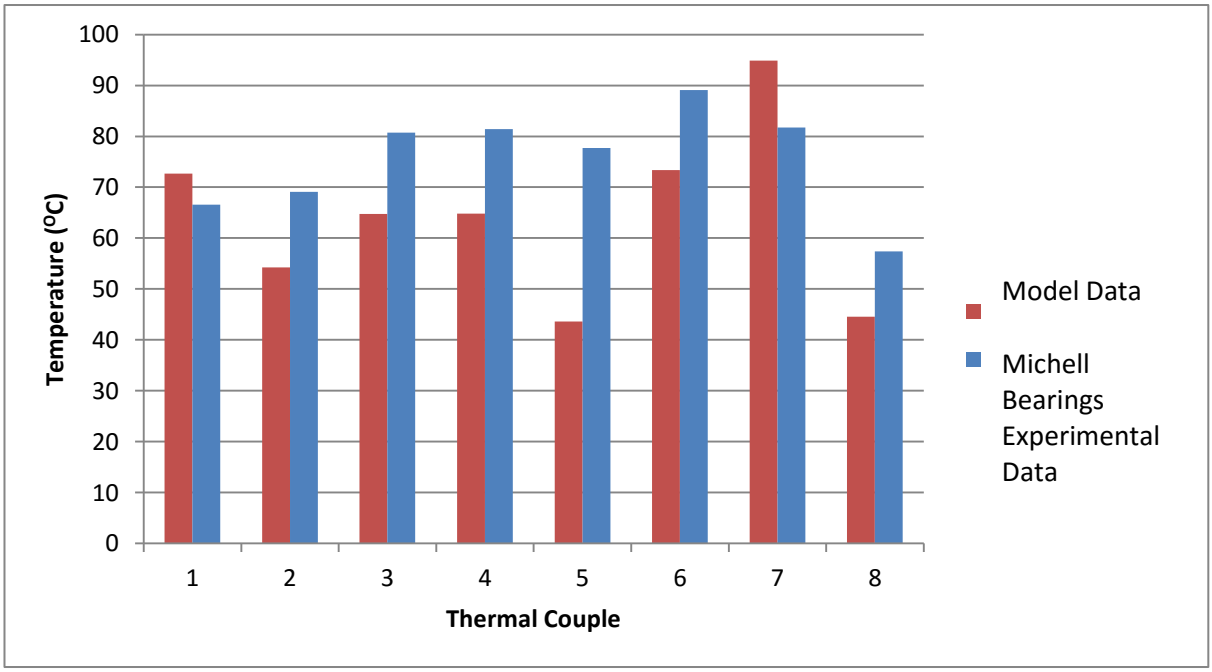

Figure 5.11 Comparison of results 1200RPM rotational speed and 4.33MPa specific Load

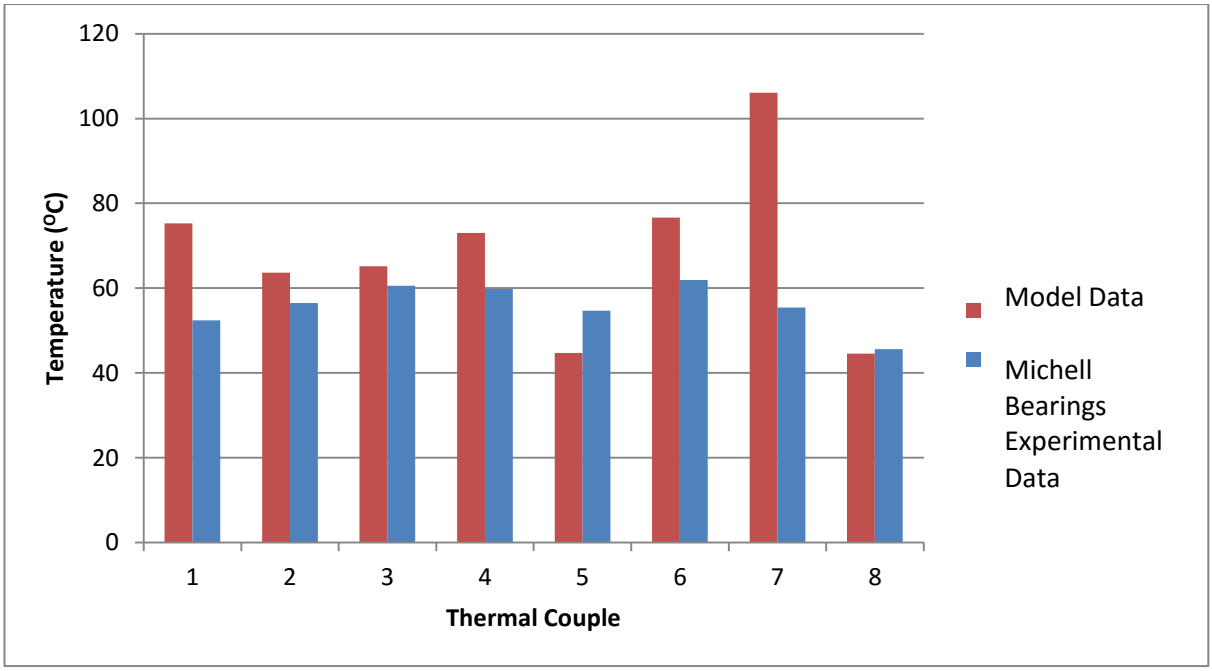

Figure 5.12 comparison of results at 400RPM rotational speed and 5.76MPa specific Load

The results produced by the model vary from the private communications with Michell Bearings test data, with thermocouple 7 being the largest difference in all test cases. The model, generally, predicts a higher temperature then the test data. The model does not include chamfers and fillets (rounded corners) unlike the test experiment. Chamfers have been proven to reduce the overall temperature of a thrust being system [22], mean the temperatures present within the model would be higher than the experimental data. Chamfers also move the peak temperature back towards the centre line of the pad [22]. This would mean that thermocouple 7, which was placed close to the centre of pressure, would no longer be at the location of the peak pressure, and therefore the peak temperature. The author believes that this effect, along with the decrease in overall temperature of the pad due to chamfers, is a cause of the over prediction of temperature by the model.

The thermocouple data location was simulated as accurately as possible, but each thermocouple position may be slightly inaccurate by a few millimetres. From the

temperature profiles simulated by the model, a few millimetres in any direction could have a large effect on the temperature value. This could account for the large difference between the simulated and published experimental results. It would be desirable to compare the model to other simulation results, but the author was unable to find any published data in which enough details on materials and oil properties were given. Whilst not as accurate as comparing the results to the published computational results, the author believes that comparing the data to experimental thermocouple results was a valid method to validate the model as both sets of results were comparable, and every step was taken to make the computational model as representation of the experimental set up as possible.

5.4 Visco-plastic Creep

Using the Norton creep function put forward in Chapter 4- , shown in in equation 5.10, visco-plastic creep effects can be considered within the pads PTFE region, by considering the secondary creep rate$\left(\frac{\partial \varepsilon_s}{\partial t}\right)$.

$$\frac{\partial \varepsilon_s}{\partial t} = 1.60198e^{-17}e^{-\frac{Q}{RT}} \qquad 5.10$$

By solving this equation within the PTFE domain, the predictions of deformation due to secondary creep could be made, allowing for secondary creep effects to be studied throughout the thrust bearings operational life span. This meant that during the course of a simulation, at each pre-set time step, the pad thickness would be altered to account for the creep, which in turn would affect the film thickness, and therefore the pressure seen by the pad. As discussed within Chapter 4, this was only for secondary creep effects, as primary effects were not accounted for.

As stated in section 5.2.1, at the start of the FEM simulation, the PTFE pad was assumed to undeformed, i.e. no primary creep had been taken into account. Options were explored in which primary creep could be included within the model. This included pre-deforming

the pad surface to match a pad which had undergone primary creep. Whilst this would allow the model to account for primary creep, the idea wasn't implemented due to concerns about how much primary creep to account for. The PTFE pad surface would be of different profile depending on how much pressure the pad had been exposed to, the amount of time the pad was at each pressure and at what temperature it had been loaded. This meant that each bearing, for each industrial application, would have a different surface profile.

Another concern was that the experimental equipment used to collect the creep data was designed to collect secondary creep and not primary creep. If primary creep had been the focus of the project, then the sample collection rate during the area of primary creep would have had to be much higher and a higher accuracy of sensor would also be required.

The reasons put forward so far for not pre-deforming the pad surface as a function of primary creep have been due to experimental data concerns. Another reason was due to the computational power of the software used. As discussed within the mesh selection section 5.2.2, the software used had a hard limit of memory before the problem became unsolvable. Adding a deformed surface within the model would require a finer mesh, which would increase the computational memory needed by the software. As the model was running at the upper limit of its solving capability, adding a pre-deformed surface would mean that a solution would not be found.

Including a pre-deformed surface would allow for a fixed amount of primary creep to be included within the model, which in turn would increase the accuracy of the model. Not including it within the model is an obvious limitation of the model but is required to allow for the model to be solved.

5.5 Visco-plastic Creep Study

The visco-plastic TEHL model considered within this thesis was of the same dimension as in the temperature validation study done in section 0. The dimensions of the pad considered can be found in Table 5.5 and the test conditions used within the study can be found in Table 5.6. A diagram of the pad layout can be found in Figure 5.9. The model proposed consists of 3 domains, a fluid domain which was connected to a PTFE domain, which on the lower side of the domain was connected to the PTFE domain, was assumed to be connected to the collar on the top side, though this was assumed to be a boundary, which was assumed to be a set height and did not deform, and no heat transfer occurred. This assumption was also made at the lower boundary of the steel backing material.

Table 5.6 Visco-plastic study test conditions

Specific Pressure (MPa)	Rotational Speed (revs/min)
2.88	400
4.33	600
	800
	1200

Table 5.7 gives the material properties of the pad and oil used within the study. The PTFE considered within this study, as shown in Chapter 3, was a 15% carbon black, 2% graphite filled blend.

Table 5.7 Material properties of the PTFE pad and Oil

	PTFE	ISO-32 Oil
Young's Modulus at 25^{O}C (E) [MPa]	496	NA
Density ($\boldsymbol{\rho}$)[Kg/m-3]	2200	871
Thermal conductivity (K) [W/m/K]	0.22	0.13
Specific heat at constant Pressure (C_P) [J/kg/K]	970	2020
Viscosity at 25^{o}C (μ) [Pa.s]	NA	0.28
Poisson's ratio (v)	0.46	NA
Thermal Expansion Coefficient ($^{O}C^{-1}$)	$124x10^{-6}$	NA

Using these conditions a computational model was undertaken to simulate the visco-plastic creep effects on a PTFE pad, over a 2 year time frame, at 15days intervals. This meant that 48 time steps were considered per test case, and the every combination of test conditions were used. With these results, conclusions could be made about the effect of secondary creep on a PTFE faced thrust bearing pad.

5.6 Summary

Within this chapter a visco-plastic TEHL model has been put forward, which simulates the effects of secondary creep effects on a PTFE faced thrust bearing pad. The equations described by the model are explained along with their origin. An explanation of numerical methods and finite element analysis has been stated, which is used to solve the computational model.

Chapter 6- Results of Visco-plastic Creep effects Simulations

In this chapter, the effect of secondary creep effects is considered for a PTFE faced thrust pad bearing, following the study described within Chapter 5, section 5.5. This applies a TEHL model to predict the temperature and pressure seen by a thrust pad, which is then coupled to a Norton creep function to predict the secondary creep rate and therefore the deformation which the pad will undergo due to the creep. The change in pad thickness is then accounted for within the film thickness equations, which will affect the TEHL results. The effect on pressure, film thickness and temperature seen by the pad are considered as well as change in pad thickness. The model simulated a 2 year operating period for a 15% carbon black, 2% graphite filled PTFE pad, with a constant time step of 15days. The effect of creep on the pad thickness is first considered, before the change in fluid film thickness is discussed. The effect of the deforming pad surface and film thickness on the pressure and temperature profiles of the pad is then considered. Conclusions are then made about the overall system and the interaction between the effects considered as well as the effect on the pad operational life span.

6.1 Thickness of PTFE Pad

Figure 6.1 shows how the thickness of the PTFE faced pad changes over a 2 year time period. From this figure, it can be seen that at the start of the simulation, where no visco-plastic effects accounted for, the pad is thicker at the leading outer edge then the trailing inner edge. At this point in the simulations deformations of the pad is only a function of pressure, into the pad, and thermal expansion. As seen in Figure 6.1, when time = 0 and the initial undeformed pad thickness was 10mm, there is an increase in pad thickness near the leading edge, and the largest decrease in pad thickness at the trailing edge, in the area that largest pressures and temperatures occur. This would suggest that,

whilst thermal expansion does increase the pad thickness, the deformation due to the pressure are generally larger, meaning net the deformation at the centre of pressure, i.e. a reduction of pad thickness.

In all cases considered in the study, the minimum thickness of the pad reduced with time, as shown in Figure 6.1, whilst the maximum thickness of the pad became larger, meaning that the pad is getting thinner in places of high pressure, and thicker in places of low pressure. This is due to the visco-plastic flow of the material from an area of compressive stress to an area of low stress. It can also be seen that as time pass, the contours of the pad thickness become less densely spread, meaning more uniform pad thickness across the pad face, with less normalised 'peaks' on the pad surface.

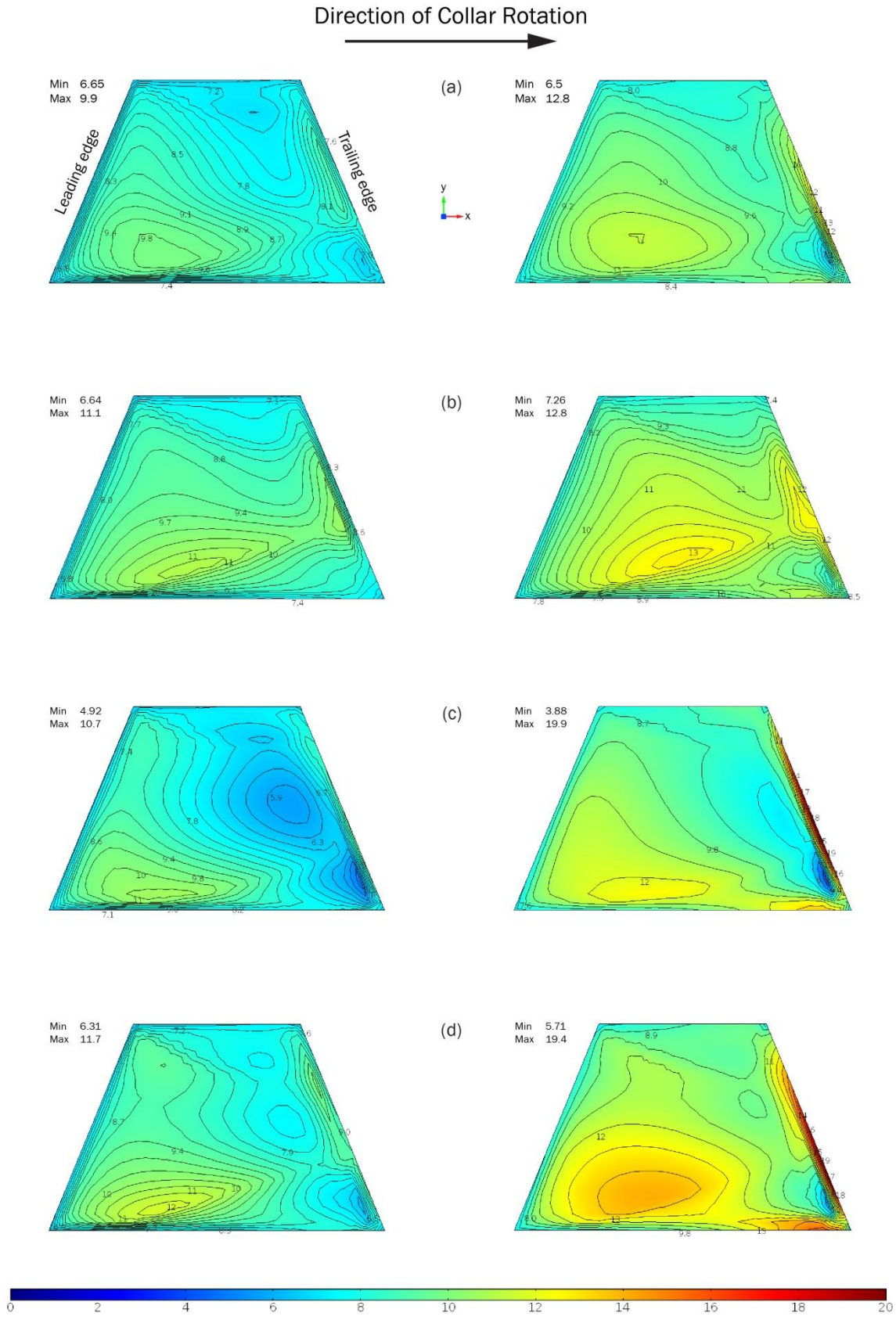

Figure 6.1 PTFE pad thickness (mm)at time= 0 (left hand side) and time= 2 years (right hand side) for a) 400 RPM 2.88 MPa, b) 1200 RPM 2.88 MPa, c) 4.88MPa 400 RPM and d) 4.88 MPa 1200 RPM

6.2 Oil Film Thickness

When the film thickness is considered, it can be observed from Figure 6.2 that in all cases considered within the study, the maximum film thickness decreases gradually over time. When the minimum film thickness is considered, shown in Figure 6.3, it can be seen that for the specific pressure of 2.88 MPa simulations, the film thickness increases very slightly with time. This is not the case for the specific pressure of 4.88 MPa simulations, which after initially increasing the film thickness soon starts to decrease rapidly. This 'turning point' occurs at a different time for each condition, and no clear relationship between time or rotational speed can be found. This 'turning point' is discussed in more detail, when pressure results are considered.

It is interesting to note that whilst quite large changes in the pad surface geometry occur, the overall maximum and minimum values for film thickness no not change dramatically for the 2.88MPa case. This could be due to the maximum film thickness being located at the trailing outer edge, and the minimum film thickness being located at the leading outer edge, as shown in Figure 6.4. This would suggest that tilt angle has a larger effect on film thickness then deformation due to creep, pressure and thermal expasion.

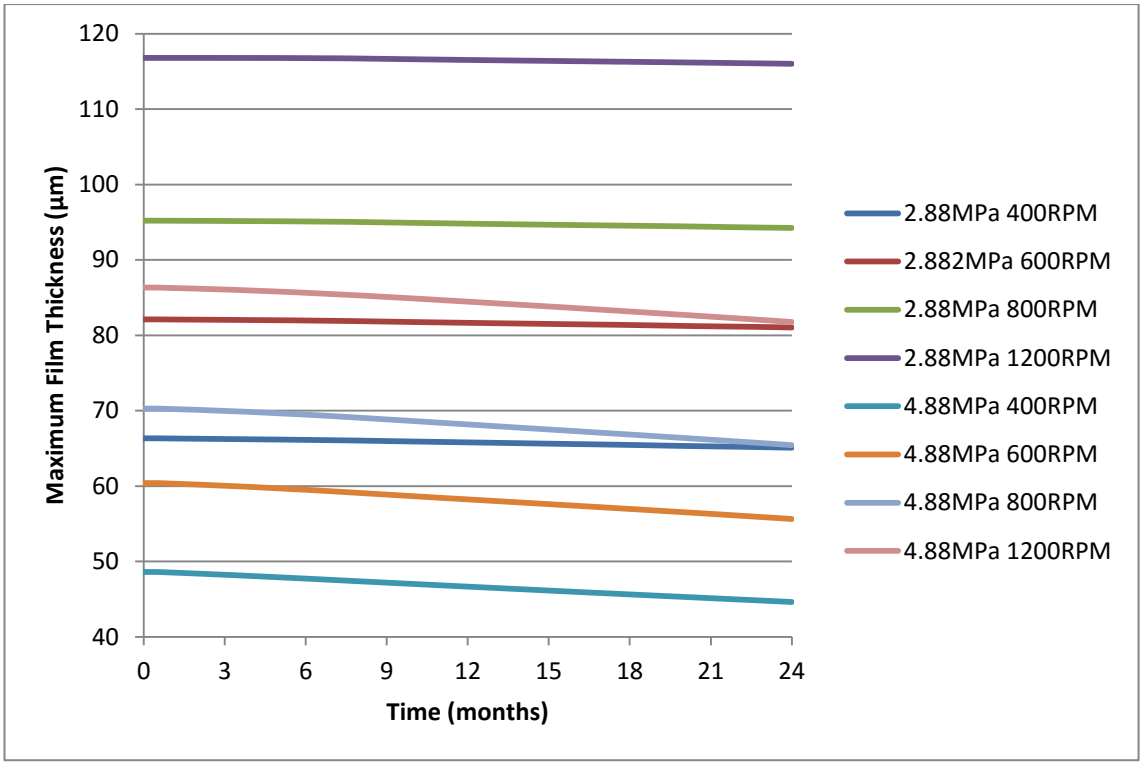

Figure 6.2 Maximum film thickness over a 2 year simulation

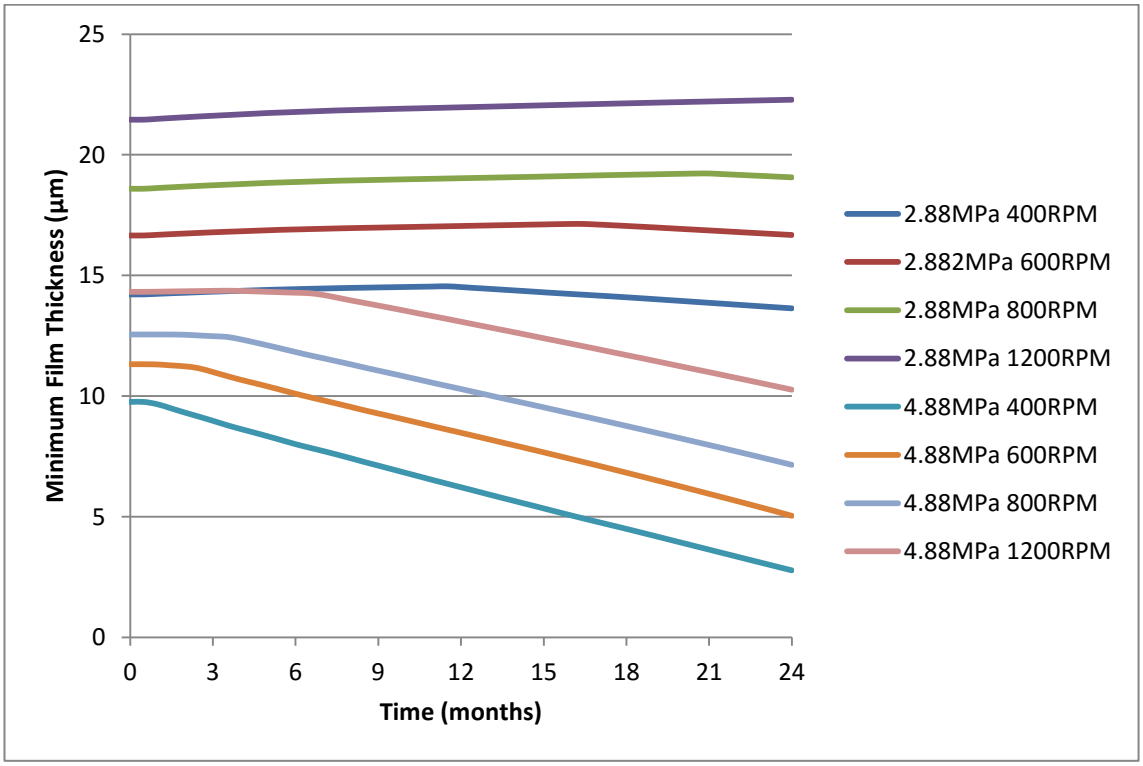

Figure 6.3 Minimum film thickness over a 2 year simulation

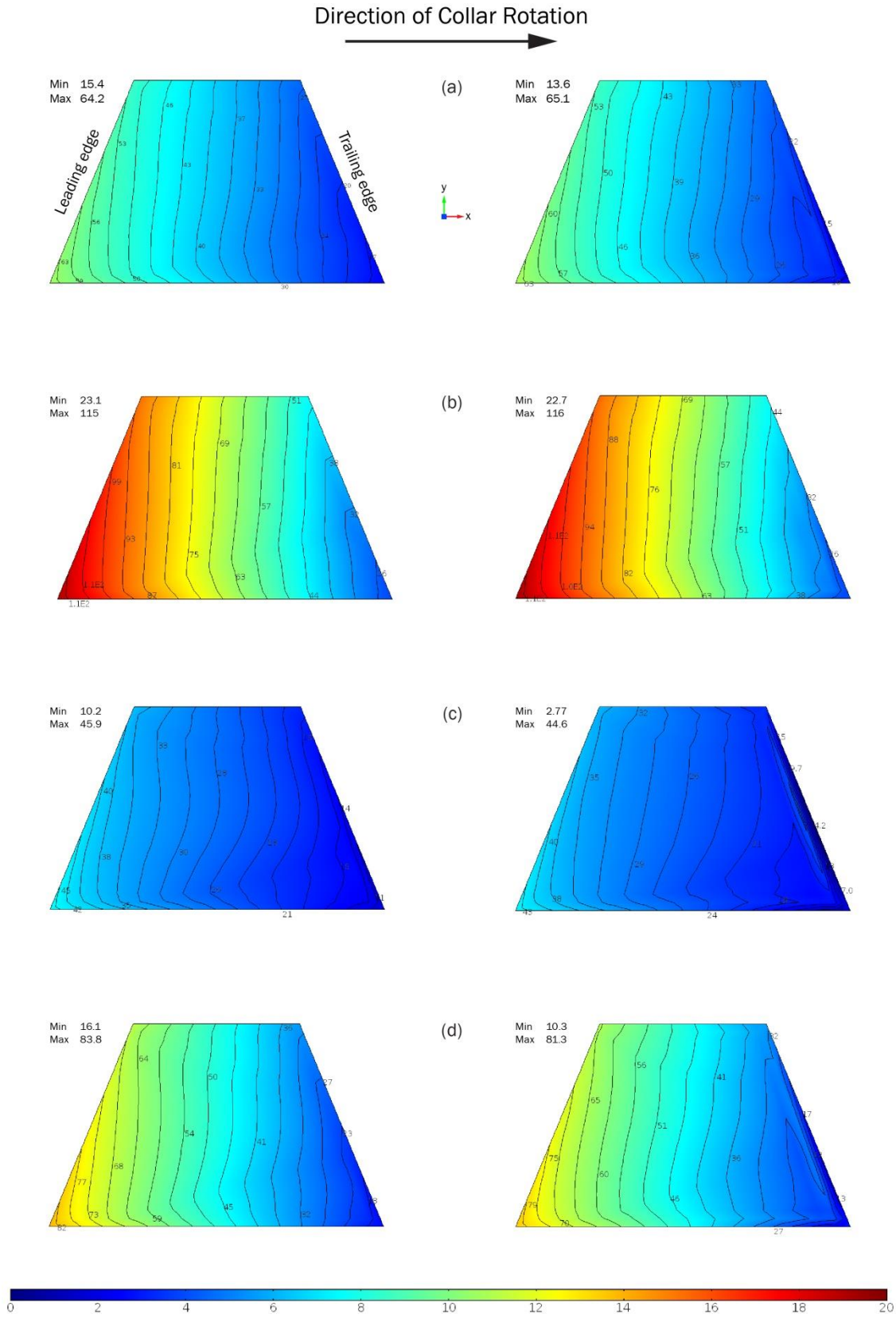

Figure 6.4Film thickness profiles (µm) of PTFE faced pads at time= 0 (left hand side) and time= 2 years (right hand side) for a) 400RPM 2.88MPa, b) 1200RPM 2.88MPa, c) 400RPM 4.88MPa and d)1200RPM 4.88MPa

6.3 Pressure Results

Figure 6.5 shows how peak pressure, seen by the PTFE faced pad surface, changes with time. It can be observed from the graph that for the case of a specific pressure of 2.88 MPa normalised pressure, the peak pressure seen by the pad decreases slightly over time. As the only effect which is a function of time is the creep function, this change in peak pressure is due to the pad deforming due to the creep.

In the case of specific pressure 4.88 MPa normalised pressure, the peak pressure decrease over time for all rotational speeds, until at a certain point in time, the peak pressure starts to increase again. This 'turning point' happens at a later time point as rotational speed increases and the time that this occurs does not increase linearly as rotational speed increases.

The decrease in peak pressure is only about 2% difference for the 2.88 MPa test cases, for all rotational speeds, and around 2-3% for the 4.88 MPa normal pressure, before the 'turning point'. After the turning point, the peak pressure value increases by around 3-4.5% from the original value at time=0. This turning point occurs at a much later point in the simulations then the minimum film thickness 'turning point', though the time delay between these points remains constant. Also both the peak pressure and minimum film thickness all 'turn' at a later time point as rotational speed increase, i.e. the higher the rotational speed, the later the turning point in the simulation. The only mechanical phenomenon being simulated within the model that is a function of time is the secondary creep function. This means that these 'turning points' are caused by the visco-plastic secondary creep effects. By considering the pad thickness results, Figure 6.1, it can be seen that the area of low pad thickness, become very concentrated at the trailing outer edge, and small compared to the remaining area of the pad.

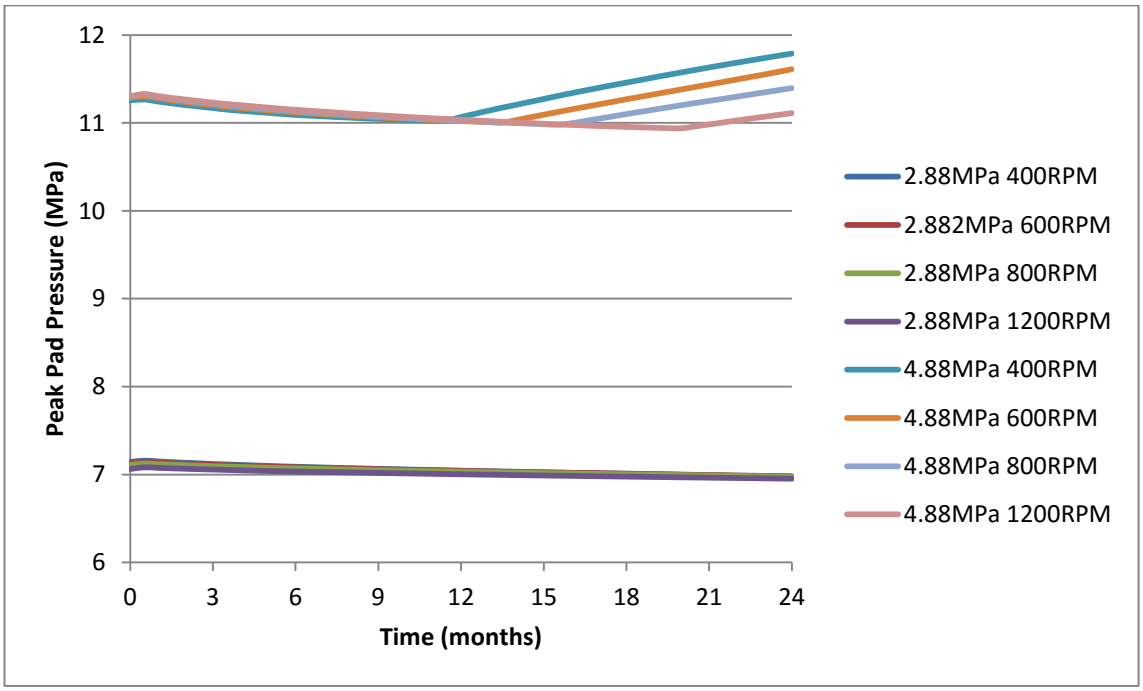

Figure 6.5 Peak pressure seen by PTFE Pad over a 2 year simulation

Figure 6.6 shows the pressure profiles on the PTFE pads surface at the start of the simulation and after 2 years respectively. From there figures, it can be observed that the pressure profile varies very little over the time period. The pressure profile does spread out in the x-direction, most noticeably in case c, 4.88 MPa and 400 RPM, but these changes are very small. There is no obvious change in the y-direction when considering the pressure profile. This change in x-direction, but not y-direction, is expected as the pad is allowed to tilt in the x-direction as a function of centre of pressure, but not in the y-direction meaning that the pressure profile would not change in the y-direction. This lack of change within the pressure profile was an unexpected result, as the pad thickness profiles, shown in Figure 6.1, demonstrate a much larger amount of change. However it could be argued that the pressure distribution is determined by the fluid mechanics and is therefore less affected by changes in pad thickness than might be initially expected.

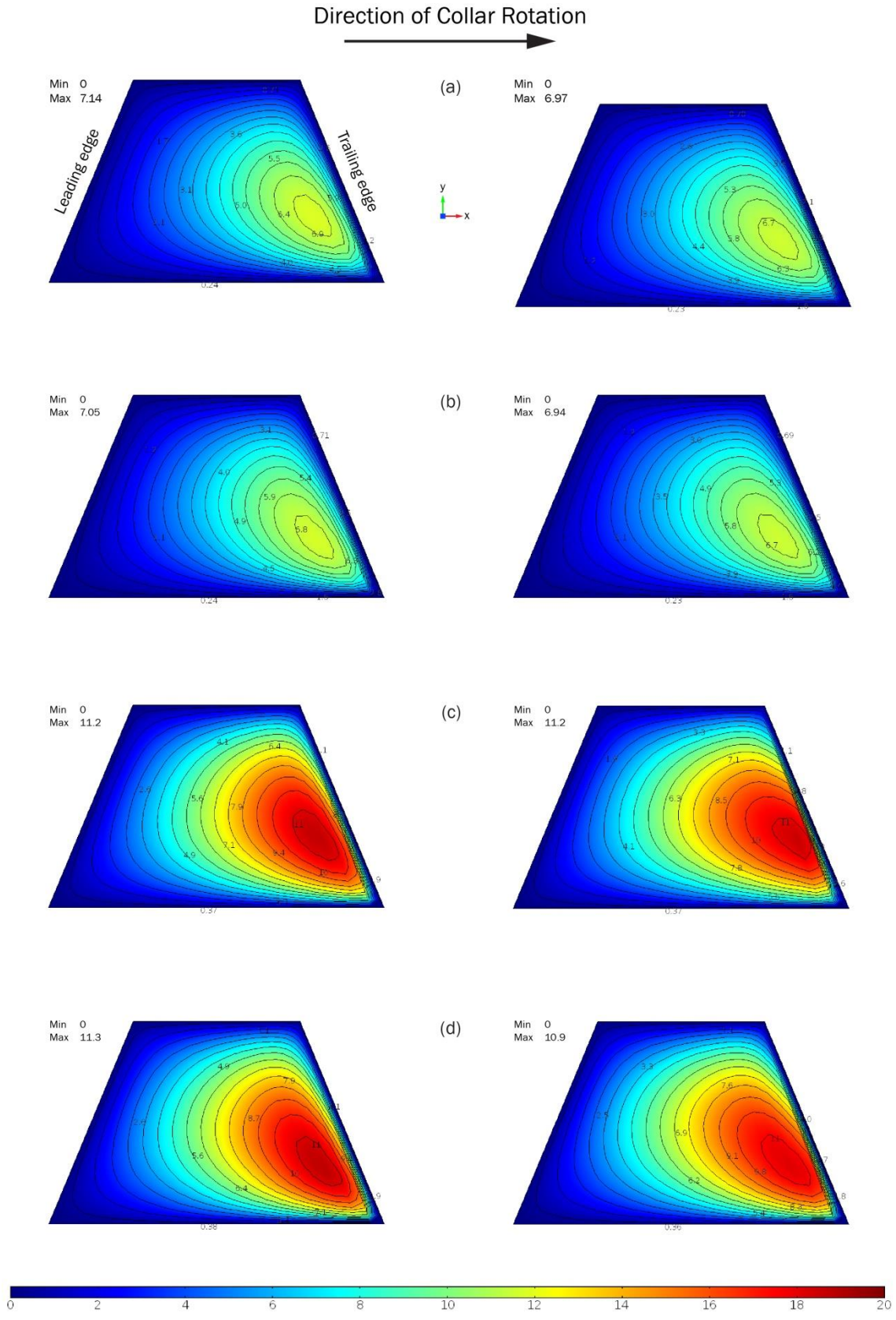

Figure 6.6 Pressure profiles (MPa) of PTFE faced pads at time= 0 (left hand side) and time= 2 years (right hand side) for a) 400 RPM 2.88 MPa, b) 1200 RPM 2.88 MPa, c) 4.8 8MPa 400 RPM and d) 4.88 MPa 1200 RPM

6.4 Temperature Results

Figure 6.7 show how the average temperature of the pad surface changes over the simulation time period. It can be seen that as rotational speed for the specific pressure of 2.88 MPa case increases, the average temperature of the pad decreases over time, whilst the opposite is true for the 4.88 MPa load case, as the speed increases the average temperature also increases with respect to time. The temperature is a shear stress, caused by the change in pressure, a driven parameter, which means that the temperate should follow a similar profile to the pressure as can be seen by comparing Figure 6.6 and Figure 6.8. The areas of large pressures, in Figure 6.6, correlate to areas of high temperature in Figure 6.8, as expected. However the temperature profiles are more spread out than the pressure profiles and this is to be expected due to the hot-oil carry over effect, as described in Chapter 5, i.e. additional heat energy is being added to the system at the leading edge from the previous pad's trailing edge. The temperature at the edges of the pads, shown in Figure 6.8, is governed by the supply oil temperature, which is 40^{O}C.

It can be seen from Figure 6.8, that as time passes the temperature profiles spread out in both x and y directions, towards the leading and inner diameter edges respectively.

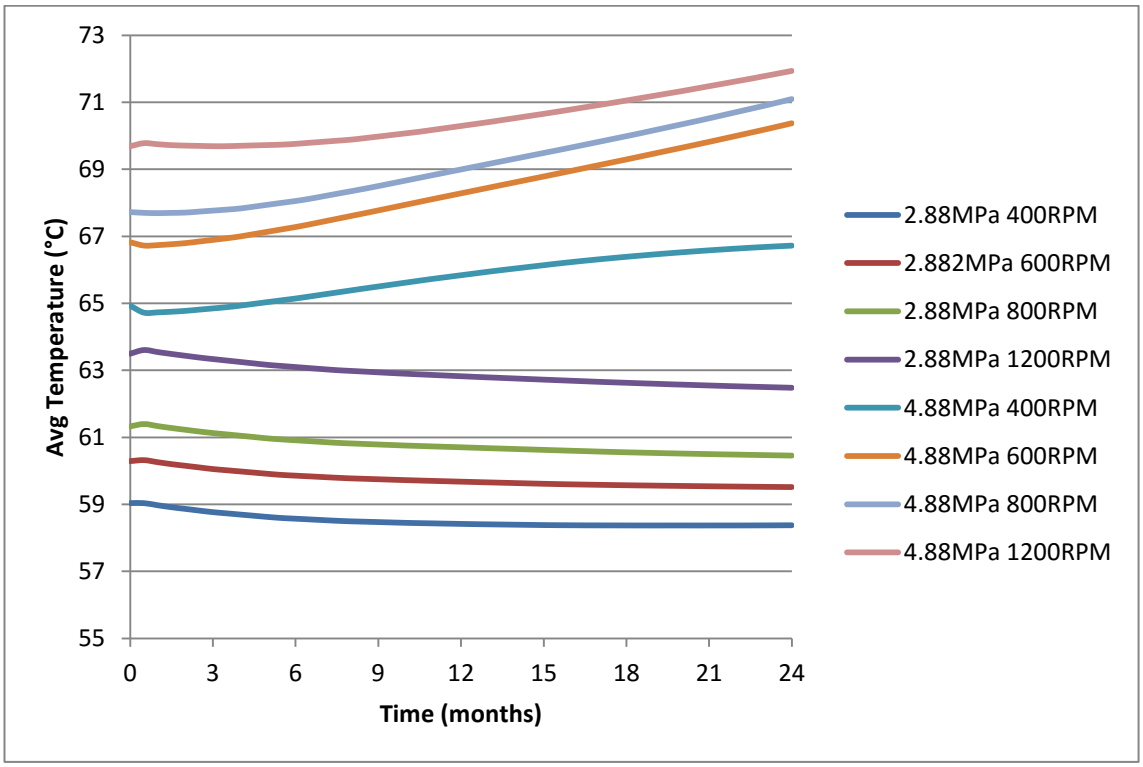

Figure 6.7 Average temperature seen by PTFE pad over a 2 year simulation

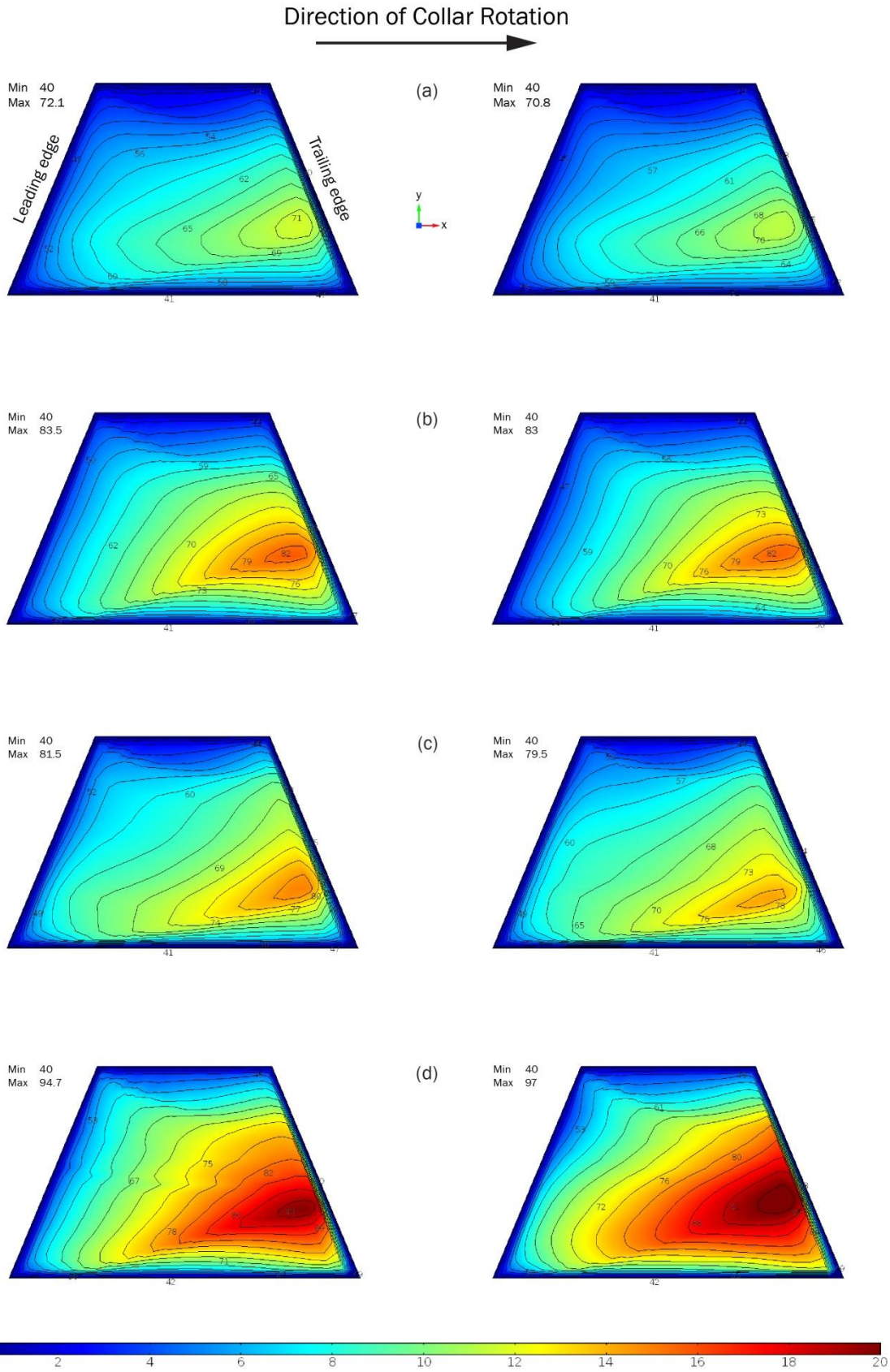

Figure 6.8 Temperature profiles (^{O}C) of PTFE faced pads at time= 0 (left hand side) and time= 2 years (right hand side) for a) 400RPM 2.88MPa, b) 1200RPM 2.88MPa, c) 400RPM 4.88MPa and d)1200RPM 4.88MPa

6.5 Conclusions

The results demonstrate how visco-plastic-creep effects change the surface shape of a thrust bearing pad over the course of its operational life span, which in turn affects the film thickness of the pad, along with the temperature and pressure seen by the pad.

Overall the results found are as predicted: as time passes, the PTFE pad becomes thinner and the film thickness becomes larger, in areas of high pressure and temperature, meaning that the temperature and pressure in these areas decrease. This in turn leads to the thrust bearing pad surface deforming at a lower rate in these areas of high pressure and temperature.

Figure 6.1 shows that the pad increases in thickness along the outer edge of the pad, at the start of the simulations. As time passes, the outer trailing edge part of the pad decreases in thickness, until it is smaller than its original thickness, whilst the outer leading edge of the pad reduces in thickness, but stays above its initial thickness. The deformation of the pad is a function of pressure, thermal expansion and secondary visco-plastic creep effects. If only thermal expansion was accounted for in the pad deformation equations, then a much larger expansion would have been seen at the outer trailing edge. As the pad deformation was in fact a function of thermal expansion, pressure and visco-plastic creep, the latter two variables tending to reduce pad thickness, the net deflection was into the pad surface, meaning that for areas of high pressure, which coincided with areas of high temperature (as temperature was a function of pressure), the visco-plastic and pressure deformation were together larger than the thermal expansion deflection. As the pressure at these locations does not change dramatically, (in fact only 2-4%), it can be concluded that this change in pad thickness is due mainly to secondary visco-plastic creep effects.

Chapter 7- Conclusions and Suggestions for Future Work

Within the body of this thesis a TEHL model has been presented which simulates the effects of secondary visco-plastic creep effects on a filled PTFE faced thrust bearing, providing a detailed understand of the changes a PTFE faced pad will undergo during its lifespan. An EHL method of solving the Reynolds lubrication equations was coupled with the energy equation to allow for heat generation and a Norton creep function to allow for the visco-plastic effects to be modelled. The results of the model were also a function of tilt angle, thermal expansion coefficient, and other thermally dependent material properties. Experimental work was conducted by the author on filled PTFE samples so that the amount of creep strain accumulated within the sample over a 7 day period could be measured. These results were then used to find the parameters a Norton creep function, which was incorporated into the TEHL model. This allowed for conclusions to be made about the effects of secondary creep effects on a PTFE faced thrust pad bearing.

The model has shown that, due to the visco-plastic creep effects, the maximum temperature seen by the pad changes with time depending on the load case, whilst the pad thickness always decreased as time passed. It was observed that the pad thickness became more uniform as time passed due to the visco-plastic effects, though variations of thickness were still present within the pad. This suggests that the visco-plastic effects over time help to counter most of the deformations seen by the pad, caused by thermal expansion of the pad material and the pad deforming due to pressure.

As time passes, the areas of high temperature spread out over the pad profile. This means that the pad is at a more uniformed temperature, meaning that the thermal expansion would tend to be the same across the pad surface. Without the visco-plastic effects, past literature has shown large temperature gradients across a pads surface [7]. This in turn leads to large amount of thermal expansion in some areas and not others. The

work present here suggests that as time pass, the pad deforms equally across a larger area, as the temperature profile is also spread out more evenly over a larger area. This would suggest visco-plastic effects prolonged the lifespan of a PTFE thrust bearing pad.

A reduction in peak pressure, caused by the visco-plastic effects mean that a smaller amount of large pressure deformation is present in the pad, and the pad deforms more uniformly as time passes. This is also supported by the PTFE pad thickness results. A more uniform pressure distribution, as discussed above, would lead to a more uniform pad, leading to a longer life span of a pad. This conclusion is that as the pressure and temperature distribution does not change significantly over time, then most visco-plastic deformation would continue to occur in one location on the pad, which could lead to a very thin PTFE layer and might lead to a failure of the pad. By being allowed to visco-plastic deform, the peak pressure and temperature are allowed to spread over more of the pad, meaning that the pad deformation reduces by less. It is the author's opinion that secondary visco-plastic creep effects help to increase a PTFE faced pad operational lifespan. However it should be pointed out that the current model makes no allowances for damage or failure of the pad material due to long term creep effects.

7.1 Limitations of the model

Due to the complexity of the creep results gained from the experimental work, a function for the secondary creep only was found, and the primary creep was ignored. This was a limitation of the model, as the primary creep did count for a large percentage of the total creep strain. Several different ways were considered to allow for the inclusion of the primary creep; making the Young's modulus a function of primary creep, considering the primary creep as a linear function and fitting a nonlinear curve to the data were all considered. This lack of primary creep within the simulations meant that the model predicted a lower total deformation then the experimental data suggested.

Considering the Young's modulus as a function of primary creep was considered, to allow for the primary creep to be considered as an 'effective Young's modulus'. This idea was ruled out as the creep is permanent deformation, and the method proposed would give an elastic deformation only. This would mean that if the pressure became less within an area, the deformation would spring back elastically towards the originally thickness.

The method of considering the primary creep as a linear function and fitting a nonlinear function to the curve point was ruled out as the point at which each case transitioned into secondary creep, from primary creep, seemed to be random, i.e. a common trend could not be found. This meant that a common point would have to be taken for all the test cases, which would lead to over prediction of creep in most cases. The start point of the secondary creep could be chosen as the secondary creep was a linear function of time.

Another limitation of the model was the inability to run high specific loads and rotational speeds due to instabilities within the model. When a high load or rotational speed was applied to the simulation, the solver would fail to solve due to 'inverse mesh elements'. This meant that the elements, within the fluid domain specifically, were folding back on themselves at the trailing edge. By simplifying the model, it was found that using more elements within the fluid domain, in the z-direction, that the model could solve to a higher pressure and rotational speed. The reason this method was not included within the final model was that as the number of elements increase the program would hit a point of 10GB ram, at which point the software, Comsol 4.3a, would cease to function. It has been reported that this problem has now been fixed within newer versions of Comsol, but the author was unable to remake the model on a newer version of Comsol due to time constraints.

7.2 Future Work

The model presented within this body of work, whilst an improvement on current models used for life span predictions on PTFE thrust bearings, has further room for improvements. The first would be to rebuild the model within a newer version of Comsol so that larger pressure and rotational speeds can be considered. This would also allow for more accurate predictions to be made around the bearing's trailing edge. At the bearing's trailing edge, large deformations are seen. If more elements could be specified in this area, a more gradual and realistic pad deformation should be seen.

To improve the model further and make the model more representative of an industrial thrust bearing pad, chamfers and fillets should be included within the model, which would increase the computational accuracy. From literature it can be seen that this would move the centre of pressure and pressure profiles closer to the centre of the pad.

Another improvement would be the inclusion of primary creep, as this would mean a more realistic visco-plastic deformation would be seen. This could be included with a nonlinear function being found for the primary creep. If the experimental rig was redesigned to allow for a more accurate analysis of the primary creep region, by using a faster sampling rate and with a more accurate sensor, a laser for example, then the primary creep region could be quantified. This was considered during the course of the project, but due to time restraints and cost of the equipment, was decided against.

The inclusion of more temperature dependent variables, Poisson's ratio and density of the pad for example, would also improve the accuracy of the model. This would involve further testing of the filled PTFE samples.

7.3 Summary

The aim of the project was to understand the importance of visco-plastic creep effects within a filled PTFE faced thrust bearing. The work presented here has studied the effect of secondary visco-plastic effects on a PTFE thrust pad, and the long term effects on film characteristics and pressure distributions have been modelled. It has also been observed from experimental work that the primary creep, whilst not included within this study, should be considered within future simulations.

It is considered that the main contributions to knowledge have been the extension of the TEHL thrust bearing analysis to include time dependent deformations of the bearing pad surface coupled with modelling of the creep properties of the filled PTFE for the first time. Although the effects of creep deformations on the bearing performance are not very significant for the range of materials and parameters considered here, the methodology has important implications for the design of thrust bearings where such effects could determine the long term durability of the bearing.

References

1. Ettles, C.M.M., J. Seyler, and M. Bottenschein, *Calculation of a safety margin for hydrogenerator thrust bearings.* Tribology Transactions, 2005. **48**(4): p. 450-456.
2. Ettles, C.M.M., *The Development of a Generalized Computer Analysis For Sector Shaped Tilting Pad Thrust Bearings.* Tribology Transactions, 1976: p. 153-163.
3. Ettles, C.M.M., et al., *Test results for PTFE-faced thrust pads, with direct comparison against babbitt-faced pads and correlation with analysis.* Journal of Tribology-Transactions of the Asme, 2003. **125**(4): p. 814-823.
4. Dowson, D., *History of tribology*. 2. ed. 1998, London: Longman. 768 p.
5. http://michellbearings.com/. *Michell Bearings, Rolls Royce Lmt*. [cited 2014 4th April].
6. http://scioly.org/wiki/index.php/Materials_Science. *Materials Science*. [cited 2015 10/8/2015].
7. Glavatskih, S.B. and M. Fillon, *TEHD analysis of thrust bearings with PTFE-faced pads.* Journal of Tribology-Transactions of the Asme, 2006. **128**(1): p. 49-58.
8. Markin, D., D.M.C. McCarthy, and S.B. Glavatskih, *A FEM approach to simulation of tilting-pad thrust bearing assemblies.* Tribology International, 2003. **36**(11): p. 807-814.
9. Jiang, X., J. Wang, and J. Fang, *Thermal elastohydrodynamic lubrication analysis of tilting pad thrust bearings.* Proceedings of the Institution of Mechanical Engineers Part J-Journal of Engineering Tribology, 2011. **225**(J2): p. 51-57.
10. Dowson, D. and G.R. Higginson, *Elasto-hydrodynamic lubrication*. SI ed. Pergamon international library: international series on materials science and technology. 1977, Oxford: Pergamon. xiv, 235 s. 2 tav.
11. Reynolds, O., *On the Theory of Lubrication and its application to Mr. Beauchamp Tower Experiments.* Phil. Trans, 1886. **117**: p. 157.
12. Pai, S.-I., *Viscous flow theory*. 1956, Princeton, New Jersey,. 2 bd.
13. Dowson, D., *A Generalised Reynolds equation for Fluid-Film Lubrication.* Int J Mech. Sci, 1962. **4**: p. 159-170.
14. Hersey, M.D., *Laws of lubrication of horizontal journal bearings.* Journal of the Washington Academy of Science, 1914. **4**: p. 542-552.
15. Kondo, Y.T., et al., *Tribological properties of ionic liquids, in Ionic liquids - New aspects for the future*. J. Kadokawa. 2013.
16. Sotres, J. and T. Arnebrant, *Experimental Investigations of Biological Lubrication at the Nanoscale: The Case of Synovial Joint and the Oral Cavity.* Lubricants, 2013. **1**: p. 103-131.
17. Cameron, A., *Basic Lubrication Theroy* 1970, London: William Clowes and Sons Limited.
18. Cameron, A. and C.M.M. Ettles, *Basic lubrication theory*. 3rd ed. Ellis Horwood series in engineering science. 1981, Chichester, New York: Halsted Press. 256 p.
19. Tieu, A., *Hydrodynamic THrust Bearings: Theory and Experment.* Journal of Tribology, 1991: p. 633-637.
20. Taniguchi, S. and E.C.M. M, *A thermo-Elastic Analysis of the Paralled Surface Thurst Washer.* Tribolog Transactions, 1975: p. 299-305.
21. Gero, L.R. and C.M.M. Ettles, *A Three Dimensional Thermohydrodynamic Finite Element Scheme for Fluid Film Bearings.* Tribology Transactions, 1988: p. 182-191.
22. Fillon, A. and S.B. Glavatskih, *PTFE-faced centre pivot thrust pad bearings: Factors affecting TEHD performance.* Tribology International, 2008. **41**(12): p. 1219-1225.

23. Ettles, C.M.M. and Cameron. *The Action of the Parallell Surface Bearing*. in *Conference of Lubrication and Wear*. 1968. Int Institution of Mechanical Engineering, London.
24. Wodtke, M., et al., *Large Hydrodynamic Bearings- Comparison of Theoretical and Predicition and Measurements.* Futuroscope, 2010.
25. Glavatskih, S.B., D.M.C. McCarthy, and I. Sherrington, *Hydrodynamic performance of a thrust bearing with micropatterned pads.* Tribology Transactions, 2005. **48**(4): p. 492-498.
26. Sahlin, F., et al., *Two-Dimensional CFD-Analysis of Micro-Patterned Surfaces in Hydrodynamic Lubrication.* Journal of Tribology, 2005. **127**(1): p. 96.
27. http://www.frymetals.com/pdf_uploads/referenceguide.pdf. *Babbit Bearing Alloy Reference Guide, Fry Metals*. [cited 2011 16 August].
28. Rolodo, L., I. Komar, and N. Vulic, *Design and Materials Selection for Environmentally friendly Ship Propulsion Systems.* Journal of Mechanical Engineering, 2013. **59**: p. 25-31.
29. Strecker, W. *Failure Analysis for Plain Bearings*. 2014 [cited 2014 10.1.2016].
30. Simmons, J.E.L., R.T. Knox, and W.O. Moss, *The Development of PTFE (polytetraflorethylene) Faced Hydrodynamic Thrust Bearings for Hydrogenerator Application in the United Kingdom.* Proc. Inst. Mech. Eng Part J, 1998. **212**: p. 345-352.
31. Aleksandrov, A.e., *Use of Elastic Metal- Plastic Segments with Fluoric Plastic Covering on Friction Surfaces in Hydro- Turbine Thrust Bearings.* Gidtrotekhnicheskoe Stroitelstvo, 1981. **9**: p. 12-14.
32. Shen, W., Y, *Development of Teflon- Lined Thrust Bearing Pads on Medium and Large Hydro- Electric Units in China.* Unpublished, photocopies can be provided on request for individual, personal use, 1994.
33. Riande, et al., *Polymer Viscoelasticity*. 2000, New York: Marcel Dekker Inc.
34. Aderikha, V.N. and V.A. Shapovalov, *Effect of Filler Surface Properties on Structure, Mechanical and Triobological Behavior of PTFE-Ccarbon Black Composities.* Wear, 2010: p. 1455-1464.
35. Ching-Wen, L., et al., *Weaving Technology and MEchanical Properties of Extended PTFE Fabrics.* Journal of Tribology, Processing Tech, 2007: p. 319-322.
36. Faughnan, P., et al., *Correclation between Dynamic Mechanical Properties and FAtigue Behavior of Filled and Unfilled PTFE* Journal of Materials Processing Tech, 1998: p. 319-322.
37. Dingham, X. and Y. Kemei, *The Mechanical and Tribological Properties of PTFE filled and PTFE waste Powders.* Journal of Applied Polymer Science, 1996: p. 1035-41.
38. Yujun, X. and C. Xianhu, *Tensile Properties of Glass Fiber Reinforced PTFE using a Rare-Earth Surface Modifier.* Journal of Materials Science, 2001: p. 1729-1731.
39. Benabdallah, H.S. and J. Wei, *Effects if Lubrication on the Friction and Wear Proprieties of PTFE and POM.* Journal of Tribology, 2005: p. 766-775.
40. Burris, D. and W. Gregory Sawyner, *A Low Friction and Ultra Low Wear Rate of PEEK/PTFE Composite.* Wear, 2006: p. 766-775.
41. Shi-Quan, L., L. Tong-Sheng, and L. Ren-Geo, *The Tribological Properties of PTFE Filled with Thermally Treated Nano- Attapilgite.* Tribology International, 2006: p. 541-547.
42. Aderikha VN, S.V., *Effect of Filler Surface Properties on Structure, Mechanical and Triobological Behavior of PTFE-Carbon Black Composites.* Wear, 2010: p. 1455-1464.
43. Ward, I., *Mechanical Properties of Soild Polymers*. 1979, Bristol: J.W. arrowsmith Ltd.

44. Fluoropolymers, *Physical Properties of 'Fluon; Unifilled and 'Fluorocomp' Filled PTFE*. 1993, ICI Group: http://www.agcchem.com/newsroom/finish/13-fluon-ptfe-resins/46-processing-note-f12-13-physical-properties-of-unfilled-filled-ptfe.
45. DuPont, *Teflon PTFE, Fluoropolymer Resin*. DuPont: USA.
46. Maloney, S. *Overview of PTFE fillers used in Rotary Seals, Wear Rings, Piston Rings and Related Sealing Products*.
47. Thermoplastics. *Fluid Power Sealing Materials (PTFE - Filled & Non-Filled)*. Thermoplastics 2014 [cited 2015 Dec].
48. Bingham, E.C., *Fluidity and plasticity*. 1922 New York: McGraw-Hill.
49. Norton, F.H., *Creep of steel at high temperatures*. 1929, New York.: McGraw-Hill Book Co.
50. François, D., A. Pineau, and A. Zaoui, *Mechanical Behaviour of Materials Volume II: Viscoplasticity, Damage, Fracture and Contact Mechanics,* . 1993: Kluwer Academic Publishers.
51. Rappaz, M., M. Bellet, and M. Deville, *Numerical Modeling in Materials Science and Engineering*. 1998: Springer.
52. http://uk.rs-online.com/web/p/thermocouples/0158913. *RS Lmt*. [cited 2015 5 Feb].
53. Johnson, K.L., *Contact Mechanics*. 1985, Cambridge University: Cambridge Press.
54. Gohar, R., *Elastohydrodynamics*. Second Ed ed. 2001, Cambridge: Cambridge University Press.
55. Ettles, C.M.M. and L.R. Gero, *A Three Dimensional Thermo Hydrodynamic Finite Element Scheme for Fluid Film Bearings.* 1988: p. 182-191.
56. McCarthy, D.M.C. and S.B. Glavatskih, *Assessment of polymer composites for hydrodynamic journal-bearing applications.* Lubrication Science, 2009. **21**(8): p. 331-341.
57. McCarthy, D.M.C., S.B. Glavatskih, and I. Sherrington, *Oil-film thickness and temperature measurements in PTFE and babbitt faced tilting-pad thrust bearings.* Proceedings of the Institution of Mechanical Engineers Part J-Journal of Engineering Tribology, 2005. **219**(J3): p. 179-185.
58. Glavatskih, S.B., *Tilting pad thrust bearings.* Tribological Research and Design for Engineering Systems, 2003: p. 379-390.
59. Knox, R.T., *Performance Test on PTFE Faced thrust Pads*. 2004: Newcastle.

Appendix

I. Fluorocarbon PTFE Data Sheets

Fluorocarbon Company Ltd
Caxton Hill, Hertford, Herts
SG13 7NH, UK
Tel: +44 (0)1992 550731
Fax: +44 (0)1992 584697
Email: info@fluorocarbon.co.uk
Web: www.fluorocarbon.co.uk

FLUOROCARBON

Issue 2

DATA SHEET

FLUOROCARBON COMPANY MATERIAL REFERENCE – **FL 515**

DESCRIPTION CARBON AND GRAPHITE FILLED PTFE

TYPICAL APPLICATIONS

Carbon and graphite filled PTFE is normally used in dynamic sealing applications. Carbon filler gives good compression and wear resistance, good thermal conductivity and low permeability. Graphite improves the self-lubricating properties.

TYPICAL PHYSICAL PROPERTIES #

SPECIFIC GRAVITY	(BS EN ISO 13000-2)	2.12
TENSILE STRENGTH	(BS EN ISO 13000-2)	20 MPa
ELONGATION	(BS EN ISO 13000-2)	200 %
SHORE D HARDNESS	(BS EN ISO 13000-2)	60
MAXIMUM WORKING TEMPERATURE		260°C

These figures are typical values for the material and do not represent a product specification. Properties will vary depending on the source of raw material, method of processing, physical form of the product, direction of measurement etc.

II. Engineering Drawings of Creep Rig